Research on Oxygen Evolution Catalysts with High Performances and Low Noble Metal Amounts for Polymer Electrolyte Membrane Water Electrolysis

A Doctoral Dissertation

presented to the Integrated Graduate School of Medicine,

Engineering and Agricultural Science

University of Yamanashi

March 2019

G16DG001 Hideaki Ohno

Contents

Chapter 2: Development of Highly Dispersed Iridium Based Nanocatalysts on Doped Tin Oxides

List of Abbreviations

δ	… The mole fraction of oxygen deficiencies
acac	… Acetylacetonate
AEMWE	… Anion exchange membrane water electrolyzer
AP	… As-prepared
AWE	… Alkaline water electrolyzer
BET	… Brunauer-Emmett-Teller adsorption method
BP	… The British petroleum
CCL	… Current collector layer
CCM	… Catalyst coated membrane
CFE	… Channel flow electrode
CL	… Catalyst layer
COP24	… The 24th climate change conference of the parties
FC	… Fuel cell
fcc	… Face-centered cubic
FIB	… Focused ion beam
FY	… Fiscal year
GDL	… Gas diffusion layer
HER	… Hydrogen evolution reaction
HHV	… Higher heat value
I/S	… Volume ratio of ionomer to supports
ICP-MS	… Inductively coupled plasma mass spectroscopy
ICP-OES	… Inductively coupled plasma optical emission spectroscopy
IEE	… The institute of energy economics
IPCC	… The intergovernmental panel on climate change

IRENA	… The international renewable energy agency
LHV	… Lower heat value
LSCF	… $LaSrCoFeO_3$
LSM	… $LaSrMnO_3$
LSV	… Linear sweep voltammetry
MEA	… Membrane-electrode assembly
METI	… The ministry of economy, trade and industry
OER	… Oxygen evolution reaction
PEFC	… Polymer electrolyte fuel cell
PEMWE	… Proton exchange membrane water electrolyzer
PFSA	… Perfluorosulfonic acid
RHE	… Reversible hydrogen electrode
SEM	… Scanning electron microscopy
SIM	… Scanning ion microscopy
SOEC	… Solid oxide electrolysis cell
SOFC	… Solid oxide fuel cell
S-S	… Start-up and shut-down
TEM	… Transmission electron microscopy
UNFCCC	… The United Nations framework convention on climate change
XPS	… X-ray photoelectron spectroscopy
XRD	… X-ray diffraction method
YSZ	… Y_2O_3 stabilized ZrO_2

Chapter 1: General Introduction

1.1 Background

Because of the drastic improvement of science technologies since the industrial revolution and the explosive increase in the world population (over 7.5 billion in 2018), the energy consumption have been increasing continuously in decades. We've been relying on the primary energy resources largely, particularly the fossil energy that are used as coal, oil, and natural gas principally [1]. However, the concentration of greenhouse gases such as CO_2, CH_4, and NO_x in atmosphere in the world has been increased due to the large consumption of fossil fuels, leading to serious environmental issues such as global warming and the pollution of air, soil, and ocean [2]. As an approach of the international framework to reduce greenhouse gas emissions, adaptation, and finance, Paris Agreement was adopted within UNFCCC in 2015 [3]. This long-term goal is to maintain the increase in the average temperature to below 2°C compared to pre-industrial levels, and to limit the increase to 1.5°C. 184 nations participating in UNFCCC have become parties to this agreement as of November 2018.

In Japan, the total greenhouse gas emission was the 5th largest among the world [4], and we have set the goal as the decrease in 26% until FY2030 compared to those of FY2013. At present, the primary energy supply in Japan has been produced dominantly by fossil fuels: as high as 89% since the fatal accident of the Fukushima Daiichi Nuclear Power Plant by the Great East Japan Earthquake in 2011. Considerable amount of fossil fuels such as natural gas, oil, and coal, etc. have been imported for the power generation [5]. The domestically supplying energies converts partially into materials derived from fossil fuels such as kerosene, gasoline, petroleum products, whereas they are also utilized as electric power, which amount accounts for a percentage of 43% within the energy supply [6]. The electricity is the secondary energy, which is the most convenient for general use, while a large decrease of CO_2 emission is quite difficult by conventional thermal power plants. If we get thermal-power-derived electricity from the combustion of fuels, the efficiency is low because it is limited by Carnot efficiency, e.g., the efficiency of conventional thermal power plants that consume a large amount of natural gas or coal is about 40%, and the remaining 60% of heat is wasted on the earth. Unlike thermal power plants that are subjected to thermal engine restrictions, fuel cells (FCs) can convert the chemical energy from hydrogen into the electric power with high conversion efficiency [7]. The theoretical efficiency of FCs by the use of pure hydrogen is 83% based on higher heat value (HHV), when and liquid water is produced. Since it is ca. twice that of a conventional power plant, the fuel required would reduce to half and the CO_2 emission would be halved. Of course, the power generation efficiency in actual FCs decreases due to the overvoltage loss. However, by utilizing the waste heat as a form of hot water in co-generation systems, the overall efficiency is as high as 93% based on lower heat value (LHV) for residential FCs.

In order to establish the low-carbon and ultimately CO_2-free society combined with FCs independently from the thermal power generation, the use of renewable energy sources is favored, such as hydro-, geothermal-, wind-, and solar-powers. The renewable capacities have been increasing in worldwide year by year [8]. In Japan, the amount of the hydroelectric generating capacity was almost constant because large-scale generation involving the pumped-storage method has been already well-developed, whereas those from wind and solar powers are significantly increasing [9]. However, the power output from such renewable resources is intermittent in nature, i.e., wind power systems with rotation of turbines depend largely on the wind velocity, and photovoltaic cells cannot generate electricity in night. In addition, the locations suitable for renewable power generation are not always close to those with power demands. To match the energy supply with the demand, an efficient energy storage system is necessary to achieve the effective utilization of large-scale renewable electricity.

Hydrogen is received attention as an attractive energy carrier with high energy density, which is one of fuels for FCs. Hydrogen can be obtained by various methods, industrialized production methods of the reformation of hydrocarbons: Such as naphtha, city gas, and methanol, the thermochemical water splitting reaction via the iodine-sulfur process with high temperature ~ 1000°C, as well as involving by-product from brine electrolysis, are commonly used for mass production of hydrogen [10–12]. The water electrolysis, where electricity is used to split water into oxygen and hydrogen, will also play an important role, because it has the excellent advantages as follows [11,13]:

1) High purity H_2 (≥ 99.99%) can be generated by one-step reaction directly converted from water and electricity.

2) On-site production of H_2 is possible; it is convenient for industries such as semiconductor fabrication, ammonia production, oil refinery, etc.

As shown in **Figure 1-1**, the concept of hydrogen energy society is one of the key strategies in our country to solve the energy and environmental issues. The Ministry of Economy, Trade, and Industries (METI) of Japan announced a "Hydrogen-Fuel Cell Strategic Roadmap" in 2014 to realize the hydrogen society by industrial-academic-government cooperation as follows [14]:

Phase 1) Development of domestic power-to-gas systems for renewable hydrogen supply

Phase 2) Development of international hydrogen supply chains with utilizing unused energy and renewable energy from overseas

Phase 3) Establishment of CO_2-free hydrogen supply systems (brown coal combined with carbon dioxide capture and storage methods utilizing renewable energy)

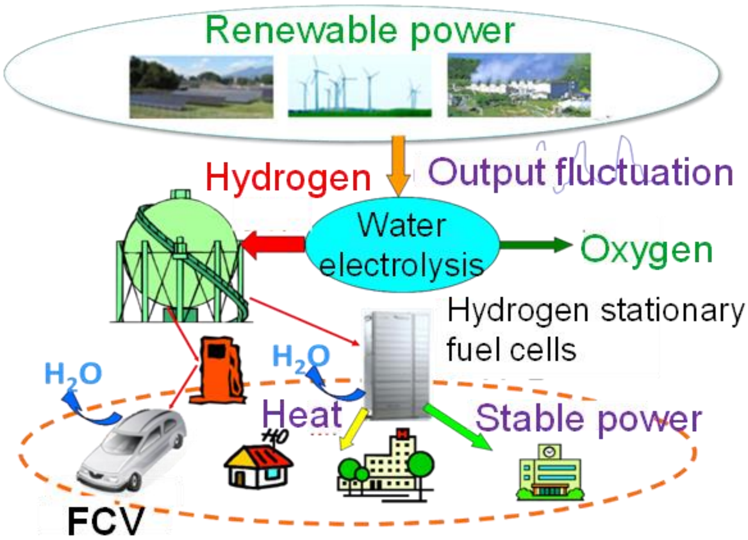

Figure 1-1. A schematic image of hydrogen energy society constructed by the combination with fuel cells (FCs) and electrolysis.

1.2 Water electrolysis

1.2.1 Thermodynamics

Water electrolysis reaction is written by:

$$H_2O \rightarrow H_2 + \frac{1}{2}O_2 \qquad (1.1)$$

According to the thermodynamics, the total energy required for the electrolysis, reaction enthalpy (ΔH), is the sum of the Gibbs free energy (electrochemical work; ΔG) and the heat energy ($\Delta Q = T\Delta S$), where ΔS is the change in entropy of the reaction as following equations:

$$\Delta H = \Delta G + T\Delta S \qquad (1.2)$$

For the electrolysis of liquid water at 298 K under the standard conditions (activities of H_2O, H_2, and O_2 are unity: pure H_2O and 101.3 kPa of gases), $\Delta H° = 286$ kJ mol^{-1}, $\Delta G°=$ 237 kJ mol^{-1}, and $\Delta S° = 163$ J mol^{-1} K^{-1}. $\Delta G°$ represents the minimum amount of electrical energy required for the water electrolysis reaction. The reversible standard voltage for the electrolysis ($U_{rev}°$) is calculated by the following equation;

$$U_{\mathrm{rev}}° = \frac{\Delta G°}{2F} = 1.23 \text{ V (at 298 K)} \qquad (1.3)$$

where F is the Faraday constant. The entropic heat energy $T\Delta S°$ is usually supplied either internally (Joule heat in the electrolyzer) or externally (from a heat source). In contrast, the thermoneutral standard voltage for electrolysis ($U_{th}°$) is calculated as follows:

$$U_{\mathrm{th}}° = \frac{\Delta H°}{2F} = 1.48 \text{ V} \qquad (1.4)$$

The standard values of ΔH and ΔS at any temperature (ΔH_T and ΔS_T, respectively) can be calculated by the use of the heat capacity at constant pressure (C_p):

$$\Delta H_T° = \Delta H_{298}° + \int_{298}^{T} C_p \, dT \qquad (1.5)$$

$$\Delta S_T° = \Delta S_{298}° + \int_{298}^{T} \frac{C_p}{T} \, dT \qquad (1.6)$$

For the case of water vapor, the value of $\Delta H°$ is reduced by the latent heat of vaporization of water (ΔH_{vap}, 44 kJ mol^{-1} at 298K). Thus, the value of $\Delta H°[H_2O(l)]$ = 286 kJ mol^{-1} at 298 K is referred to HHV, while $\Delta H°[H_2O(g)]$ = 242 kJ mol^{-1} is called as LHV.

The temperature dependences for U_{th} and U_{rev} are shown in **Figure 1-2**. The change in U_{th} with temperature is relatively small, while U_{rev} is reduced with temperature due to the increase in the term of $T\Delta S°$ (> 0). Therefore, a high temperature steam electrolysis (so-called, solid oxide electrolysis cell; SOEC) is favorable with respect to the reduced electric energy required (U_{rev}) with an assist of heat energy. An effect of the pressure in the electrolyzer on the U_{rev} can be calculated by the substituting the Nernst equation;

$$U_{\mathrm{rev}} = U_{\mathrm{rev}}° + \frac{2.303RT}{2F}\log\frac{P_{H2}\sqrt{P_{O2}}}{a_{H2O}} \quad (1.7)$$

where R is the universal gas constant.

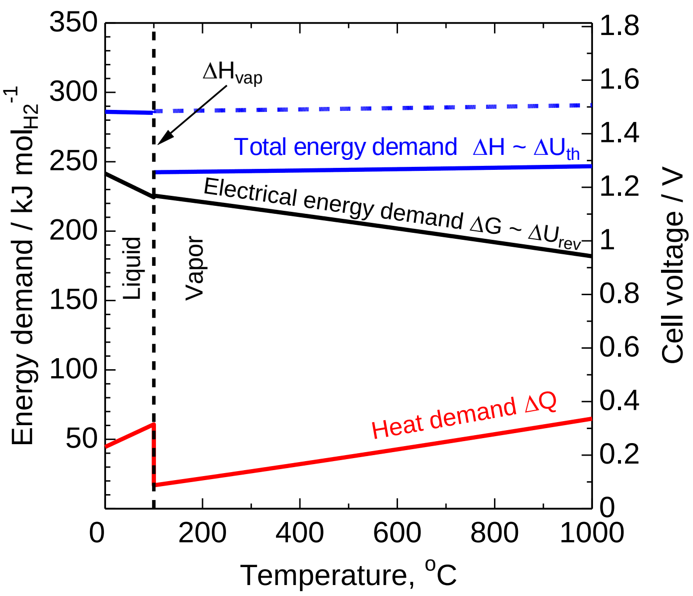

Figure 1-2. The values of total (Δ*H*), thermal (Δ*Q*), and electrical (Δ*G*) energies, as well as cell voltages (U_{th} and U_{rev}) calculated from Δ*H* and Δ*G*, respectively, for an ideal electrolysis process as function of the temperature at a constant pressure.

In the actual cells, the cell potential (E_{cell}) is larger than the thermodynamic value U_{rev} due to several overpotentials (or polarizations): E_{cell} is the sum of U_{rev} and the overpotentials caused by ohmic resistance (η_{ohm}), activation overpotential (η_{act}) and mass transport (concentration overpotential, η_{conc}):

$$E_{cell} = U_{rev} + \eta_{ohm} + \eta_{act} + \eta_{conc} \quad (1.8)$$

The voltage efficiency (ε_v) in a practical electrolyzer is calculated as follows:

$$\varepsilon_v = \frac{U_{th}}{E_{cell}} \qquad (1.9)$$

The current efficiency (ε_F; Faradaic efficiency) is defined as the ratio of generated amount of gas (H_2) to the theoretical one calculated based on the Faraday's law. Finally the energy conversion efficiency of the electrolyzer ($\varepsilon_{electro}$) is the product of ε_v and ε_F, which is the ratio of the theoretical energy $\Delta H°$ to the energy consumed actually:

$$\varepsilon_{\mathrm{electro}} = \varepsilon_{\mathrm{v}} \times \varepsilon_{F} \qquad (1.10)$$

1.2.2 *Kinetics*

In this section, properties of three major water electrolyzers are described briefly. Operation principles of alkaline water electrolyzer (AWE), proton-exchange membrane water electrolyzer (PEMWE), and solid oxide electrolysis cell (SOEC) are illustrated in **Figure 1-3**. Their main characteristics are summarized in **Table 1-1**.

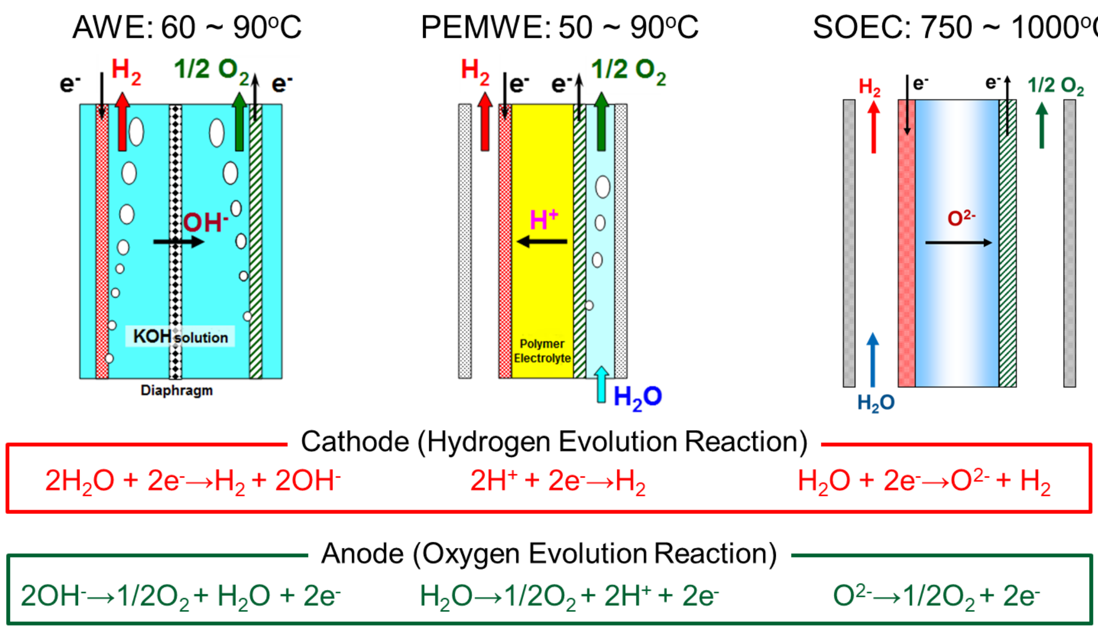

Figure 1-3. Schematic images, typical operation temperature, and reaction formula for three representative electrolyzers.

Table 1-1. Main characteristics of three representative electrolyzers.

Cell type	Alkaline [15,16]	PEMWE [17,18]	SOEC [19,20]
Efficiency of the electrolyzer, $\varepsilon_{electro}$	~ 80%	~ 80%	~ 100%
Current density (A cm^{-2})	~ 0.4	~ 3.0	~ 1.0
Cathode	Ni, Fe, Ni-coated steel	Pt black, Pt/C	Ni-YSZ
Anode	expanded Ni-plated steel, Ni-coated steel, Ni-Co oxides, perovskite-type oxides	Ir, IrO_2, Pt/Ir, RuO_2, $(Ir,Ru)O_2$, $(Ir,Sn)O_2$	LSM, LSM-YSZ, LSCF
Electrolyte	20~40wt% KOH solution	Perfluorosulfonic acid (PFSA) membrane	YSZ

1.2.2.1 Alkaline Water Electrolyzer (AWE)

Since the electrolysis phenomenon was discovered in 1789 [18], AWEs have been commercialized and operated as a well matured technology for hydrogen production up to the MW in the world. The AWE by the use of 20 to 40 wt% KOH electrolyte solution is the most-established technology among various water electrolyzers [15,21]. Advantages of AWEs are cost effectiveness due to the use of non-precious metal (or metal oxide) catalysts and low temperature operation (usually < 100°C). In contrast, because H_2 and O_2 gas evolution takes place from the cathode and anode into KOH solution to disturb the ionic conduction, the current density should be moderate and an appropriate diaphragm is necessary to separate gases from two electrodes (**Figure 1-3**). However, it is difficult for the diaphragm to suppress the cross-diffusing of gases completely, leading to a mixing of oxygen and hydrogen, which reduces apparent Faradaic efficiency [15]. Recently, an anion exchange membrane water electrolyzer (AEMWE) has been investigated. Even at a laboratory scale, an AEMWE has been operated to mitigate disadvantages of AWE described above [16]. The major problems for AEMWE have been reported to be low activities of electrocatalysts [16,22-24].

1.2.2.2 Proton-Exchange Membrane Water Electrolyzer (PEMWE)

To overcome the drawbacks of AWE, a solid polymer membrane with very thin (100-200 μm) as an efficient separator have been investigated in the field of brine electrolysis in 1950's [25]. In addition, another approach was designed to press electrodes on each side of the membrane to reduce ohmic potential loss in the electrolyte (similar to the catalyst coated membrane; see section **1.3**). This design has also been applied in systems using the reverse reaction to PEFCs and high-temperature water electrolysis technology, in which deionized water in the form of liquid or steam can be used as a reactant. The first PEMWE was invented based on the use of a solid polymer (perfluorosulfonic acid; PFSA) as an electrolyte and a gas separator in the 1960's [17,18,21]. Such membrane properties also open up the possibility to carry out the electrolysis at elevated pressure or even in a type of electrochemical compressor with a minimized risk of explosive gas mixtures forming [18,25]. It leads that the produced hydrogen in pressurized vessels can be stored practicably, and the external mechanical hydrogen compressor can be down-sized or eliminated [26], while it has the possibility of the formation of an explosive mixture at high pressure due to cross-over of producing hydrogen in an extreme case [25]. Thicker membranes are required to minimize this negative aspect, leading to increased ohmic losses of the cell. An operating pressure of up to 150 bars has been achieved on a commercial basis [18,25].

In the early era for non-pressurized PEMWE systems, the presenting performances was low with a high potential of 1.88 V at 1 A cm^{-2} and 80°C [18]. However, it has been improved to 1.75 V at a similar condition in 2000's, furthermore more recently it was reported that the operation of 3 A cm^{-2} at ~1.8 V in the institute [18,21,25,27]. In terms of the durability, a high current density of 1 A cm^{-2} at 80°C and 15,000 hours (up to 1.75 V) operation was achieved in industrial PEMWE in 1990's [25], and recently, the commercialized PEMWE was developed by several groups up to the operation at ~2 A cm^{-2} (~ 2 V) and 20,000-60,000 hours [18,21]. This advantage of PEMWE is superlative among the water electrolysers at present.

Nevertheless, a big drawback of conventional PEMWEs are concerned, that is very expensive because the selection of electrodes and the current collector layer (CCL) has been limited because of the strongly acidic environment and high potential operation at the anode. For instance, the use as electrode reaction catalysts is confined to noble metal based electrocatalysts for the state-of-the-art in this field. This is related to the motivation of this work (see section **1.3**).

1.2.2.3 Solid Oxide Electrolysis Cell (SOEC)

In the 1980s, the first to report was resulted from a SOEC using a supported tubular electrolyte [18]. The operation temperature of SOECs was mostly 900 to 1000°C, but it has been lowered to ca. 800 or 700°C recently for the reduction of both degradation rates of component materials and fabrication costs as well as utilization of various waste heat sources [19–21]. Due to the high temperature operation compared with AWE and PEMWE, SOECs are expected to provide the highest efficiency of electrolytic hydrogen production, because the E_{cell} can be reduced due to favorable thermodynamic and kinetic conditions, therefore non-noble metals can be used for catalysts in SOECs. In addition, when SOECs are operated reversely, they can work as solid oxide fuel cells SOFCs to generate electricity with a high efficiency by consuming stored hydrogen or fossil fuels. However, due to high temperature operation, the start-up and shut-down (S-S) cycles of SOECs take long time, and frequent S-S cycles are avoided to suppress the degradation due to thermal cycles [19–21].

1.3 Component Materials and Issues of PEMWE

In this work, PEMWE have been selected because it has the following advantages; ease of maintenance and the compact system design compared to AWE, with moderate electrolysis efficiency ($\varepsilon_{electro}$, ~ 80%) even at high current density operation (~ 3 A cm^{-2}) by the use of a PFSA or a hydrocarbon based membrane compared to the other electrolysers as described in section **1.2.2.2**. **Figure 1-4** shows the schematic diagram of a practical PEMWE cell. The center part which the electrocatalysts sprayed on the both sides of a membrane (so-called catalyst coated membrane; CCM) is sandwiched by CCLs. A CCL plays roles in current collector, as well as diffuse liquid or gases (H_2 at the cathode, H_2O and O_2 at the anode), thus it is also named the gas diffusion layer (GDL). Such a structure of the single cell is called as a membrane-electrode assembly (MEA). A MEA is usually further sandwiched by separators with flow channels. Gaskets are used to avoid to leak of gases.

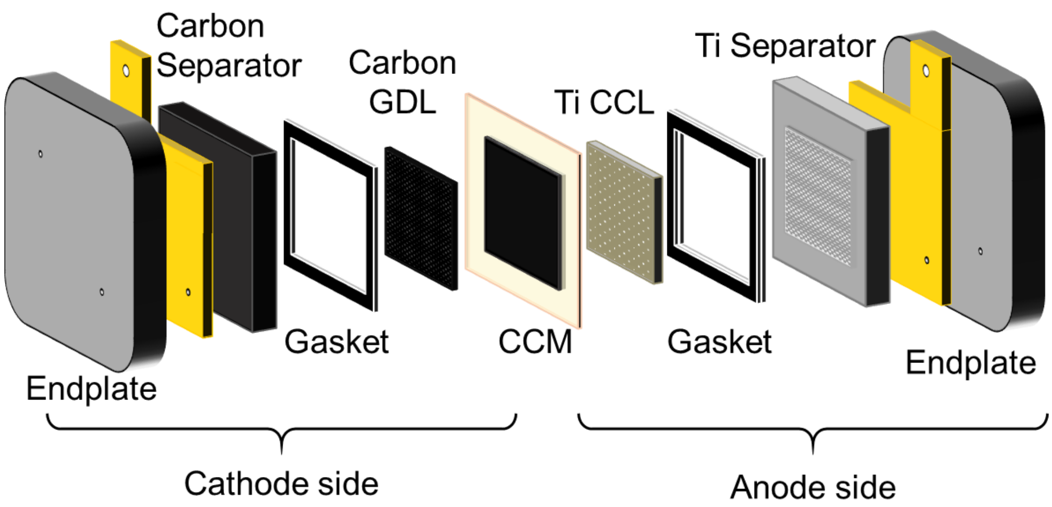

Figure 1-4. Schematic images of components in a practical PEMWE cell (a single cell).

As stated in section **1.2.2.2**, the main drawback of PEMWE is its cost. It was reported that the average capital cost of a hydrogen station of PEMWE is predicted >200,000 yen kW^{-1} [21,26,27]. The cost of stacks accounts for a percentage >50% in one system, in addition the breakdown of stacks as follows; separators (~50%), MEAs (~30%), and the balance and/or manufacturing (~20%) [26,27]. For separators at the anode, titanium plates coated with precious metals (platinum or gold) have been used. This reduces the corrosion rate but costs because of the coating step and titanium base itself. At the cathode, carbon based materials have been used frequently as same as the polymer electrolyte fuel cell (PEFC) field, however, it is also expensive. A paper was published that was related to industrial designs in terms of the separators in stacks for the cost reductions [27]. For MEAs, it has been addressed that concerns regard with the high costs of electrocatalysts were based on Ir and Pt black with high metal loading (≥ 2 mg_{Ir+Pt} cm^{-2} in each electrode) as far [18]. Moreover, if hydrogen is used as the major energy carrier supplied by PEMWE for the large-scale (GW~TW level) combined with renewable energies, it is expected to be required of 25% utilization of Ir production rate in the world (use of 2 mg_{Ir} cm^{-2} at 4 W cm^{-2} operation) [27]. Therefore, almost all interest to the electrocatalyst tends to the reduction of the noble metal amounts. To solve the catalyst problem, one possible approach is to use nano-sized catalysts highly dispersed on support materials in place of noble metal blacks with large particle sizes.

Catalyst developments for PEMWE using liquid acid electrolytes were already reported for both cathode (hydrogen evolution reaction; HER) and anode (oxygen evolution reaction; OER) in bulk states. It was clarified that when single elements were used alone, the both reactions were essentially dependent on noble elements for the sake of efficiency. For the HER, it was found that the order of catalytic activities in 0.1 M H_2SO_4 was Pt ~ Pd > Rh > Ir > Ru > Ni [28]. For the OER, the order for metals was Ru

> Ir > Pd > Rh > Pt (for oxides: RuO_2 > IrO_2 > PtO_2 > Co_3O_4) [28–30]. In the recent years, Pt-alloy electrocatalysts on the cathode have been worked [31,32], while the large efforts have been focused on the anode, because the overpotential at an anode is commonly much larger than that at a cathode. The large overpotential will lead to lower the efficiency in PEMWE, which is associated with the sluggish kinetics and complicated reaction mechanisms in OER processes [33,34]. Indeed the Ru-based catalyst, especially RuO_2 was discovered to exhibit much lower oxygen overpotentials than any other materials tested, however, a major drawback with RuO_2 is that it corrodes at high potential in oxygen evolution range [35]. It has been also reported in nanoparticles, that the order OER activity was RuO_x > IrO_x > PtO_x, while the order for OER stability was IrO_x > PtO_x > RuO_x [36]. Therefore Ir or IrO_x have been considered as promising nanoscaled OER catalysts, as well as some works have been reported with respect to the Ir-Ru oxide based OER catalysts to utilize the high OER kinetics of RuO_2 [37–39].

1.4 Project Objective

To reduce the amount of noble metals effectively, it is typically proposed that they can be mixed with the other robust metal oxides such as catalyst supports. For the support material at the anode, high durability at the high potentials of the OER under acidic conditions is required. Carbon based supports, which have been commonly used in PEFCs, cannot be used due to the severe corrosion at such high potentials [40,41]. Various carbides and oxides have been examined as supports for noble metal catalysts at the OER; such as titanium carbides [42], silicon carbides [43,44], tantalum oxides [45], tin oxides [46,47], niobium oxides [48,49], titanium oxides [50], and manganese oxides [51]. Considering the stability at high oxygen-evolving potentials in strong acidic media and the need for high electronic conductivity, doped tin oxides have been reported as promising candidates as support materials [52,53]. Indeed, thin films and bulk powders of SnO_2 doped with Sb, Nb, Ta, In, and F have exhibited electronic conductivities ≥ 0.1 S cm^{-1}, which are sufficiently high for consideration as catalyst supports [54,55].

Recently, researchers in my laboratory succeeded in synthesizing corrosion-resistant SnO_2 supports, doped with Sb, Nb or Ta, with a fused-aggregate network structure for the cathode catalysts of PEFCs [56–59]. These supports have unique features in terms of enhanced electrical conductivity and gas diffusivity, similar to the characteristics of typical carbon black supports. For example, Pt catalysts highly dispersed on such SnO_2 supports exhibited high durability at high potentials, up to 1.5 V vs. the reversible hydrogen electrode (RHE), simulating the S-S cycling of PEFCs [56–60].

In this dissertation, it is reported that iridium based OER catalysts supported on doped tin oxides with a fused-aggregate network structure toward high performances for PEMWE. I have challenged to demonstrate the feasibility of their use as new anode catalysts, which can reduce the amount of noble metal to 1/10 compared to conventional cells with maintaining ε_v of 90% at 1 A cm^{-2}.

In ***Chapter 2***, I have synthesized two iridium based catalysts supported on niobium doped tin oxides; Ir-Pt binary and IrO_x nanoparticles. The former was used to investigate an Ir-Pt binary effect on the OER activities in an acidic electrolyte solution, and the latter was prepared to develop the iridium oxide nanoparticles with high noble metal loading catalysts.

In ***Chapter 3***, iridium based electrocatalysts highly-dispersed on doped tin oxides were examined for polarization performances on OER not only in the acidic electrolyte solution, but also in a practical PEMWE cells with the Ir loading of a level as low as 0.1 mg$_{Ir}$ cm^{-2}. It was found that the results in regard with OER activities in an acidic electrolyte solution was different from that of the practical PEMWE cells for synthesized electrocatalysts.

In ***Chapter 4***, to improve the stability for practical PEMWE cells comparable with the conventional catalyst, I have focused on the interfaces between iridium based nanoparticles and doped tin oxides. By additional heat-treatment of N_2, the interfacial solid solution, which would enhance the interaction between iridium oxide and doped tin oxide, was formed partially.

Finally I summarize the results of all chapters, and propose the guidelines in ***Chapter 5*** for "Research on Oxygen Evolution Catalysts with High Performances and Low Noble Metal Amounts for Polymer Electrolyte Membrane Water Electrolysis" entitled in this dissertation.

References

1. BP statistical review of world energy, reported by BP global (2018): https://www.bp.com/content/dam/bp/en/corporate/pdf/energy-economics/statistical-review/bp-stats-review-2018-full-report.pdf.
2. Climate change 2014 synthesis report summary for policymakers, reported by IPCC (2014): https://www.ipcc.ch/site/assets/uploads/2018/02/AR5_SYR_FINAL_SPM.pdf.
3. The adoption of the Paris Agreement (2015): https://unfccc.int/sites/default/files/english_paris_agreement.pdf.
4. T.A. Boden, G. Marland, and R.J. Andres, National CO_2 Emissions from Fossil-Fuel Burning, Cement Manufacture, and Gas Flaring. 1751-2014 (2017), DOI: 10.3334/CDIAC/00001_V2017.
5. Japan's energy 20 questions to understand the current energy situation, edited by METI Agency for Natural Resources and Energy (2017): http://www.enecho.meti.go.jp/en/category/brochures/pdf/japan_energy_2017.pdf.
6. Whitepaper for energy trends, edited by METI Agency for Natural Resources and Energy (2014) [in Japanese]: http://www.enecho.meti.go.jp/about/whitepaper/2014pdf/whitepaper2014pdf_2_1.pdf.
7. L. Carrette, K.A. Friedrich, and U. Stimming, Fuel Cells - Fundamentals and Applications. *Fuel Cells*, **1**, 5 (2001), DOI: 10.1002/1615-6854(200105)1:1<5::AID-FUCE5>3.0.CO;2-G.
8. Renewable capacity highlights, reported by IRENA (2018): https://www.irena.org/-/media/Files/IRENA/Agency/Publication/2018/Mar/RE_capacity_highlights_2018.pdf.
9. Electricity review Japan, edited by the federation of electric power companies of

Japan (2017): https://www.fepc.or.jp/library/pamphlet/pdf/04_electricity.pdf.

10. Energy carriers, prepared by Cross-ministerial Strategic Innovation Promotion Program (2016): https://www.jst.go.jp/sip/pdf/SIP_energycarriers2016_en.pdf.
11. Y. Nishimura, Hydrogen production by water electrolysis - Research, development and application of hydrogen production. *Electrochemistry*, **71**, 278 (2003) [in Japanese].
12. S. Kasahara, S. Kubo, R. Hino, K. Onuki, M. Nomura, and S. Nakao, Flowsheet study of the thermochemical water-splitting iodine–sulfur process for effective hydrogen production. *Int. J. Hydrogen Energy* **32**, 489 (2007), DOI: 10.1016/j.ijhydene.2006.05.005.
13. A. Buttler and H. Spliethoff, Current status of water electrolysis for energy storage, grid balancing and sector coupling via power-to-gas and power-to-liquids: A review. *Renew. Sustain. Energy Rev.* **82**, 2440 (2018), DOI: 10.1016/j.rser.2017.09.003.
14. The basic hydrogen strategy, prepared by METI (2017): http://www.meti.go.jp/english/press/2017/pdf/1226_003a.pdf.
15. K. Zeng and D. Zhang, Recent progress in alkaline water electrolysis for hydrogen production and applications. *Progress in Energy and Combustion Science* **36**, 307 (2010), DOI: 10.1016/j.pecs.2009.11.002.
16. I. Vincent and D. Bessarabov, Low cost hydrogen production by anion exchange membrane electrolysis: A review. *Renew. Sustain Energy Rev.* **81**, 1690 (2018), DOI: 10.1016/j.rser.2017.05.258.
17. W. Kreuter and H. Hofmann, Electrolysis: The important energy transformer in a world of sustainable energy. *Int. J. Hydrogen Energy* **23**, 661 (1998), DOI: 10.1016/S0360-3199(97)00109-2.
18. M. Carmo, D.L. Fritz, J. Mergel, and D. Stolten, A comprehensive review on PEM

water electrolysis. *Int. J. Hydrogen Energy* **38**, 4901 (2013), DOI: 10.1016/j.ijhydene.2013.01.151.

19. M.A. Laguna-Bercero, Recent advances in high temperature electrolysis using solid oxide fuel cells: A review. *J. Power Sources* **203**, 4 (2012), DOI: 10.1016/j.jpowsour.2011.12.019.
20. K. Chen and S.P. Jiang, Review—Materials degradation of solid oxide electrolysis cells. *J. Electrochem. Soc.*, **163**, F3070 (2016), DOI: 10.1149/2.0101611jes.
21. O. Schmidt, A. Gambhir, I. Staffell, A. Hawkes, J. Nelson, and S. Few, Future cost and performance of water electrolysis: An expert elicitation study. *Int. J. Hydrogen Energy* **42**, 30470 (2017), DOI: 10.1016/j.ijhydene.2017.10.045.
22. M. Faraj, M. Boccia, H. Miller, F. Martini, S. Borsacchi, M. Geppi, and A. Pucci, New LDPE based anion-exchange membranes for alkaline solid polymeric electrolyte water electrolysis. *Int. J. Hydrogen Energy* **37**, 14992 (2012), DOI: 10.1016/j.ijhydene.2012.08.012.
23. K.E. Ayers, E.B. Anderson, C.B. Capuano, M. Niedzwiecki, M.A. Hickner, C.-Y. Wang, Y. Leng, and W. Zhao, Characterization of anion exchange membrane technology for low cost electrolysis. *ECS Trans.* **45** (23), 121 (2013), DOI: 10.1149/04523.0121ecst.
24. L. An, T.S. Zhao, Z.H. Chai, P. Tan, and L. Zeng, Mathematical modeling of an anion-exchange membrane water electrolyzer for hydrogen production. *Int. J. Hydrogen Energy* **39**, 19869 (2014), DOI: 10.1016/j.ijhydene.2014.10.025.
25. M. Paidar, V. Fateev, and K. Bouzek, Membrane electrolysis–History, current status and perspective. *Electrochim. Acta* **209**, 737 (2016), DOI: 10.1016/j.electacta.2016.05.209.
26. K.E. Ayers, E.B. Anderson, C.B. Capuano, B. Caeter, L. Dalton, G. Hanlon, J. Manco,

and M. Niedzwiecki, Research advances towards low cost, high efficiency PEM electrolysis. *ECS Trans.* **33** (1), 3 (2010), DOI: 10.1149/1.3484496.

27. U. Babic, M. Suermann, F.N. Büchi, L. Gubler, T.J. Schmidt, Review—Identifying critical gaps for polymer electrolyte water electrolysis development. *J. Electrochem. Soc.* **164**, F387 (2017), DOI: 10.1149/2.1441704jes.
28. M.H. Miles and M.A. Thomason, Periodic variations of overvoltages for water electrolysis in acid solutions from cyclic voltammetric studies. *J. Electrochem. Soc.* **123**, 1459 (1976), DOI: 10.1149/1.2132619.
29. S. Trasatti, Electrocatalysis in the anodic evolution of oxygen and chlorine. *Electrochim. Acta* **29**, 1503 (1984), DOI: 10.1016/0013-4686(84)85004-5.
30. I.C. Man, H.-Y. Su, F. Calle-Vallejo, H.A. Hansen, J.I. Martinez, N.G. Inoglu, J. Kitchin, T.F. Jaramillo, J.K. Nørskov, and J. Rossmeisl, Universality in oxygen evolution electrocatalysis on oxide surfaces. *ChemCatChem.* **3**, 1159 (2011), DOI: 10.1002/cctc.201000397.
31. J. Greeley, T.F. Jaramillo, J. Bonde, I. Chorkendorff, J.K. Norskov, Computational high-throughput screening of electrocatalyticmaterials for hydrogen evolution. *Nat. Mater.* **5**, 909 (2006), DOI: 10.1038/nmat1752.
32. S.E. Fosdick, S.P. Berglund, C.B. Mullins, and R.M. Crooks, Evaluating electrocatalysts for the hydrogen evolution reaction using bipolar electrode arrays: Bi- and trimetallic combinations of Co, Fe, Ni, Mo, and W. *ACS Catal.* **4**, 1332 (2014), DOI: 10.1021/cs500168t.
33. T. Shinagawa, A.T. Garcia-Esparza, and K. Takanabe, Insight on tafel slopes from a microkinetic analysis of aqueous electrocatalysis for energy conversion. *Sci. Rep.* **5**, 13801 (2015), DOI: 10.1038/srep13801.
34. C. Spöri, J.T.H. Kwan, A. Bonakdarpour, D.P. Wilkinson, and P. Strasser, The

stability challenges of oxygen evolving catalysts: Towards a common fundamental understanding and mitigation of catalyst degradation. *Angew. Chem. Int. Ed.* **36**, 5994 (2017), DOI: 10.1002/anie.201608601.

35. R. Kötz, H.J. Lewerenz, and S. Stucki, XPS studies of oxygen evolution on Ru and RuO_2 anodes. *J. Electrochem. Soc.* **130**, 825 (1983), DOI: 10.1149/1.2119829.
36. T. Reier, M. Oezaslan, and P. Strasser, Electrocatalytic oxygen evolution reaction (OER) on Ru, Ir, and Pt catalysts: A comparative study of nanoparticles and bulk materials. *ACS Catal.* **2**, 1765 (2012), DOI: 10.1021/cs3003098.
37. S. Song, H. Zhang, X. Ma, Z. Shao, R.T. Baker, and B. Yi, Electrochemical investigation of electrocatalysts for the oxygen evolution reaction in PEM water electrolyzers. *Int. J. Hydrogen Energy* **33**, 4955 (2008), DOI: 10.1016/j.ijhydene.2008.06.039.
38. L.-E. Owe, M. Tsypkin, K.S. Wallwork, R.G. Haverkamp, and S. Sunde, Iridium–ruthenium single phase mixed oxides for oxygen evolution: Composition dependence of electrocatalytic activity. *Electrochim. Acta* **70**, 158 (2012), DOI: 10.1016/j.electacta.2012.03.041.
39. T. Audichon, T.W. Napporn, C. Canaff, C. Morais, C. Comminges, and K.B. Kokoh, IrO_2 coated on RuO_2 as efficient and stable electroactive nanocatalysts for electrochemical water splitting. *J. Phys. Chem. C* **120**, 2562 (2016), DOI: 10.1021/acs.jpcc.5b11868.
40. L.M. Roen, C.H. Paik, and T.D. Jarvi, Electrocatalytic corrosion of carbon support in PEMFC cathodes. *Electrochem. Solid-State Lett.*, **7** (1), A19 (2004) DOI: 10.1149/1.1630412.
41. T. Yoda, H. Uchida, and M. Watanabe, Effects of operating potential and temperature on degradation of electrocatalyst layer for PEFCs. *Electrochim. Acta*, **52**, 5997 (2007),

DOI: 10.1016/j.electacta.2007.03.049.

42. L. Ma, S. Sui, and Y. Zhai, Preparation and characterization of Ir/TiC catalyst for oxygen evolution. *J. Power Sources* **177**, 470 (2008), DOI: 10.1016/j.jpowsour.2007.11.106.

43. A.V. Nikiforov, A.L.T. García, I.M. Petrushina, E. Christensen, and N.J. Bjerrum, Preparation and study of IrO_2/SiC-Si supported anode catalyst for high temperature PEM steam electrolysers. *Int. J. Hydrogen Energy* **36**, 5797 (2011), DOI: 10.1016/j.ijhydene.2011.02.050.

44. A.V. Nikiforov, C.B. Prag, J. Polonský, I.M. Petrushina, E. Christensen, and N.J. Bjerrum, Development of refractory ceramics for the oxygen evolution reaction (OER) electrocatalyst support for water electrolysis at elevated temperatures. *ECS Trans.* **41** (42), 115 (2012), DOI: 10.1149/1.4718004.

45. J.-Y. Lee, D.-K. Kang, K.H. Lee, and D.Y. Chang, An investigation on the electrochemical characteristics of Ta_2O_5-IrO_2 anodes for the application of electrolysis process. *Mater. Sci. Appl.* **2**, 237 (2011), DOI: 10.4236/msa.2011.24030.

46. J. Xu, G. Liu, J. Li, and X. Wang, The electrocatalytic properties of an IrO_2/SnO_2 catalyst using SnO_2 as a support and an assisting reagent for the oxygen evolution reaction. *Electrochim. Acta* **59**, 105 (2012), DOI: 10.1016/j.electacta.2011.10.044.

47. G. Li, H. Yu, X. Wang, S. Sun, Y. Li, Z. Shao, and B. Yi, Highly effective $Ir_xSn_{1-x}O_2$ electrocatalysts for oxygen evolution reaction in the solid polymer electrolyte water electrolyser. *Phys. Chem. Chem. Phys.* **15**, 2858 (2013), DOI: 10.1039/c2cp44496h.

48. W. Hu, S. Chen, and Q. Xia, IrO_2/Nb-TiO_2 electrocatalyst for oxygen evolution reaction in acidic medium. *Int. J. Hydrogen Energy* **39**, 6967 (2014), DOI: 10.1016/j.ijhydene.2014.02.114.

49. K.S. Kadakia, P.H. Jampani, O.I. Velikokhatnyi, M.K. Datta, P. Patel, S.J. Chung,

S.K. Park, J.A. Poston, A. Manivannan, and P.N. Kumta, Study of fluorine doped (Nb,Ir)O_2 solid solution electro-catalyst powders for proton exchange membrane based oxygen evolution reaction. *Mater. Sci. Eng. B* **12**, 101 (2016), DOI: 10.1016/j.mseb.2016.06.015.

50. E. Oakton, D. Lebedev, M. Povia, D.F. Abbott, E. Fabbri, A. Fedorov, M. Nachtegaal, C. Copéret, and T.J. Schmidt, IrO_2-TiO_2: A high-surface-area, active, and stable electrocatalyst for the oxygen evolution reaction. *ACS Catal.* **7**, 2346 (2017), DOI: 10.1021/acscatal.6b03246.

51. S.D. Ghadge, P.P. Patel, M.K. Datta, O.I. Velikokhatnyi, R. Kuruba, P.M. Shanthi, and P.N. Kumta, Fluorine substituted (Mn,Ir)O_2:F high performance solid solution oxygen evolution reaction electro-catalysts for PEM water electrolysis. *RSC Adv.* **7**, 17311 (2017), DOI: 10.1039/c6ra27354h.

52. M. Pourbaix, *Atlas of Electrochemical Equilibria in Aqueous Solutions*, 2nd ed.; National Association of Corrosion Engineers (1974), ISBN: 0915567989.

53. S. Geiger, O. Kasian, A.M. Mingers, K.J.J. Mayrhofer, and S. Cherevko, Stability limits of tin-based electrocatalyst supports. *Sci. Rep.* **7**, 4595 (2017), DOI: 10.1038/s41598-017-04079-9.

54. Y. Wang, T. Brezesinski, M. Antonietti, and B. Smarsly, Ordered mesoporous Sb-, Nb-, and Ta- doped SnO_2 thin films with adjustable doping levels and high electrical conductivity. *ACS Nano* **3**, 1373 (2009), DOI: 10.1021/nn900108x.

55. H.-S. Oh, H.N. Nong, and P. Strasser, Preparation of mesoporous Sb-, F-, and In-doped SnO_2 bulk powder with high surface area for use as catalyst supports in electrolytic cells. *Adv. Funct. Mater.* **25**, 1074 (2015), DOI: 10.1002/adfm.201401919.

56. K. Kakinuma, M. Uchida, T. Kamino, H. Uchida, and M. Watanabe, Synthesis and

electrochemical characterization of Pt catalyst supported on $Sn_{0.96}Sb_{0.04}O_{2-\delta}$ with a network structure. *Electrochim. Acta* **56**, 2881 (2011), DOI: 10.1016/j.electacta.2010.12.077.

57. K. Kakinuma, Y. Chino, Y. Senoo, M. Uchida, T. Kamino, H. Uchida, S. Deki, and M. Watanabe, Characterization of Pt catalysts on Nb-doped and Sb-doped $SnO_{2-\delta}$ support materials with aggregated structure by rotating disk electrode and fuel cell measurements. *Electrochim. Acta* **110**, 316 (2013), DOI: 10.1016/j.electacta.2013.06.127.

58. Y. Senoo, K. Kakinuma, M. Uchida, H. Uchida, S. Deki, and M. Watanabe, Improvements in electrical and electrochemical properties of Nb-doped $SnO_{2-\delta}$ supports for fuel cell cathodes due to aggregation and Pt loading. *RSC Adv.* **4**, 32180 (2014), DOI: 10.1039/c4ra03988b.

59. Y. Senoo, K. Taniguchi, K. Kakinuma, M. Uchida, H. Uchida, S. Deki, and M. Watanabe, Cathodic performance and high potential durability of Ta-$SnO_{2-\delta}$-supported Pt catalysts for PEFC cathodes. *Electrochem. Commun*. **51**, 37 (2015), DOI: 10.1016/j.elecom.2014.12.005.

60. Y. Chino, K. Taniguchi, Y. Senoo, K. Kakinuma, M. Hara, M. Watanabe, and M. Uchida, Effect of added graphitized CB on both performance and durability of Pt/Nb-SnO_2 cathodes for PEFCs. *J. Electrochem. Soc.*, **162**, F736 (2015), DOI: 10.1149/2.0651507jes.

Chapter 2: Development of Highly Dispersed Iridium Based Nanocatalysts on Doped Tin Oxides

2.1 Introduction

As the first approach to reduce the amount of noble metals with maintaining high voltage efficiency (ε_V), an effect of composition of Ir-Pt binary catalysts on the OER activities has been examined in an acidic electrolyte solution. IrO_2 and Pt black powders have been used as conventional catalysts for the oxygen evolution reaction (OER) in the PEMWE. The OER activities of Ir-Pt binary or Ir-Pt-Ru ternary systems have been investigated by several groups [1–5], and it has been reported that the OER activity might be enhanced due to the Ir-Pt alloy effect [5].

In ***Chapter 2***, new OER catalysts were prepared by dispersing Ir-Pt binary nanoparticles on Nb-SnO_2 support with a fused-aggregated structure by the use of a nanocapsule method as well as a colloidal method. In my laboratory, Pt or Pt-alloy nanoparticles have been uniformly dispersed on carbon or oxide supports with well-controlled size and composition by the nanocapsule method [6,7]. This is because the all metal precursors (Pt and alloying components) were confined within the limited reaction space in reverse micelles (nanocapsule), followed by the simultaneous reduction by a strong reducing agent. Characteristics of Ir-Pt/Nb-SnO_2 are shown in this chapter.

In addition, a colloidal method in aqueous media was used to develop the highly-dispersed iridium oxide (IrO_x) nanoparticles with high noble metal loading catalysts, because hydrated/oxidized iridium might be affinitive electrostatically with tin oxides during the oxidative reaction, due to the good hydrophilicity of Nb-SnO_2 support compared to the graphitized carbon support [8].

2.2 Experimental Methods

2.2.1 Synthesis

The Nb-SnO_2 support with the fused-aggregate network structure was prepared by the flame pyrolysis method [9,10]. The projected composition was $Sn_{0.96}Nb_{0.04}O_{2-\delta}$, where δ is the mole fraction of oxygen deficiencies, corresponding to that with the highest electronic conductivity. The resulting oxides were heat-treated at 800°C for 2 h in air using a rotary kiln furnace.

Ir-Pt binary nanoparticles were loaded on the Nb-SnO_2 support (Ir_yPt_{100-y}/Nb-SnO_2) by the nanocapsule method [6,7] as shown in **Scheme 2-1**. $Ir(acac)_3$ and $Pt(acac)_2$ were used as the precursors, and the solvent used was diphenyl ether. The projected value of total metal loading on Nb-SnO_2 was 20 wt%, and the molar ratio of metal salt(s) to surfactant (oleylamine and oleic acid) was adjusted at 1.0 for all samples. Nb-SnO_2 support dispersed in diphenyl ether was added after the reduction reaction step. The product was filtered and washed with ethanol several times. The black powders thus obtained were heated at 200°C for 4 h in 5% H_2/N_2 balance atmosphere and at 150°C for 30 min in vacuum. This method of heat treatments was similar manner to the Pt/Nb-SnO_2 system [7].

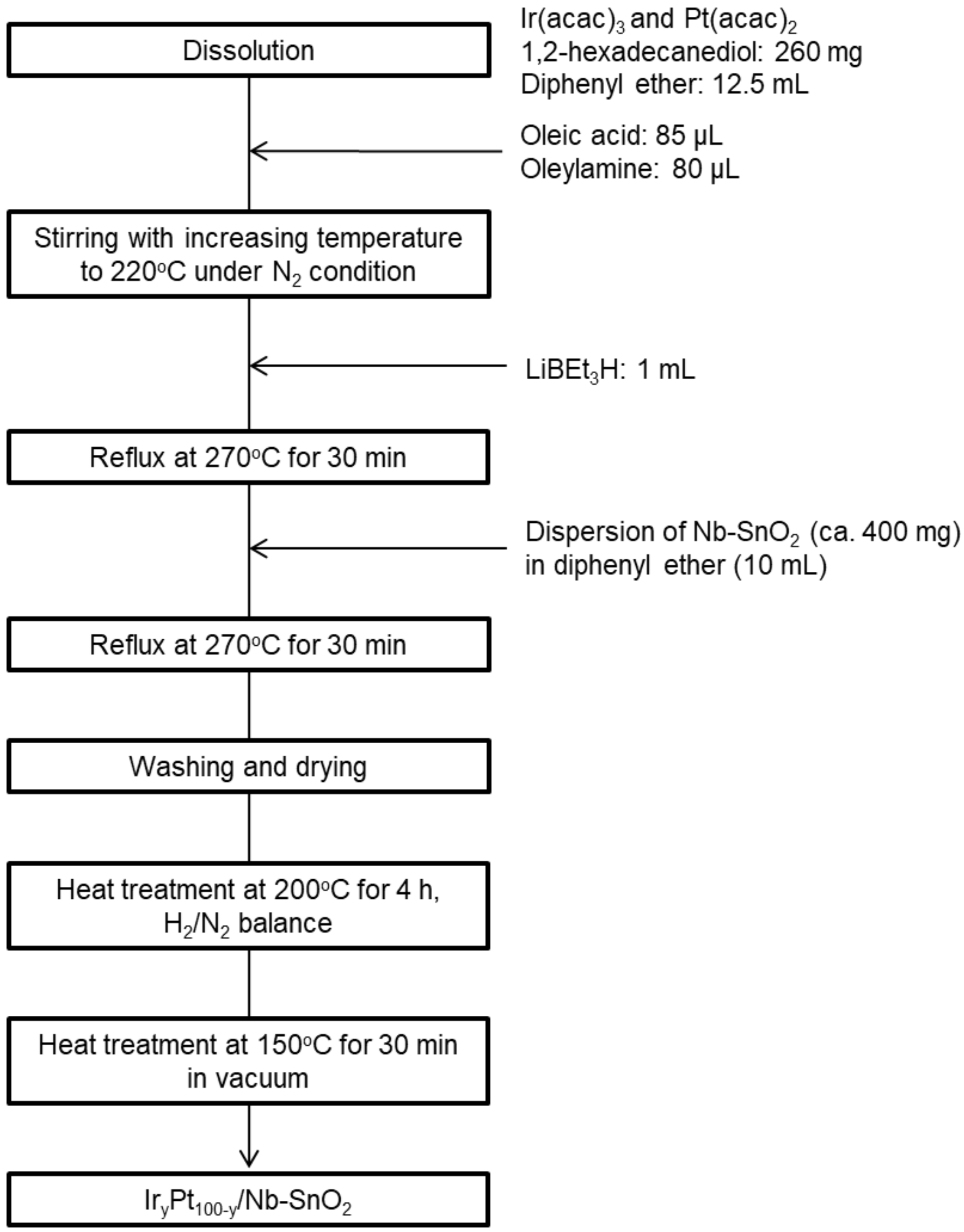

Scheme 2-1. Synthesis of $Ir_yPt_{100-y}/Nb\text{-}SnO_2$ binary catalyst by the nanocapsule method.

Oxidized iridium nanoparticles loaded on the Nb-SnO_2 support (IrO_x/Nb-SnO_2) were prepared by a colloidal method [9,11] as shown in **Scheme 2-2**. The projected value of iridium metal loading on Nb-SnO_2 was 20 wt%. H_2IrCl_6 was dissolved in pure water (18.2 MΩ, Milli-Q, Millipore Japan Co.). Powdered $NaHSO_3$ was added to H_2IrCl_6 aqueous solution as the reducing agent, accompanied by the evolution of HCl, probably due to the formation of sulfite [11]. With maintaining the pH of the solution at ca. 5.0 by an addition of NaOH solution (5 wt%), H_2O_2 solution (used as received, ca. 30% in concentration) as an oxidant was added dropwise with 2 mL min^{-1} to the solution. The Nb-SnO_2 support was dispersed in pure water, followed by mixing with the IrO_x colloidal solution. The temperature of the dispersion was then increased to 90°C and maintained for 3 or 18 h with stirring (ageing). The suspension was filtered and washed with pure water to remove chlorides thoroughly. The blue powder thus obtained was dried at 60°C in an oven, denoted as IrO_x/Nb-SnO_2 (AP) catalyst, while IrO_x/Nb-SnO_2 (150H_2) catalyst (black powder) was additionally prepared by a heat treatment at 150°C for 2 h under 5% H_2/N_2 balance atmosphere. The temperature of 150°C was set to be same as the Pt/Nb-SnO_2 and Pt/Sb-SnO_2 catalysts in PEFC [8,9].

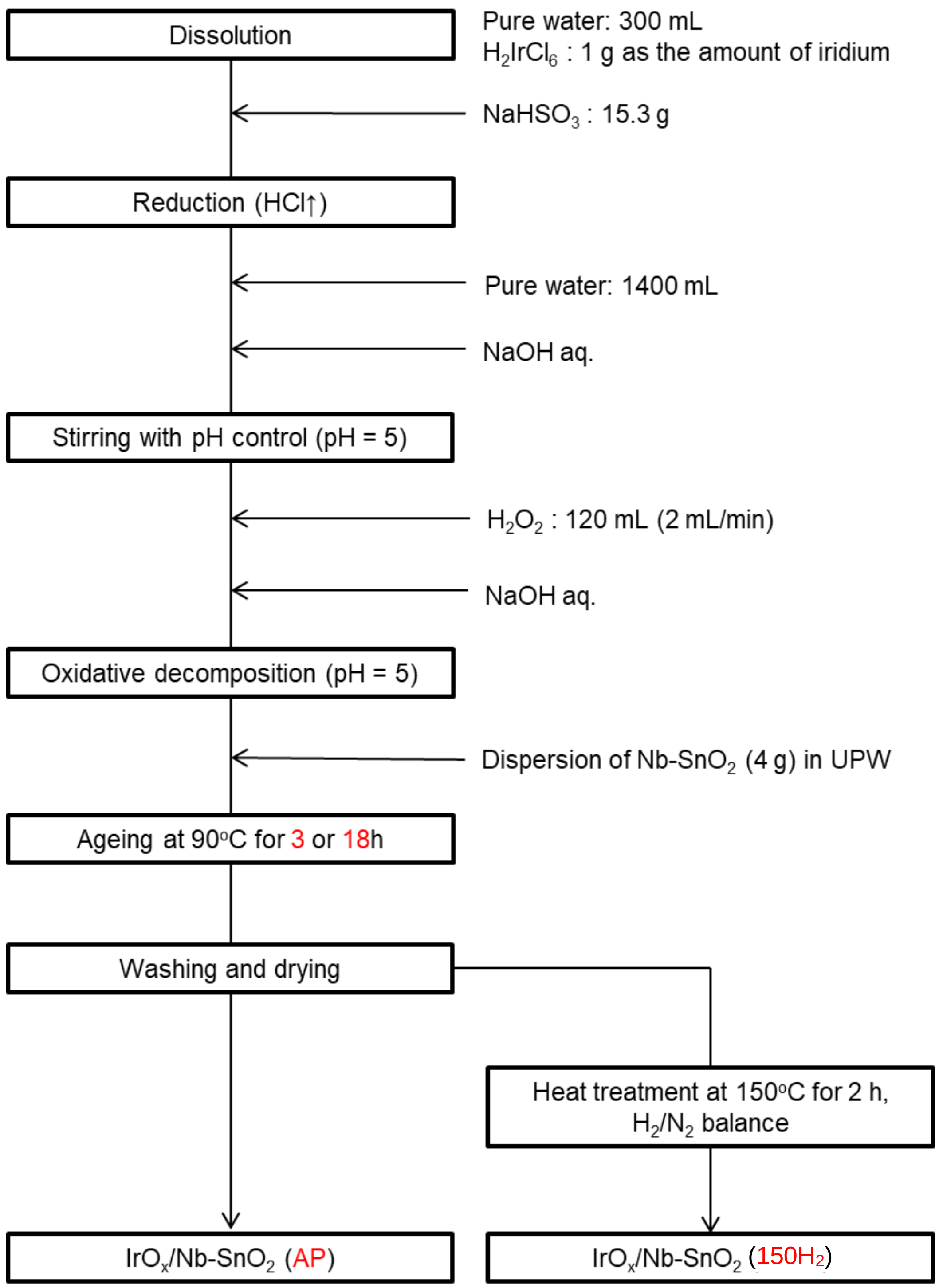

Scheme 2-2. Synthesis of IrO_x/Nb-SnO_2 catalyst by the colloidal method.

2.2.2 Measurements of Physical Properties

The surface areas of the Nb-SnO_2 support was measured by Brunauer-Emmett-Teller (BET) method equipped with N_2 adsorption system (BELSORP-mini, Nippon BEL Co.). Crystallographic structures and crystallite sizes of the samples were analyzed by X-ray diffraction (XRD; Ultima IV, Rigaku Co.) with Cu-Kα radiation (40 kV, 40 mA). The samples were also characterized by a transmission electron microscope (TEM; H-9500, Hitachi High-Technologies Co.) with an acceleration voltage of 200 kV and an emission current of ~ 0.4 μA. The average diameter and size distributions of the loaded nanoparticles were estimated from ca. 300 particles in more than six TEM images with 150 × 150 nm areas.

The amount of Ir metal in IrO_x/Nb-SnO_2 catalyst was quantitatively analyzed by the use of inductively coupled plasma methods with optical emission spectroscopy (ICP-OES; iCAP6300Duo, Thermo Fisher Scientific K.K.) or mass spectroscopy (ICP-MS; 7500CX, Agilent Technologies Inc.) after pretreatment by the alkaline carbonate-fusion method. This pretreatment was used in order to dissolve the catalyst completely, including IrO_x nanoparticles and tin oxide supports. To estimate the content of $Ir^{(IV)}$, the electronic states of iridium in the IrO_x/M-SnO_2 were characterized by X-ray photoelectron spectroscopy (XPS; JPS-9010, JEOL Co., Ltd.) with Mg-Kα radiation (10 kV, 30 mA).

2.2.3 Electrochemical Measurements in Electrolyte Solution (Half-Cell)

The electrochemical properties of the Ir_yPt_{100-y}/Nb-SnO_2 and IrO_x/Nb-SnO_2 catalysts in 0.1 M $HClO_4$ electrolyte solution was examined by the use of a channel flow electrode cell (CFE; a half-cell method) [12,13]. The working electrode was contained of the catalyst dispersed uniformly on an Au substrate (flow direction length 1 mm × width 4 mm) with a ca. two-monolayer height of the Nb-SnO_2 support particles, assuming the average diameter of the support was 30 nm (ca. 42 μg cm^{-2}). The amount of Nb-SnO_2 support in Ir_yPt_{100-y}/Nb-SnO_2 catalyst could be determined by the subtraction of those of Ir and Pt from 100 wt% quantified by ICP, whereas in case of IrO_x/Nb-SnO_2, it was calculated by the subtraction of that of IrO_x analyzed by combination with ICP and XPS (see **Appendix 2-1**). Then a Nafion® solution was pipetted onto the catalyst layer to yield an average film thickness of 0.1 μm, followed by heat treatment at 130°C for 30 min in air as same as the method in PEFC [13]. A platinum mesh was used as the counter electrode, and a reversible hydrogen electrode (RHE) was used as the reference electrode. All electrode potentials in ***Chapter 2*** referred to the RHE.

The electrolyte solution of 0.1 M $HClO_4$ was purified in advance by conventional pre-electrolysis in order to avoid the influence of impurities [14]. With the use of a potentiostat (HA1010mM8, Hokuto Denko), the OER activity of each catalyst was examined by linear sweep voltammetry (LSV) at a sweep rate of 10 mV s^{-1} in circulated 0.1 M $HClO_4$ at 80°C. The AC impedance of the electrolyte solution was measured at 0.8 V by a frequency response analyzer (SI 1287 with SI 1260, Solartron Analytical) with a modulation amplitude of 10 mV in the frequency range from 10 kHz to 1 Hz.

For the conventional catalyst, a mixture of commercial IrO_2 (Tokuriki Honten Co., Ltd.) and Pt black (Ishifuku Metal Industry Co., Ltd.) powder were used with 1:1 in mass ratio, and additionally observed by a scanning electron microscope (SEM; SU9000, operated at 30 kV, Hitachi High-Technologies Co.) and TEM. In the OER activity test by the use of a half cell, this conventional catalyst with a noble metal loading of 100 μg_{Ir+Pt} cm^{-2} on Au substrate was used as a reference.

2.3 Results and Discussion: Effect of Ir-Pt composition on the OER activity

2.3.1 Physical Properties of the Ir-Pt/Nb-SnO_2 Catalysts

Figure 2-1 shows a typical TEM image of Nb-SnO_2 support. It was observed that the support had a chain-like structure with random branching of the particles, so-called a fused-aggregate network structure. The surface areas of the Nb-SnO_2 support measured by the BET method was 30 $m^2\ g^{-1}$.

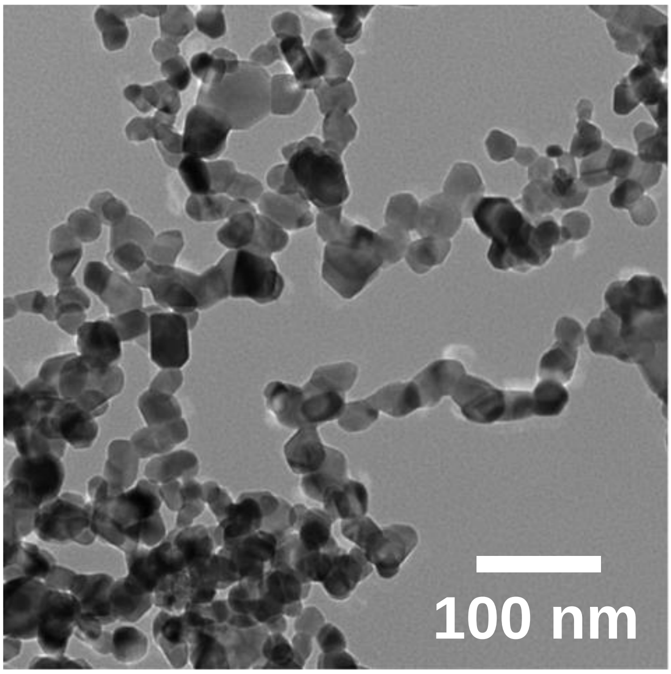

Figure 2-1. A TEM image of the Nb-doped SnO_2 support with a fused-aggregate network structure.

Figure 2-2 shows TEM images of a series for $Ir_yPt_{100-y}/Nb\text{-}SnO_2$ catalysts, where y is atom% of Ir (projected value). Ir-Pt binary nanoparticles of ca. 1 ~ 6 nm in diameter were found to be dispersed on the oxide supports. The average particle size for $Ir/Nb\text{-}SnO_2$ catalyst was very small specifically.

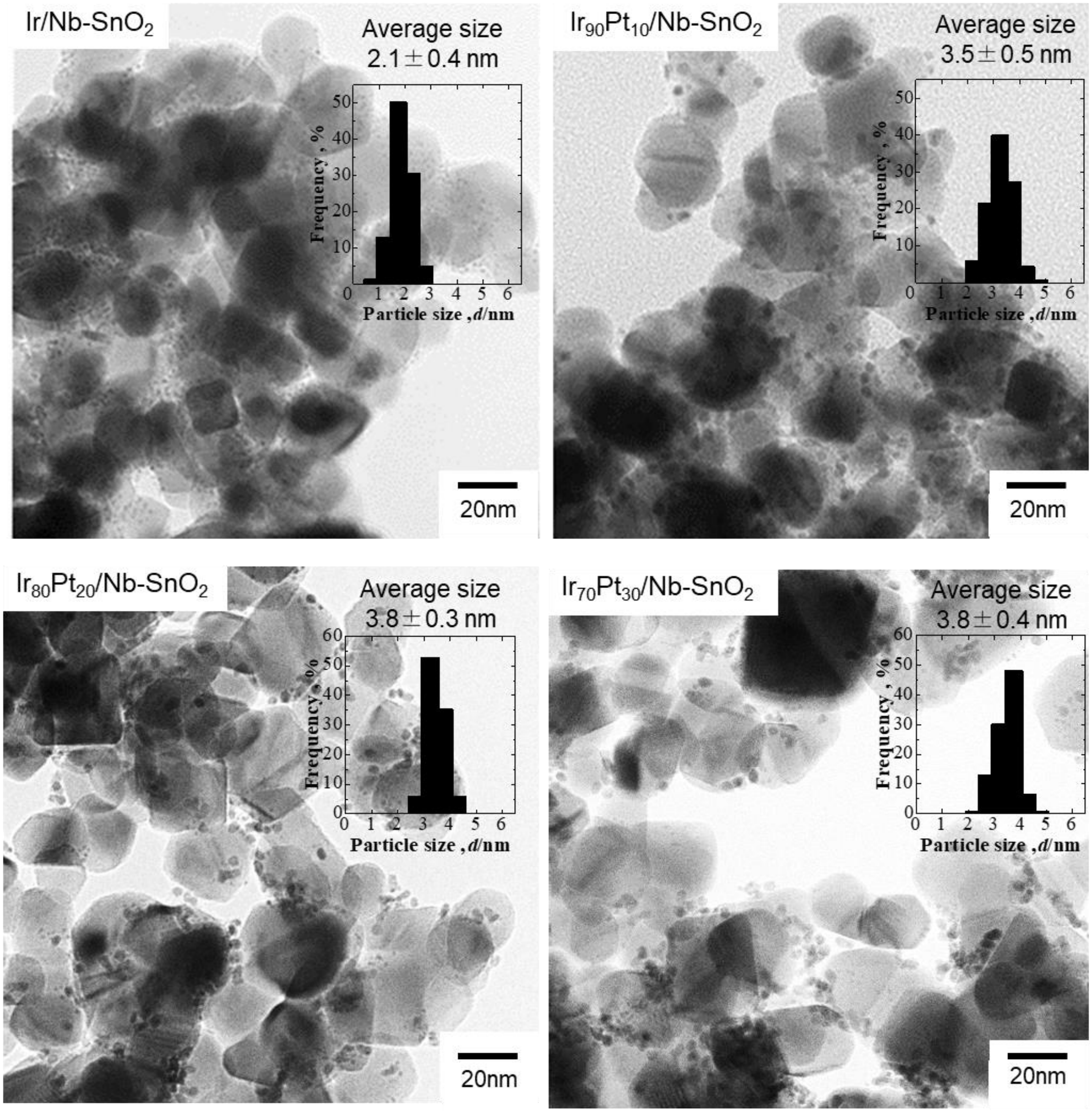

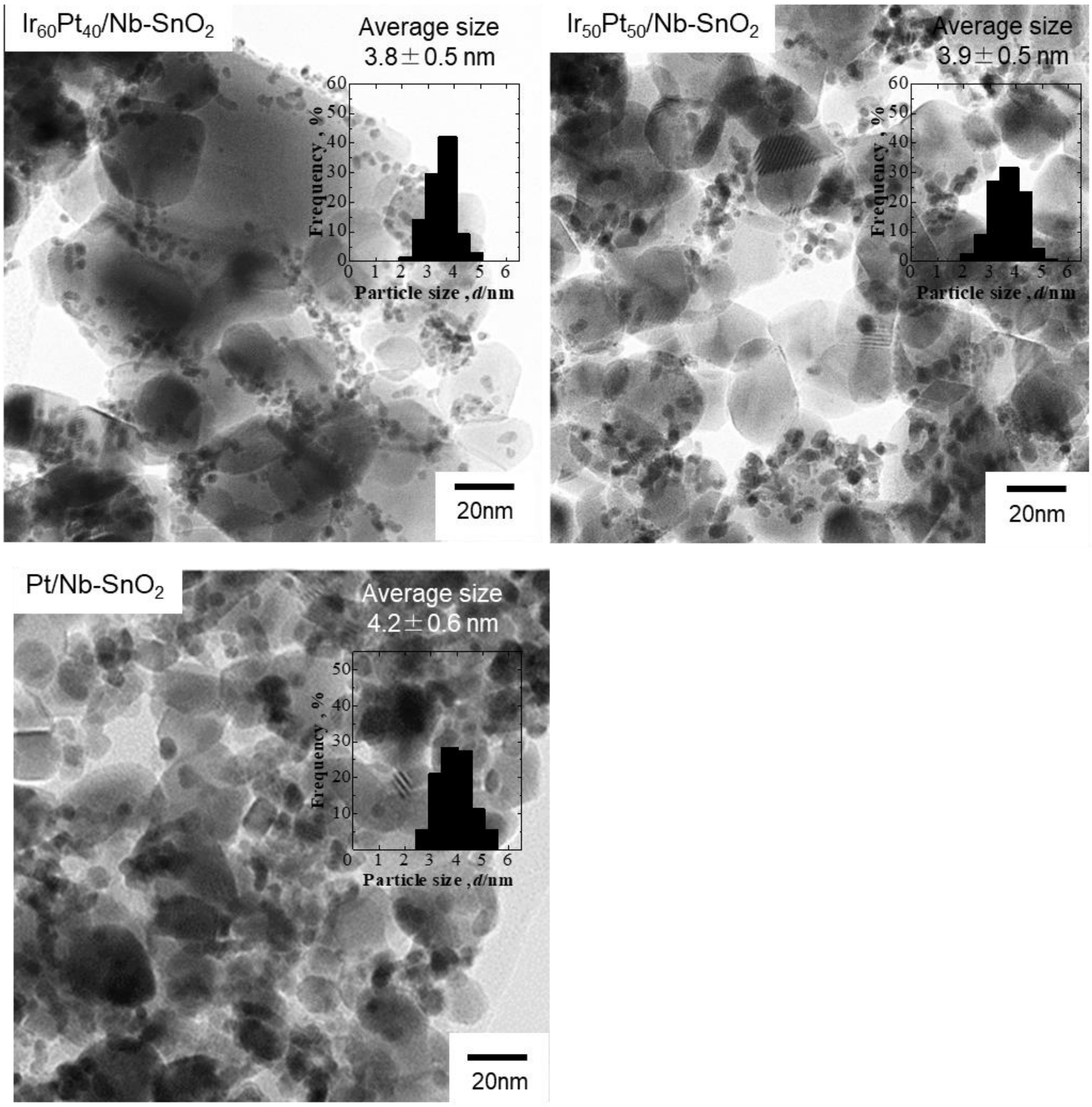

Figure 2-2. TEM images and particle size distribution histograms for Ir_yPt_{100-y}/Nb-SnO_2 catalysts, where y represents atom% of Ir (projected composition). The average diameter and size distribution of Ir-Pt particles were estimated from ca. 300 particles in several TEM images.

XRD patterns of Ir_yPt_{100-y}/Nb-SnO_2 catalysts are shown in **Figure 2-3**. The crystallite sizes of Nb-SnO_2 estimated from the peak at 2θ = ca. 34° was 16 nm. The peaks around 40°, 47°, and 68° were assigned to Pt and/or Ir metal with a fcc structure for Pt and Ir-Pt catalysts, while peaks assigned to Ir fcc structure were not observed for Ir/Nb-SnO_2. This might be because the crystallite size of Ir was too small to be detected by XRD. It was difficult to identify the alloying of Ir with Pt because lattice constants for Ir and Pt were too close (390 and 392 pm, respectively).

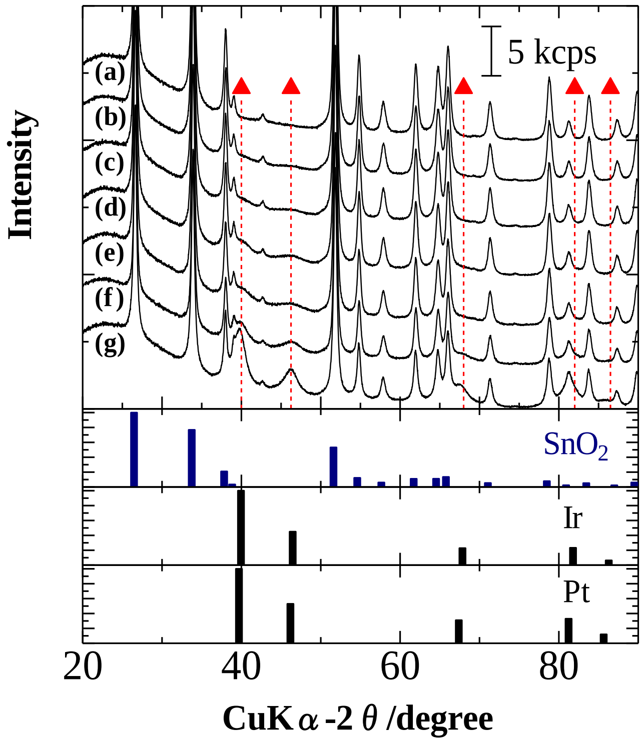

Figure 2-3. XRD patterns of Ir_yPt_{100-y}/Nb-SnO_2 catalysts: y = (a) 100, (b) 90, (c) 80, (d) 70, (e) 60, (f) 50, and (g) 0, respectively (y represents the projected composition). ▲ corresponds diffraction peaks of fcc Ir.

The average diameter of Ir-Pt binary particles estimated from TEM, composition (Ir content) and noble metal loading evaluated by ICP-MS for Ir_yPt_{100-y}/Nb-SnO_2 catalysts are summarized in **Table 2-1**. The content of Ir was much smaller than that projected. **Figure 2-4** shows the average particle sizes and metal loadings as a function of Ir content. The average size decreased nearly linearly with Ir content, and the metal loading deceased with increasing the Ir content. The reason for such dependences is not clear, but it was rather difficult to control the composition and the loading amount by the nanocapsule method.

Table 2-1 Average diameter of Ir-Pt particles estimated from TEM, Ir content and noble metal loading evaluated by ICP for Ir_yPt_{100-y}/Nb-SnO_2 catalysts.

Ir content (at%, projected)	Average diameter (nm)	Ir content (at%)	Metal loading (wt%)
100 (Ir)	2.1 ± 0.4	-	1.8
90	3.5 ± 0.5	35.3	2.1
80	3.8 ± 0.3	29.2	4.7
70	3.8 ± 0.4	23.3	8.5
60	3.8 ± 0.5	20.4	9.9
50	3.9 ± 0.5	11.7	10.7
0 (Pt)	4.2 ± 0.6	-	15.3

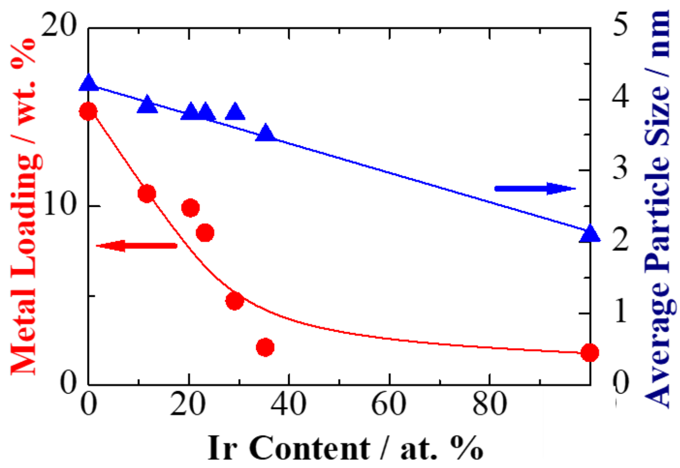

Figure 2-4. Average particle size and noble metal loading with respect to Ir content (evaluated values) in Ir_yPt_{100-y}/Nb-SnO_2.

2.3.2 Dependence of Ir Composition on OER Activity for Ir-Pt Binary Catalysts

The OER activities of Ir_yPt_{100-y}/Nb-SnO_2 catalysts were examined by the CFE technique. **Figure 2-5** (a) shows the anodic polarization curves for Ir_yPt_{100-y}/Nb-SnO_2 and Au substrate in N_2-saturated 0.1 M $HClO_4$ at 80°C, in which the current was shown by the current density (*j*) based on the geometric area of Au substrate. Since a small anodic current of Au substrate, which can be ascribed to the oxidation of Au and O_2 evolution, it was subtracted as the base-line from the original current-potential (*I*–*E*) curves. **Figure 2-5** (b) shows LSVs, which the current axis is shown by the apparent mas activity (*MA*) based on the current per mass of Ir+Pt loaded on the electrode substrate.

In the present work, *MA*s at 1.5 V ($MA_{1.5}$) was applied to compare the OER activities. It has been reported for a PEMWE operated at 1 A cm^{-2} that the potential of the Pt/C cathode for the hydrogen evolution reaction at 90°C with 0.7 mg_{Pt} cm^{-2} was −0.05 V [15] and the *iR* loss, mainly due to Nafion® 117, was ca. 0.1 V [16]. Taking these values from literature and the anode potential of 1.5 V for the OER, the cell potential can be estimated to be 1.65 V at 1 A cm^{-2}, which corresponds to ε_v of 90%. **Figure 2-6** shows $MA_{1.5}$ for the catalysts as a function of Ir content. The $MA_{1.5}$ values increased with Ir content. Specifically, Ir (100 at% Ir)/Nb-SnO_2 catalyst exhibited a very high activity, 7.8 A mg_{Ir}^{-1}, which is about 4 times larger than that of 35 at% Ir. This is consistent with literature reporting that the OER activity of Ir-Pt binary catalysts decreased by the presence of Pt or oxidized Pt [3,17]. Hereinafter, I focused on Ir-based (metal or oxidized Ir) nanoparticles dispersed on doped SnO_2, and examined the catalysts by a colloidal method.

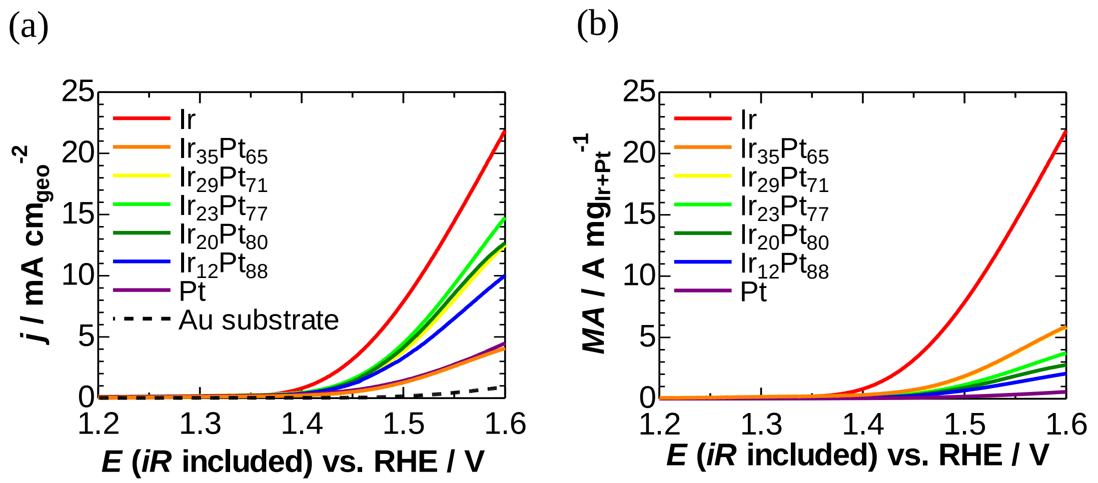

Figure 2-5. LSVs (*iR*-included) for O_2 evolution at Ir_yPt_{100-y}/Nb-SnO_2 (y represents the evaluated composition) and Au substrate in N_2-saturated 0.1 M $HClO_4$ at 80°C at 10 mV s^{-1} and 26 cm s^{-1}. (a) The current density (*j*) is based on the geometric area of the Au substrate of the working electrode (4 mm^2). (b) The current was shown by the apparent mass activity (*MA*) based on the mass of Ir+Pt loaded on the substrate.

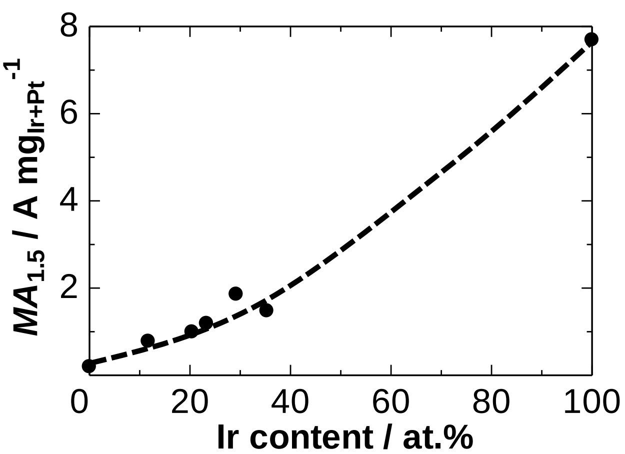

Figure 2-6. *MA*s at 1.5 V ($MA_{1.5}$) of a series in Ir_yPt_{100-y}/Nb-SnO_2 catalysts as a function of Ir content (evaluated values).

2.4 Results and Discussion: OER Activities of Iridium Oxide Nanocatalysts Prepared by the Colloidal Method

2.4.1 Physical Properties of IrO_x/Nb-SnO_2 Catalysts

Figure 2-7 shows TEM images of AP and 150H_2 catalysts for IrO_x/Nb-SnO_2 synthesized by a colloidal method with ageing time for 3 or 18 h. The dispersion of nanoparticles on the Nb-SnO_2 supports were found to be more uniform than the case of those synthesized by the nanocapsule method shown in **Figure 2-2**.

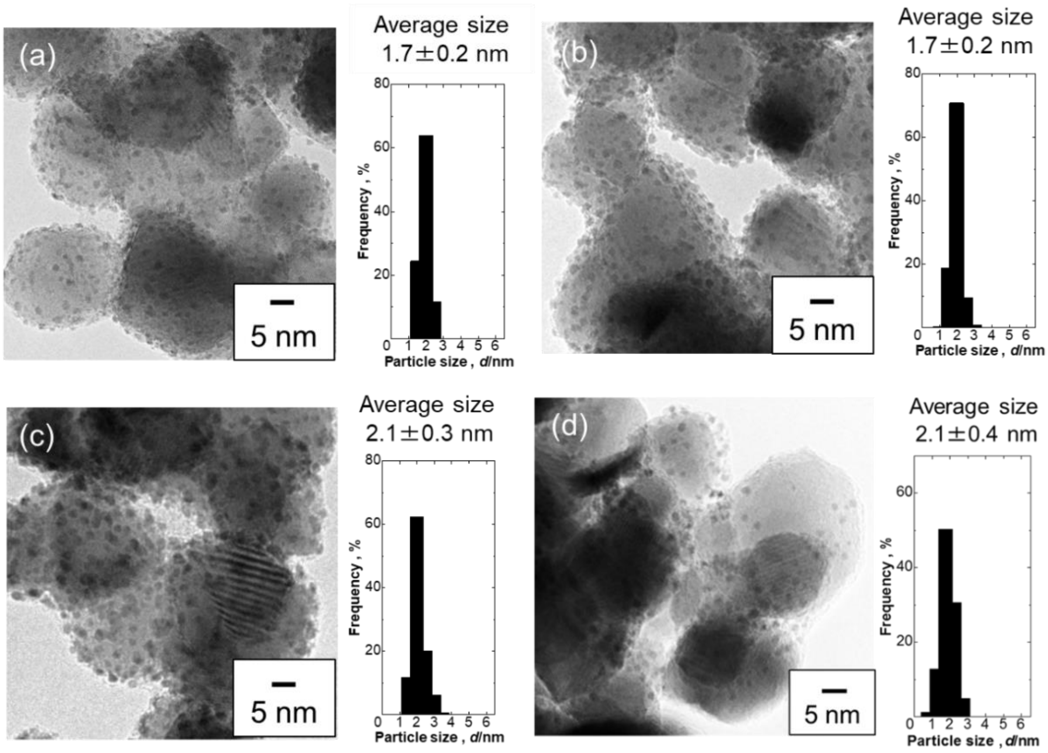

Figure 2-7. TEM images and particle size distribution histograms for IrO_x/Nb-SnO_2 catalysts prepared by colloidal method; (a) AP with 3 h ageing, (b) 150H_2 with 3 h ageing, and (c) 150H_2 with 18 h ageing. (d) Those of Ir/Nb-SnO_2 catalyst synthesized by nanocapsule method.

The average sizes of the Ir or IrO_x nanoparticles (d_{Ir}) for 3 h ageing were unchanged even after H_2 treatment at 150°C as shown in **Figure 2-7** (a) and (b). With increasing the ageing time to 18 h, the values of d_{Ir} increased from 1.7 to 2.1 nm. The amount of Ir metal in IrO_x/Nb-SnO_2 with the ageing time for 3 and 18 h was quantified to be 6.5 and 11.3 wt%, respectively. These values were larger than that of Ir/Nb-SnO_2 catalyst synthesized by the nanocapsule method. SEM and TEM images of commercial IrO_2 and Pt particles (for the conventional catalyst) are shown in **Figure 2-8**.

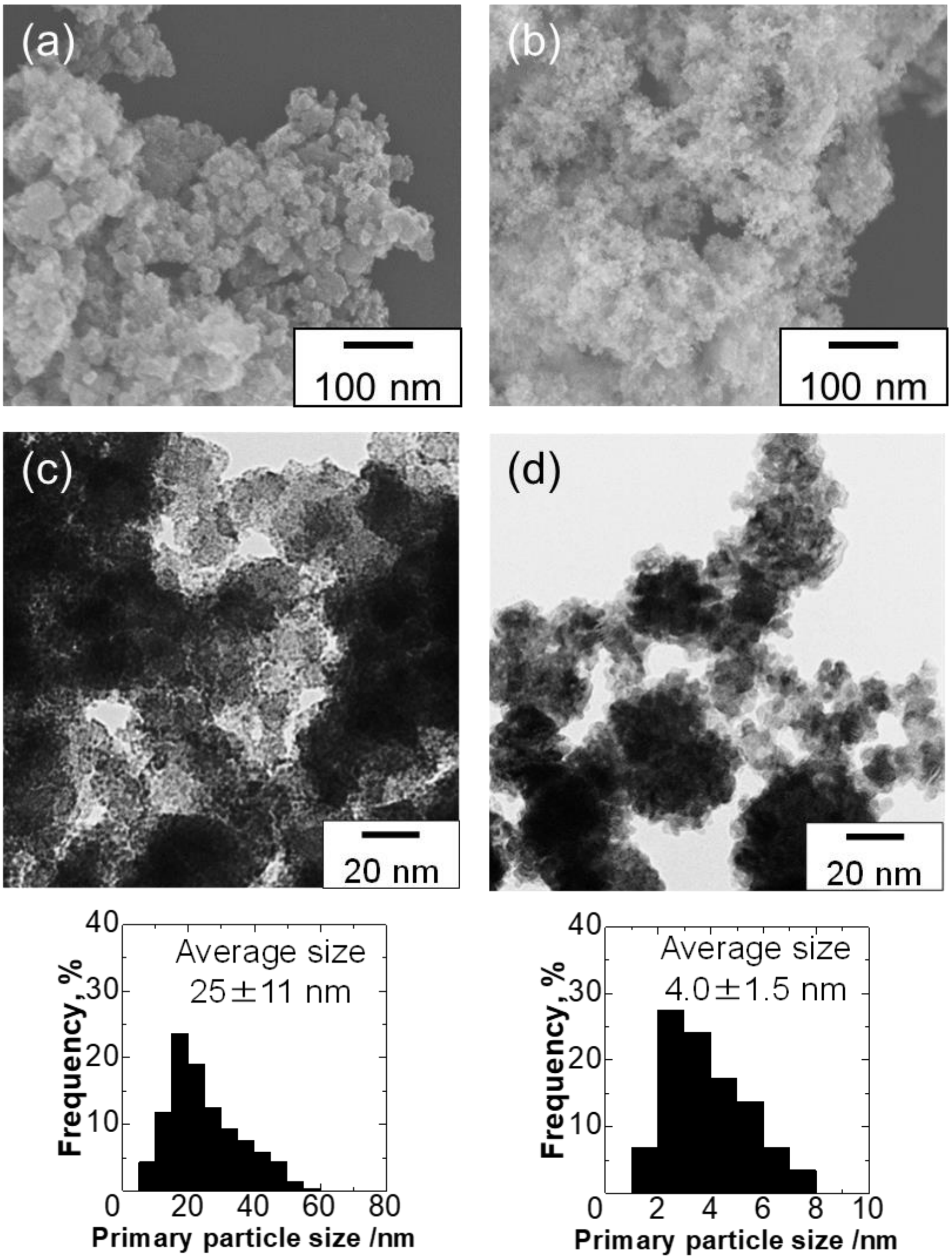

Figure 2-8. SEM and TEM images, and particle size distribution histograms (primary particles) for conventional catalysts: (a,c) commercial IrO_2 and (b,d) commercial Pt black.

To estimate the ratio of Ir^0 and $Ir^{(IV)}$ (IrO_2), XPS measurements were carried out. **Figure 2-9** shows a XP spectrum for the 150H_2 (18 h ageing) catalyst as an example. Peaks around 64 and 60 eV were assigned to Ir $4f_{5/2}$ and $4f_{7/2}$. By the deconvolution of the peaks into symmetric Gaussian ones, the ratio of metallic Ir^0 and $Ir^{(IV)}$ was obtained [18]. The contents of $Ir^{(IV)}$ (corresponding to IrO_2) were quantitative analyzed to be 81, 29, 16 and 100 at% in AP (3 h ageing), 150H_2 (3 h ageing), 150H_2 (18 h ageing) and commercial IrO_2 catalysts, respectively.

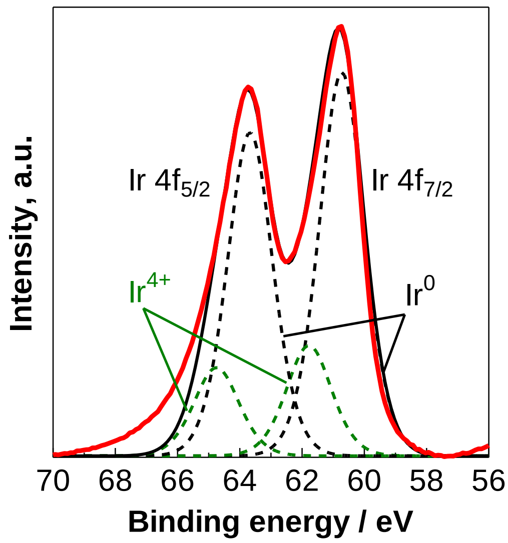

Figure 2-9. A XP spectrum of Ir $4f_{5/2}$ and $4f_{7/2}$ at the 150H_2 (18 h ageing) powder. The binding energy was corrected by referring to C 1s at 284.2 eV. Deconvolution of peaks into metallic Ir^0 and $Ir^{(IV)}$ (IrO_2) components.

Because H_2IrCl_6 was used as the precursor in the synthesis, it was essential to remove Cl species from the catalysts to avoid Cl_2 evolution, which complicates the evaluation of OER activity. By a careful inspection by XP survey spectrum as shown in **Figure 2-10**, it was confirmed that the content of Cl species was less than the detection level by XPS.

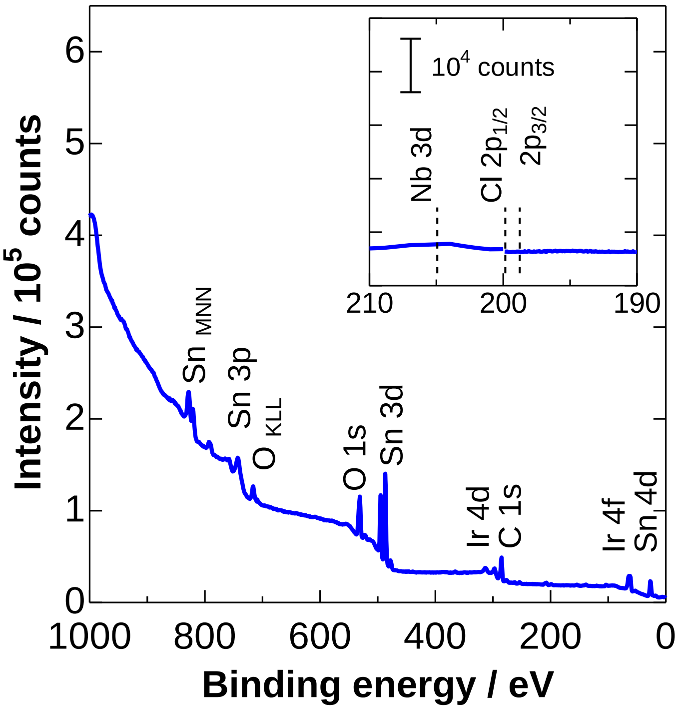

Figure 2-10. An example of XP survey spectrum of $150H_2$ with 18 h ageing for IrO_x/Nb-SnO_2 catalyst. The inset shows a magnified spectrum for detecting Cl 2p (no signals). The binding energy was corrected by referring to C1s at 284.2 eV.

2.4.2 OER Activities and Durabilities of IrO_x/Nb-SnO_2 Catalysts

Figure 2-11 shows *MA*s for the OER on IrO_x/Nb-SnO_2 catalysts prepared by the colloidal method. Interestingly, it was found that the $MA_{1.5}$ for 150H_2 (3 h ageing) catalyst was ca. 1.3-fold higher than those of 150H_2 (18 h ageing) and Ir/Nb-SnO_2 (synthesized by nanocapsule method) catalyst. This was possibly ascribed to the increase in the surface area for OER, because the d_{Ir} value of 150H_2 (3 h ageing) catalyst was 1.7 nm, which was smaller than those of 150H_2 (18 h ageing) and Ir/Nb-SnO_2 (d_{Ir} = 2.1 nm). To compare their values, specific surface areas of IrO_2 (S_{IrO2}) for IrO_x/Nb-SnO_2 and Ir/Nb-SnO_2 were calculated. Rutile IrO_2, that is the thermodynamically stable species at OER potentials in acidic media [19], was selected since the surface and/or interior of the nanoparticles on Nb-SnO_2 can be converted to IrO_2 during steady-state OER operation. Then, the surface coverage of IrO_2 on the particles could be calculated by estimating the ratio of surface atoms to the total number of atoms ($N_{surface}/N_{total}$), assuming that fcc Ir particles have an ideal cubo-octahedral shape. The calculation method is shown in **Appendix 2-2**. For the case of 150H_2 catalysts (18 h ageing, d_{Ir} = 2.1 nm) as an example, the value of $N_{surface}/N_{total}$ for 2.1 nm particles were calculated to be 52%. Thus the $Ir^{(IV)}$ value of 16% can be rationally explained if the surface atoms of 31% (= 16/52) was oxidized to IrO_2 in the as-synthesized (before OER tests) catalyst. If all of the surface atoms were oxidized to IrO_2 with an Ir metal core during the OER, the initial particle sizes would be nearly unchanged. Therefore, the value of S_{IrO2} (on an Ir metal core) was estimated to be 127 $m^2\ g_{Ir}^{-1}$. On the other hand, if all Ir atoms in the particle were oxidized to IrO_2 during the OER, the particle size (d_{IrO2}) could increase from 2.1 to 2.7 nm while maintaining a constant N_{total}, resulting in a value of 98 $m^2\ g_{Ir}^{-1}$. The calculated values of were summarized in **Table 2-2**. Note that it was assumed that the nanocapsule (Ir/Nb-SnO_2) catalyst involved no or less $Ir^{(IV)}$ content (not measured) than the $N_{surface}/N_{total}$ ratio (52%) and thus the value of

d_{IrO2} was increased from 2.1 to 2.7 nm, whereas the value of d_{IrO2} was assumed to be similar as the value of d_{Ir} because the particles were consisted of IrO_2 mainly (81%) in case of AP catalyst. From **Table 2-2**, the increase in S_{IrO2} of the $150H_2$ (3 h ageing) catalyst could be estimated by a factor of 1.2, compared with those of $150H_2$ (18 h ageing) and nanocapcule catalysts. This value is coincide well with the increase in the OER activity.

Moreover it was found that $MA_{1.5}$ of $150H_2$ (3 h ageing) catalyst exhibited ca. twice higher than AP, despite same values of d_{Ir}. One of the possible reason is an IrO_x shell on an Ir core exhibits higher OER activity than IrO_x as reported previously [20,21]. However in comparison with ageing time, larger Ir metal loading for 18 h aged catalyst (11.3 wt%) than 3 h ageing one (6.5 wt%) was detected. For a practical measurement of the performance in MEA, it was argued that the increase of Pt loading on the Nb-SnO_2 support from 9 wt% to 17 wt% was effective in decreasing the ohmic resistance and in improving the cell performance in the PEFCs [22]. Therefore $150H_2$ with 18 h aged catalyst for the IrO_x/Nb-SnO_2 was used to compare the conventional catalyst hereinafter.

Next, the effect of flow rate of the electrolyte solution on the OER current was examined. LSVs for IrO_x/Nb-SnO_2 ($150H_2$, 18 h ageing) catalyst measured in N_2-saturated 0.1M $HClO_4$ solution at 80°C with various flow rates from 26 to 220 cm s^{-1} are shown in **Figure 2-12**. The OER currents increased with increasing flow rate and nearly levelled off for flow rates $\geq$ 160 cm s^{-1}. This suggests that oxygen gas bubbles were effectively removed from the surface at large flow rate. Thus the flow rate of 160 cm s^{-1} was adopted for the OER measurements with LSVs.

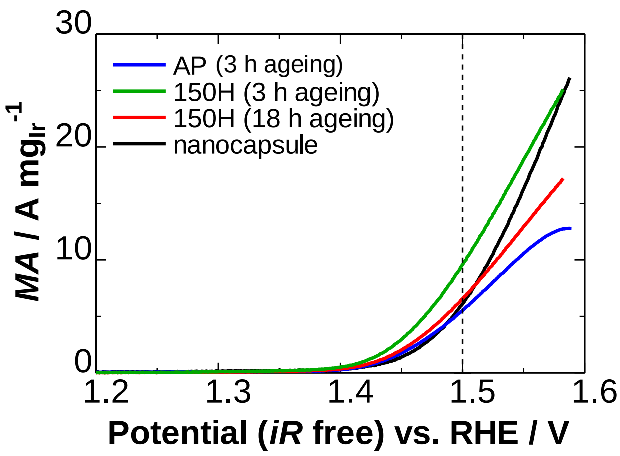

Figure 2-11. LSVs for O_2 evolution at a series of IrO_x/Nb-SnO_2 prepared by colloidal method in N_2-saturated 0.1 M $HClO_4$ at 80°C with a scan rate of 10 mV s^{-1} and 26 cm s^{-1}. For comparison, LSV of Ir/Nb-SnO_2 synthesized by nanocapsule method was added (see **Figure 2-5**).

Table 2-2 Diameters of IrO_x or Ir nanoparticles estimated by TEM (d_{Ir}), diameters of IrO_2 (d_{IrO2}), specific surface areas of IrO_2 for the IrO_2 shell/Ir metal core model ($S_{IrO2/Ir}$) and for the completely oxidized model (S_{IrO2}).

<table>
<tr><th>Sample</th><th>d_{Ir} (nm)</th><th>d_{IrO2} (nm)</th><th>$S_{IrO2/Ir}$ (m^2 g_{Ir}^{-1})</th><th>S_{IrO2} (m^2 g_{Ir}^{-1})</th></tr>
<tr><td>AP</td><td rowspan="2">1.7</td><td>1.7</td><td rowspan="2">156</td><td>156</td></tr>
<tr><td>150H_2 (3 h ageing)</td><td>2.2</td><td>121</td></tr>
<tr><td>150H_2 (18 h ageing)</td><td rowspan="2">2.1</td><td rowspan="2">2.7</td><td rowspan="2">127</td><td rowspan="2">98</td></tr>
<tr><td>nanocapsule</td></tr>
</table>

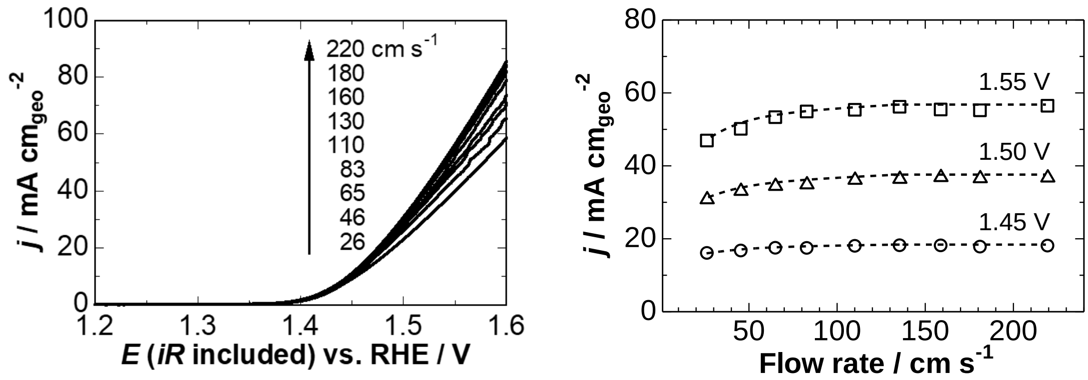

Figure 2-12. LSVs (*iR*-included) for IrO_x/Nb-SnO_2 catalyst in N_2-saturated 0.1 M $HClO_4$ solution at 80°C with regard to various flow rates from 26 to 220 cm s^{-1} with a sweep rate of 10 mV s^{-1}. The current density (j) is based on the geometric area of the Au substrate of the working electrode (4 mm^2).

Figure 2-13a shows the *iR*-free anodic polarization curves for IrO_x/Nb-SnO_2 (150H_2, 18 h ageing) and conventional catalysts (mixture of commercial IrO_2 and Pt black, 1:1 mass ratio) in air-saturated 0.1 M $HClO_4$ solution at 80 °C. The flow rate of the electrolyte solution was adjusted at 160 cm s^{-1} in order to remove oxygen gas bubbles effectively from the electrode surface. The IrO_x/Nb-SnO_2 catalyst showed onset potentials for the OER at 1.38 V, which was similar to that for the conventional catalyst. Clearly, the *MA* of the IrO_x/Nb-SnO_2 catalyst was much higher than that of the conventional catalyst. The values of apparent *MA* at 1.5 V ($MA_{1.5}$) exceeding 10 A mg_{Ir}^{-1} was 28 times larger than that of the conventional one. This indicates the possibility of reduction of the amount of noble metal anode catalyst to a low level, e.g., 0.1 mg_{Ir} cm^{-2} for operation at 1 A cm^{-2}.

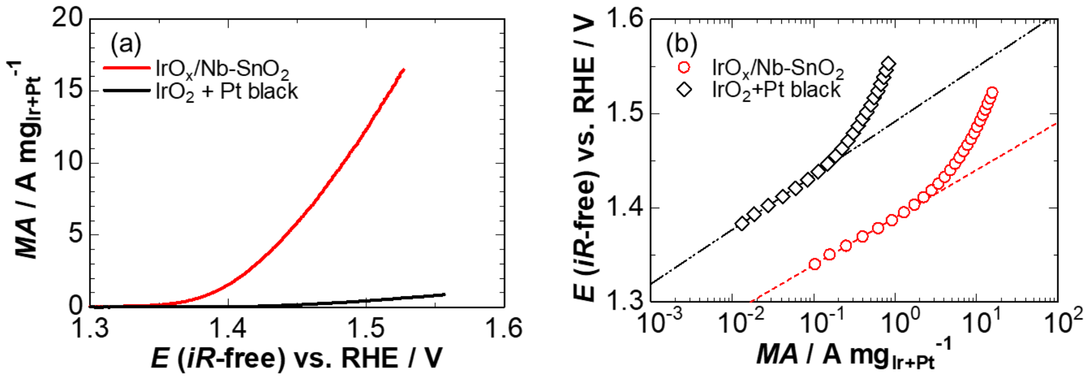

Figure 2-13. (a) *iR*-free anodic polarization curves for IrO_x/Nb-SnO_2 and conventional (IrO_2 + Pt black) catalysts in air-saturated 0.1 M $HClO_4$ solution at 80 °C with a flow rate of 160 cm s^{-1}. The current is shown as the apparent mass activity (*MA*) based on the mass of Ir (or Ir + Pt for the conventional catalyst) loaded on the electrode substrate. (b) Tafel plots for *iR*-free anodic polarization curves shown in (a). The values of Tafel slopes for IrO_x/Nb-SnO_2 and conventional catalysts at $E < 1.43$ V were 51 and 63 mV, respectively.

To ascribe the reason for such enhanced *MA*s, the specific surface areas (S_{IrO2}) for each sample was calculated at first in the same manner to **Appendix 2-2**. For the conventional catalyst, the value of S_{IrO2} was calculated to be 21 m^2 g_{IrO2}^{-1} or 24 m^2 g_{Ir}^{-1} by assuming spherical particles of commercial IrO_2 powder with 25 nm diameter based on SEM and TEM images as shown in **Figure 2-8**. Thus the increase in S_{IrO2} of the IrO_x/M-SnO_2 could be estimated by a factor of 4.0 to 5.3 compared with that of the commercial IrO_2 (see Table **2-2**). The *MA* in OER might be also affected by the structure of an IrO_x shell on an Ir core (a factor of ca. 2 at 1.5 V). However, the enhancement factor of the $MA_{1.5}$ was larger than their combination.

Another interesting factor was found in the Tafel plots as shown in **Figure 2-13b**. The Tafel slope for the conventional catalyst at E < 1.43 V was 63 mV, which is close to the 60 mV slope commonly reported for IrO_2-based electrodes in sulfuric acid solution [23–26]. In contrast, the values of Tafel slopes for IrO_x/M-SnO_2 catalysts ranged from 46 mV (IrO_x/Ta-SnO_2) to 52 mV (IrO_x/Sb-SnO_2). This suggests a promotion of the OER on the IrO_x surface due to an interaction with the doped SnO_2 supports [26–28]. It has been reported that the OER rate can be enhanced by a rapid oxidation of hydroxyl OH_{ad} species, which might adsorb on active sites of the IrO_x surface as the intermediate, into oxygen O_{ad} [29,30]. SnO_2 could catalyze such an oxidation step of OH_{ad} into O_{ad} on the IrO_x surface. Hence, the enhanced *MA*s of IrO_x/M-SnO_2 might be ascribed not only to a significant increase in the active surface area by the use of 2-nm sized IrO_x nanoparticles, but also their interaction with the oxide supports.

Lastly, the stability test of the IrO_x/Nb-SnO_2 catalyst during constant current OER was also carried out preliminary in air-saturated 0.1 M $HClO_4$ solution at 80°C. As shown in **Figure 2-14**, the potential was almost constant up to 50 hours, but the potential rose steeply after 68 h. It was observed that the catalyst layer had peeled away from the Au substrate, probably due to generated oxygen bubbles. Regarding the stability of the SnO_2 support itself, the Pourbaix diagram indicates that SnO_2 is stable in the potential and pH regions examined in the present work [19]. Moreover, dissolution of Nb and Sn from Pt/Nb-SnO_2 synthesized by the same method was not observed for the stability test in H_2SO_4 aqueous solution at 80°C under ambient air [31].

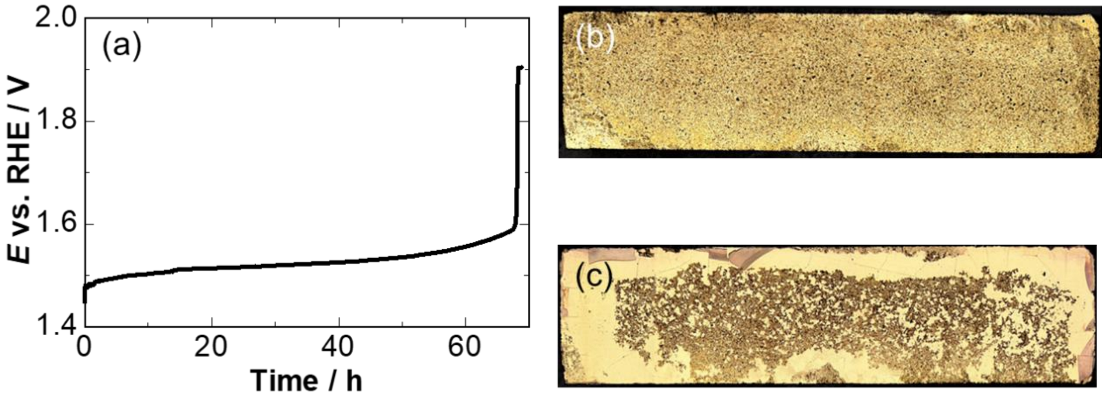

Figure 2-14. (a) Time course of potential during constant current OER at IrO_x/Nb-SnO_2 catalyst in air-saturated 0.1 M $HClO_4$ solution at 80°C and 20 mA cm_{geo}^{-1} (4 A mg_{Ir}^{-1}). The current density examined corresponds to 1 A cm^{-2} in a PEMWE with an Ir-loading of 0.25 mg_{Ir} cm^{-2}. The laser microscopic images of Au substrate (b) before and (c) after the time course test. The slope between 10 and 40 h was 0.47 mV h^{-1}.

Appendix 2-1. Calculation method for the amounts of the Nb-SnO_2 support.

The amount of Nb-SnO_2, for IrO_x/Nb-SnO_2 with 18 h ageing as an example, was calculated as follows. The amount of Ir loading was 11.3 wt%, which was quantified by ICP after dissolving the catalysts completely by the alkaline carbonate-fusion method. This value corresponds to (Ir^0 + $Ir^{(IV)}$) contained in the catalyst, and the value of $Ir^{(IV)}$ (IrO_2) percentage analyzed by XPS was 16% (at% = wt%). Then, two following equations were used for the mass of Ir^0 and $Ir^{(IV)}$:

$$m_{\mathrm{Ir}^0} + m_{\mathrm{Ir}^{(\mathrm{IV})}} = 11.3 \quad (2.1)$$

$$m_{\mathrm{Ir}^{(\mathrm{IV})}} / (m_{\mathrm{Ir}^0} + m_{\mathrm{Ir}^{(\mathrm{IV})}}) = 0.16 \quad (2.2)$$

The contents of Ir^0 and $Ir^{(IV)}$ thus obtained were 9.5 wt% and 1.8 wt%, respectively. The mass of IrO_2 [m_{IrO2}] can be calculated to be 2.1 wt% from the following equation:

$$m_{\mathrm{IrO2}} = m_{\mathrm{Ir}^{(\mathrm{IV})}} \times (192.22+32)/192.22 \quad (2.3)$$

Hence, the content of Nb-SnO_2 in the catalyst was 88.4 wt% [= 100 − (9.5 + 2.1)]. When the working electrode consisted of the IrO_x/Nb-SnO_2 catalyst was loaded on the Au substrate at a constant amount of 5 μg_{Ir} cm^{-2}, the amount of Nb-SnO_2 loaded on the Au substrate was calculated to be 39 μg cm^{-2}.

Appendix 2-2. Calculation method for specific surface area of IrO_2 (S_{IrO2}) for IrO_x nanoparticles supported on doped SnO_2 catalysts.

Here I would like to explain here how to calculate S_{IrO2} for the IrO_x particles during operation as OER catalysts. Assuming that fcc Ir particles have an ideal cubo-octahedral shape, we can calculate the number of total atoms (N_{total}) in the particle with the number of atomic layers (L) together with the number of surface atoms ($N_{surface}$), in a similar manner for the case of fcc Pt or Pt alloy particles [32,33]:

$$N_{\mathrm{total}} = \frac{10}{3}L^3 - 5L^2 + \frac{11}{3}L - 1 \qquad (2.4)$$

N_{total} for a spherical particle can be calculated with diameter d,

$$d = a\left(\frac{3N_{\mathrm{total}}}{2\pi}\right)^{\frac{1}{3}} \qquad (2.5)$$

where a is the lattice constant for Ir (fcc structure).

Next, the number of surface atoms was calculated by the following equation:

$$N_{\mathrm{surface}} = 10L^2 - 20L + 12 \qquad (2.6)$$

For the case of IrO_x/Nb-SnO_2 with d_{Ir} = 2.1 nm, the fraction of surface atoms ($N_{surface}/N_{total}$) was calculated to be 52%. A percentage of 16% of $Ir^{(IV)}$ in the particle, estimated by XPS, can be rationally explained if 31% of the surface atoms (= 16/52) were oxidized to IrO_2 in the as-prepared catalyst. If all of the surface atoms were oxidized to IrO_2 with an Ir metal core during the OER, the initial particle size of 2.1 nm would be nearly unchanged. Thus, the value of S_{IrO2} (on an Ir metal core) was 127 $m^2\ g_{Ir}^{-1}$. On the other hand, if all Ir atoms in the particle were oxidized to IrO_2 during the OER, the particle size could increase from 2.1 nm to 2.7 nm while maintaining a constant total amount of Ir atoms, resulting in a value of 98 $m^2\ g_{Ir}^{-1}$.

2.5 Conclusion

In order to reduce the amount of noble metal catalysts for the OER in PEMWE while maintaining high efficiency, I have synthesized new Ir_yPt_{100-y} binary nanoparticles prepared by the nanocapsule method at first. In 0.1 M $HClO_4$ electrolyte solution at 80°C, a convex plot of *MA*s towards OER from 20 to 35 at% of Ir content was found, besides a significant improvement of *MA*s from 35 to 100 at% was shown. However, Ir/Nb-SnO_2 catalyst which exhibited the highest *MA* towards OER, contained quite small Ir amount of 1.8 wt% loaded on the support. Therefore, next IrO_x nanocatalysts with uniform sizes of ca. 2 nm were prepared successfully by the use of the colloidal method, highly dispersed on Nb-doped SnO_2 support. The 18 h aged catalyst exhibited moderate Ir loading with high *MA*, which was exceeding 10 A mg_{Ir}^{-1} at 1.5 V and 28 times larger than the conventional one, and thus it was used in order to investigate the electrochemically experimental conditions, such as the flow-rate dependence to eliminate the effect of O_2 generation as much as possible.

References

1. K.C. Neyerlin, G. Bugosh, R. Forgie, Z. Liu, and P. Strasser, Combinatorial study of high-surface-area binary and ternary electrocatalysts for the oxygen evolution reaction. *J. Electrochem. Soc.* **156**, B363 (2009), DOI: 10.1149/1.3049820.
2. H.-Y. Jung, S. Park, and B.N. Popov, Electrochemical studies of an unsupported PtIr electrocatalyst as a bifunctional oxygen electrode in a unitized regenerative fuel cell. *J. Power Sources* **191**, 357 (2009), DOI: 10.1016/j.jpowsour.2009.02.060.
3. K.M. Papazisi, A. Siokou, S. Balomenou, and D. Tsiplakides, Preparation and characterization of $Ir_xPt_{1-x}O_2$ anode electrocatalysts for the oxygen evolution reaction. *Int. J. Hydrogen Energy*, **37**, 16642 (2012), DOI: 10.1016/j.ijhydene.2012.02.118.
4. F. Ye, W. Hu, H. Liu, J. Liu, J. Li, X. Wang, and J. Yang, Pt-IrO_2 nanorod array electrode for oxygen evolution in PEM water electrolysis cell. *Asia-Pac. J. Chem. Eng.*, **8**, 271 (2013), DOI: 10.1002/apj.1675.
5. S. Rivas, L.G. Arriaga, L. Morales, and A.M. Fernández, Evaluation of Pt-Ru-Ir as bifunctional electrocatalysts for the oxygen electrode in a unitized regenerative fuel cell. *Int. J. Electrochem. Sci.*, **7**, 3601 (2012), http://www.electrochemsci.org/papers/vol7/7043601.pdf.
6. K. Okaya, H. Yano, H. Uchida, and M. Watanabe, Control of particle size of Pt and Pt alloy electrocatalysts supported on carbon black by the nanocapsule method. *ACS Appl. Mater. Interfaces*, **2**, 888 (2010), DOI: 10.1021/am9008693.
7. Y. Ogihara, H. Yano, M. Watanabe, A. Iiyama, and H. Uchida, Effect of an Sb-doped SnO_2 support on the CO-tolerance of Pt_2Ru_3 nanocatalysts for residential fuel cells. *Catalysts*, **6**, 139 (2016), DOI: 10.3390/catal6090139.
8. Y. Chino, K. Taniguchi, Y. Senoo, K. Kakinuma, M. Hara, M. Watanabe, and M. Uchida, Effect of added graphitized CB on both performance and durability of Pt/Nb-

SnO_2 cathodes for PEFCs. *J. Electrochem. Soc.*, **162**, F736 (2015), DOI: 10.1149/2.0651507jes.

9. K. Kakinuma, M. Uchida, T. Kamino, H. Uchida, and M. Watanabe, Synthesis and electrochemical characterization of Pt catalyst supported on $Sn_{0.96}Sb_{0.04}O_{2-\delta}$ with a network structure. *Electrochim. Acta*, **56**, 2881 (2011), DOI: 10.1016/j.electacta.2010.12.077.
10. Y. Senoo, K. Kakinuma, M. Uchida, H. Uchida, S. Deki, and M. Watanabe, Improvements in electrical and electrochemical properties of Nb-doped $SnO_{2-\delta}$ supports for fuel cell cathodes due to aggregation and Pt loading. *RSC Adv.*, **4**, 32180 (2014), DOI: 10.1039/c4ra03988b.
11. M. Watanabe, M. Uchida, and S. Motoo, Preparation of highly dispersed Pt + Ru alloy clusters and the activity for the electrooxidation of methanol. *J. Electroanal. Chem.*, **229**, 395 (1987), DOI: 10.1016/0022-0728(87)85156-2.
12. N. Wakabayashi, M. Takeichi, H. Uchida, and M. Watanabe, Temperature dependence of oxygen reduction activity at Pt-Fe, Pt-Co, and Pt-Ni alloy electrodes. *J. Phys. Chem. B* **109**, 5836 (2005), DOI: 10.1021/jp04620(IV).
13. H. Yano, E. Higuchi, H. Uchida, and M. Watanabe, Temperature dependence of oxygen reduction activity at Nafion-coated bulk Pt and Pt/carbon black catalysts. *J. Phys. Chem. B* **110**, 16544 (2006), DOI: 10.1021/jp063497t.
14. H. Uchida, N. Ikeda, and M. Watanabe, Electrochemical quartz crystal microbalance study of copper adatoms on gold electrodes Part II. Further discussion on the specific adsorption of anions from solutions of perchloric and sulfuric acid. *J. Electroanal. Chem.*, **424**, 5 (1997), DOI: 10.1016/S0022-0728(96)04924-8.
15. S.A. Grigoriev, P. Millet, and V.N. Fateev, Evaluation of carbon-supported Pt and Pd nanoparticles for the hydrogen evolution reaction in PEM water electrolysers. *J.*

Power Sources **177**, 281 (2008), DOI: 10.1016/j.jpowsour.2007.11.072.

16. F. Marangio, M. Santarelli, and M. Calì, Theoretical model and experimental analysis of a high pressure PEM water electrolyser for hydrogen production. *J. Hydrogen Energy* **34**, 1143 (2009), DOI: 10.1016/j.ijhydene.2008.11.083.
17. K.A. Lewinski, D. Vliet, and S.M. Luopa, NSTF advances for PEM electrolysis - the effect of alloying on activity of NSTF electrolyzer catalysts and performance of NSTF based PEM electrolyzers. *ECS Trans.*, **69** (17), 893 (2015), DOI: 10.1149/06917.0893ecst.
18. M. Rubel, R. Haasch, P. Mrozek, A. Wieckowski, C. De Pauli, and S. Trasatti, Characterization of IrO_2-SnO_2 thin layers by electron and ion spectroscopies. *Vacuum*, **45**, 423 (1994), DOI: 10.1016/0042-207X(94)90314-X.
19. M. Pourbaix, *Atlas of Electrochemical Equilibria in Aqueous Solutions*, 2nd ed.; National association of corrosion engineers (1974), ISBN: 0915567989.
20. Y.-T. Kim, P.P. Lopes, S.-A. Park, A-Y. Lee, J. Lim, H. Lee, S. Back, Y. Jung, N. Danilovic, V. Stamenkovic, J. Erlebacher, J. Snyder, and N.M. Markovic, Balancing activity, stability and conductivity of nanoporous core-shell iridium/iridium oxide oxygen evolution catalysts. *Nature Commun.*, **8**, *1449*, 1 (2017), DOI: 10.1038/s41467-017-01734-7.
21. V.A. Saveleva, L. Wang, D. Teschner, T. Jones, A.S. Gago, K.A. Friedrich, S. Zafeiratos, R. Schlögl, and E.R. Savinova, Operando evidence for a universal oxygen evolution mechanism on thermal and electrochemical iridium oxides. *J. Phys. Chem. Lett.*, **9**, 3154 (2018), DOI: 10.1021/acs.jpclett.8b00810.
22. Y. Chino, K. Kakinuma, D.A. Tryk, M. Watanabe, and M. Uchida, Influence of Pt loading and cell potential on the HF ohmic resistance of an Nb-doped SnO_2-supported Pt cathode for PEFCs. *J. Electrochem. Soc.*, **163**, F97 (2016), DOI:

10.1149/2.0571602jes.

23. J.-M. Hu, J.-Q. Zhang, and C.-N. Cao, Oxygen evolution reaction on IrO_2-based DSA type electrodes: kinetics analysis of Tafel lines and EIS. *J. Hydrogen Energy* **29**, 791 (2004), DOI: 10.1016/j.ijhydene.2003.09.007.
24. A.T. Marshall and R.G. Haverkamp, Electrocatalytic activity of IrO_2–RuO_2 supported on Sb-doped SnO_2 nanoparticles. *Electrochim. Acta* **55**, 1978 (2010), DOI: 10.1016/j.electacta.2009.11.018.
25. H.S. Oh, H.N. Nong, T. Reier, M. Gliech, and P. Strasser, Oxide-supported Ir nanodendrites with high activity and durability for the oxygen evolution reaction in acid PEM water electrolyzers. *Chem. Sci.* **6**, 3321 (2015), DOI: 10.1039/c5sc00518c.
26. G. Liu, J. Xu, Y. Wang, and W. Wang, An oxygen evolution catalyst on an antimony doped tin oxide nanowire structured support for proton exchange membrane liquid water electrolysis. *J. Mater. Chem. A* **3**, 20791 (2015), DOI: 10.1039/C5TA02942B.
27. J. Xu, G. Liu, J. Li, and X. Wang, The electrocatalytic properties of an IrO_2/SnO_2 catalyst using SnO_2 as a support and an assisting reagent for the oxygen evolution reaction. *Electrochim. Acta* **59**, 105 (2012), DOI: 10.1016/j.electacta.2011.10.044.
28. H.-S. Oh, H.N. Nong, T. Reier, A. Bergmann, M. Gliech, J.F. Araújo, E. Willinger, R. Schlögl, D. Teschner, and P. Strasser, Electrochemical catalyst−support effects and their stabilizing role for IrO_x nanoparticle catalysts during the oxygen evolution reaction. *J. Am. Chem. Soc.* **138**, 12552 (2016) DOI: 10.1021/jacs.6b07199.
29. J. Rossmeisl, Z.-W. Qu, H. Zhu, G.-J. Kroes, and J.K. Nørskov, Electrolysis of water on oxide surfaces. *J. Electroanal. Chem.* **607**, 83 (2007), DOI: 10.1016/j.jelechem.2006.11.008
30. S. Ferro, D. Rosestolato, C.A. Martínez-Huitle, and A.D. Battisti, On the oxygen evolution reaction at IrO_2-SnO_2 mixed-oxide electrodes. *Electrochim. Acta* **146**, 257

(2014), DOI: 10.1016/j.electacta.2014.08.110.

31. K. Kakinuma, Y. Chino, Y. Senoo, M. Uchida, T. Kamino, H. Uchida, S. Deki, and M. Watanabe, Characterization of Pt catalysts on Nb-doped and Sb-doped $SnO_{2-\delta}$ support materials with aggregated structure by rotating disk electrode and fuel cell measurements, *Electrochim. Acta* **110** 316 (2013), DOI: 10.1016/j.electacta.2013.06.127

32. R.E. Benfield, Mean coordination numbers and the non-metal transition in clusters. *J. Chem. Soc. Faraday Trans.* **88**, 1107 (1992), DOI: 10.1039/FT9928801107.

33. K. Okaya, H. Yano, K. Kakinuma, M. Watanabe, and H. Uchida, Temperature dependence of oxygen reduction reaction activity at stabilized Pt skin-PtCo alloy/graphitized carbon black catalysts prepared by a modified nanocapsule method. *ACS Appl. Mater. Interfaces* **4**, 6982 (2012), DOI: 10.1021/am302224n.

Chapter 3: Improvement of Performances for Practical PEMWE Cells with Iridium Oxide/Doped Tin Oxide Catalysts

3.1 Introduction

To utilize the unique advantages of tin oxide supports with fused-aggregate network structures, it was succeeded to disperse IrO_x nanoparticles as novel anode catalysts for PEMWE onto such Nb-SnO_2 supports in ***Chapter2***. In addition, it was reported that Ta-SnO_2 and Sb-SnO_2 supports exhibited higher electrical conductivity than the Nb-SnO_2 support [1,2]. As stated in section **1.4**, the high conductivity of supports was needed for the high OER performances. However to my knowledge, there are no literature to investigate the effect of electrical conductivity on OER performances in terms of comparison with the catalytic activity in electrolyte solution and practical cells. Here, the polarization properties in a series of IrO_x/M-SnO_2 (M = Nb, Ta, and Sb) catalysts with different values of the apparent conductivities ($\sigma_{app, catalyst}$) were examined for the OER at 80 °C in both 0.1 M $HClO_4$ solution (half cell) and a MEA (a single cell) by the use of a Nafion® membrane (thickness = 50 μm) as a practical PEMWE cell. For the first time, I found that the cell potential (E_{cell}) of the single cell decreased with the increasing values of $\sigma_{app, catalyst}$, whereas they exhibited similar OER activities in the half cell test.

3.2 Experimental Methods: Electrochemical Measurements in Practical PEMWE Cells (Single Cells)

IrO_x/Ta-SnO_2 and IrO_x/Sb-SnO_2 catalysts were prepared in the similar manner to IrO_x/Nb-SnO_2 catalyst as described in section **2.2** (i.e. 150H_2 with 18 h ageing catalysts). The projected compositions were set to be $Sn_{0.975}Ta_{0.025}O_{2-\delta}$ and $Sn_{0.95}Sb_{0.05}O_{2-\delta}$ referred from literature [1,2]. The apparent electrical conductivities of the M-SnO_2 supports and IrO_x/M-SnO_2 catalysts were measured by the two-probe method described in a previous paper [3].

Catalyst coated membranes (CCMs) were prepared as follows. First, the anode catalyst ink was prepared by mixing the IrO_x/M-SnO_2 powder, water, ethanol, and Nafion® binder solution (DE521, Du Pont Co.) as the ionomer in a ball-mill for 30 min. The cathode catalyst ink was prepared from commercial Pt/GCB (Pt 50 wt%, TEC10EA50E, Tanaka Kikinzoku Kogyo, Tokyo, Japan). The volume ratio of ionomer to the support (I/S) was adjusted to 0.7 (dry basis) in each ink. Then, the catalyst inks were directly sprayed onto the Nafion® membrane (thickness 50 μm, NRE 212, Du Pont Co., Tokyo, Japan) by the pulse-swirl-spray technique (Nordson Co., Tokyo, Japan) to prepare the CCM with an active geometric area of 25 cm^2. The CCMs were hot-pressed at 140 °C and 2.5 MPa for 3 min. The Ir loading amount for the anode catalyst layer (CL) was 0.11 mg_{Ir} cm^{-2}, and the Pt loading amount for the cathode CL was 0.35 ± 0.02 mg_{Pt} cm^{-2}. As a reference, a conventional anode catalyst (mixture of IrO_2 and Pt black, 1:1 mass ratio) with 2.66 mg_{Ir+Pt} cm^{-2} and a Pt black cathode catalyst with 2.01 mg_{Pt} cm^{-2} were employed. The CCM was sandwiched by two GDLs; a Pt-plated Ti mesh (Bekaert Toko Metal Fiber Co., Ltd., Ibaraki, Japan) for the anode, and a carbon fiber paper with microporous layer (25BC, SGL Carbon Group Co., Ltd., Tokyo, Japan) for the cathode. The MEA thus prepared was mounted into a single cell holder (Japan Automobile

Research Institute standard cell) with ribbed single serpentine flow channels.

Pure water was circulated at a flow rate of 40 mL min^{-1} for the anode. Hydrogen gas was purged to the cathode. Current-potential (*I*–*E*) curves were measured galvanostatically at 80 °C under steady-state conditions. The ohmic resistance of the cell was measured by a digital AC milliohmmeter (Model 3566, Tsuruga Electric, Co.) at 1 kHz during the operation.

The thickness of the anode CL was observed after preparation of a cross-sectional sample of the CCM by a scanning ion microscope (SIM) in a focused ion beam system (FIB; FB-2200, Hitachi High-Technologies Co., Ltd.).

3.3 Results and Discussion: OER Performances of IrO_x/M-SnO_2 (M = Nb, Ta, and Sb) Catalysts

3.3.1 Physical Properties of IrO_x/M-SnO_2 Catalysts

Figure 3-1 shows TEM images of IrO_x/M-SnO_2 catalysts with fused-aggregate network structures. The values of average size (d_{Ir}) and standard deviations for the IrO_x nanoparticles were 2.0 ± 0.3, 2.2 ± 0.3, and 2.0 ± 0.4 nm in the IrO_x/Nb-SnO_2, IrO_x/Ta-SnO_2, and IrO_x/Sb-SnO_2 catalysts, respectively. It was also characterized that these catalysts by BET surface area of the M-SnO_2 supports (S_{SnO2}), the iridium loadings estimated by ICP, the percentage of $Ir^{(IV)}$ (IrO_2) in IrO_x evaluated by XPS, the amounts of M-SnO_2 supports (see **Appendix 2-1** for calculation method), the apparent electrical conductivities of the M-SnO_2 supports ($\sigma_{app,\ support}$) and IrO_x-dispersed catalysts ($\sigma_{app,\ catalyst}$). These results are summarized in **Table 3-1**. While Sb-SnO_2 exhibited a somewhat larger S_{SnO2} value, similar amounts of iridium metal were loaded with similar percentages of $Ir^{(IV)}$ on all three catalysts. Marked differences are seen between $\sigma_{app,\ support}$ and $\sigma_{app,\ catalyst}$ values for each catalyst. The Sb-SnO_2 support exhibited the highest $\sigma_{app,\ support}$ among the supports examined, i.e., three orders of magnitude higher than that of Nb-SnO_2. The $\sigma_{app,\ support}$ values of all doped-SnO_2 increased by ca. two orders of magnitude by dispersing IrO_x on their surface. In particular, the $\sigma_{app,\ catalyst}$ value of the IrO_x/Sb-SnO_2 catalyst was the highest, 8.1×10^{-1} S cm^{-1}. Such a large increase in the σ_{app} was very similar to that observed by loading Pt nanoparticles on doped SnO_2 supports [3], where Pt nanoparticles could contribute to shrink the depletion layer of SnO_2. A similar mechanism can be envisioned for the case of the IrO_x nanoparticles on SnO_2. Thus,

$IrO_x/M\text{-}SnO_2$ catalysts were successfully synthesized with similar microstructures but with a range of different of $\sigma_{app,\ catalyst}$ values.

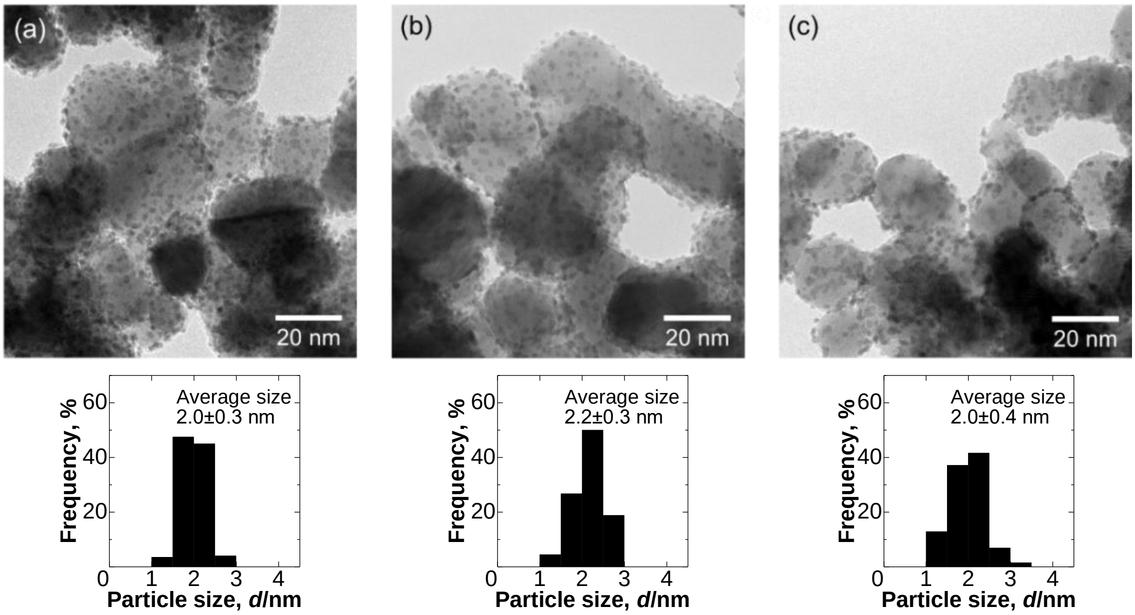

Figure 3-1. TEM images and particle size (d_{Ir}) distribution histograms for (a) $IrO_x/Nb\text{-}SnO_2$, (b) $IrO_x/Ta\text{-}SnO_2$, and (c) $IrO_x/Sb\text{-}SnO_2$ catalysts. Note that the values of d_{Ir} for the $IrO_x/Nb\text{-}SnO_2$ catalyst was changed slightly from 2.1 (in ***Chapter 2***) to 2.0 nm because of new preparation in ***Chapter 3***.

Table 3-1. BET surface area for the supports (S_{SnO2}), Ir loadings, IrO_2 percentages (corresponding to $Ir^{(IV)}$ vs. total Ir) in IrO_x nanoparticles, M-SnO_2 loadings, and apparent electrical conductivities of M-SnO_2 supports ($\sigma_{app, support}$) and IrO_x/M-SnO_2 catalysts ($\sigma_{app, catalyst}$).

Sample	S_{SnO2} (m^2 g^{-1})	Ir (Ir^0 + $Ir^{(IV)}$) loading (wt%)	$Ir^{(IV)}$ (IrO_2) percentage (%)	M-SnO_2 loading (wt%)	$\sigma_{app, support}$ (S cm^{-1})	$\sigma_{app, catalyst}$ (S cm^{-1})
IrO_x/Nb-SnO_2	30	11.3	16	88.4	2.5×10^{-5}	1.5×10^{-3}
IrO_x/Ta-SnO_2	25	10.4	19	89.3	1.3×10^{-4}	2.9×10^{-2}
IrO_x/Sb-SnO_2	40	11.0	21	88.6	1.8×10^{-2}	8.1×10^{-1}
commercial IrO_2	–	–	100	–	6.4×10^{1} [4]	

3.3.2 Oxygen Evolution Activities of IrO_x/M-SnO_2 Catalysts in Half Cells

Figure 3-3 shows the *iR*-free anodic polarization curves for IrO_x/M-SnO_2 and conventional catalysts in air-saturated 0.1 M $HClO_4$ solution at 80 °C, in which the current is shown as the *MA*. These IrO_x/M-SnO_2 catalysts showed onset potentials for the OER from 1.35 to 1.40 V, which was similar to that for the conventional catalyst. The *MA*s of the IrO_x/M-SnO_2 catalysts were also similar, which values at 1.5 V for IrO_x/Ta-SnO_2 and IrO_x/Sb-SnO_2 were 36 and 27 times larger, respectively, than that of the conventional one.

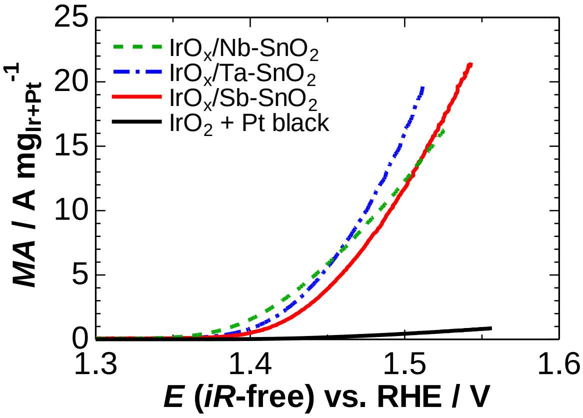

Figure 3-3. *iR*-free anodic polarization curves for IrO_x/M-SnO_2 and conventional (IrO_2 + Pt black) catalysts in air-saturated 0.1 M $HClO_4$ solution at 80 °C with a flow rate of 160 cm s^{-1}. The current is shown as the apparent mass activity (*MA*) based on the mass of Ir (or Ir + Pt for the conventional catalyst) loaded on the electrode substrate.

3.3.3 Oxygen Evolution Activities of IrO_x/M-SnO_2 Catalysts in Single Cells

CCMs were prepared with low noble metal loadings by the use of the IrO_x/M-SnO_2 catalysts with 0.11 mg_{Ir} cm^{-2} at the anode and a commercial Pt/GCB (Pt supported on graphitized carbon black) with 0.35 ± 0.02 mg_{Pt} cm^{-2} at the cathode. A conventional anode catalyst (IrO_2 + Pt black, described above) with 2.66 mg_{Ir+Pt} cm^{-2} and a Pt black cathode catalyst with 2.01 mg_{Pt} cm^{-2} were employed in a reference CCM. The *I*–*E* curves of single cells operated at 80 °C are shown in **Figure 3-4**.

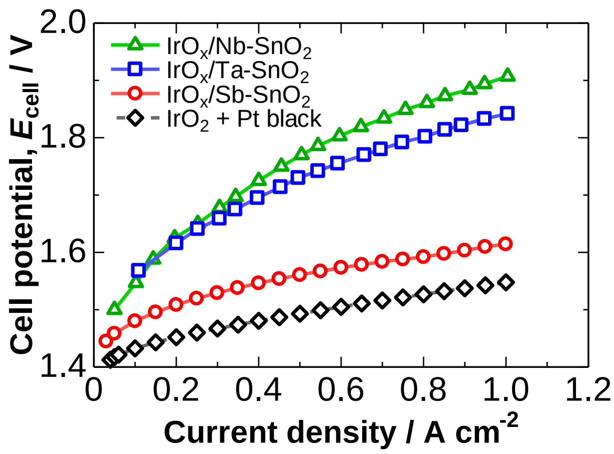

Figure 3-4. Steady-state *I*–*E* curves of single cells with various anodes and Pt/GCB cathode at 80 °C. Ultrapure water was supplied to the anode with a flow rate of 40 mL min^{-1}. The cathode compartment was purged with H_2.

The performances of the cells with three kinds of IrO_x/M-SnO_2 anodes were found to be enhanced in the order: IrO_x/Nb-SnO_2 < IrO_x/Ta-SnO_2 << IrO_x/Sb-SnO_2. For example, as shown in **Table 3-3**, the E_{cell} at 1 A cm^{-2} decreased from 1.91 V for IrO_x/Nb-SnO_2 cell to 1.61 V for the IrO_x/Sb-SnO_2 cell. The latter value was somewhat larger than that of the reference (conventional) cell (1.55 V). It is noteworthy that the initial cathode performance of Pt supported on high-surface-area carbon (Pt/C) was comparable to that of Pt black, even though Pt black has still been predominantly used in practical PEMWEs in order to ensure a long lifetime of the MEA [5]. In order to mitigate the corrosion of the carbon support, Pt supported on GCB was used in place of high-surface-area carbon. In any case, the increase in the overvoltage of IrO_x/M-SnO_2 cells compared with that of the conventional cell can be ascribed predominantly to the anode catalyst with reduced amount of noble metal (< 1/20). As shown in **Figure 3-5**, the values of *MA* based on mass of Ir for the IrO_x/Sb-SnO_2 catalyst at E_{cell} >1.45 V were considerably larger than that of the conventional cell. Interestingly, the E_{cell} of 1.61 V for the IrO_x/Sb-SnO_2 cell corresponds to a voltage efficiency (ε_v) of 92%, which is the highest performance at the significantly low Ir loading of 0.11 mg_{Ir} cm^{-2} at the anode reported so far [6,7].

Table 3-3. Noble metal loadings on CCMs, ohmic resistances ($R_{ohm, cell, obs}$) and cell potentials (E_{cell}) at 1 A cm^{-2} for various cells.

Anode catalyst	Anode loading (mg_{Ir+Pt} cm^{-2})	Cathode loading (mg_{Pt} cm^{-2})	$R_{ohm, cell, obs}$ (mΩ cm^2)	E_{cell} @1 A cm^{-2} (V)
IrO_x/Nb-SnO_2	0.11	0.34	258	1.91
IrO_x/Ta-SnO_2	0.11	0.37	175	1.84
IrO_x/Sb-SnO_2	0.11	0.35	97	1.61
IrO_2+Pt black	2.66	2.01	75	1.55

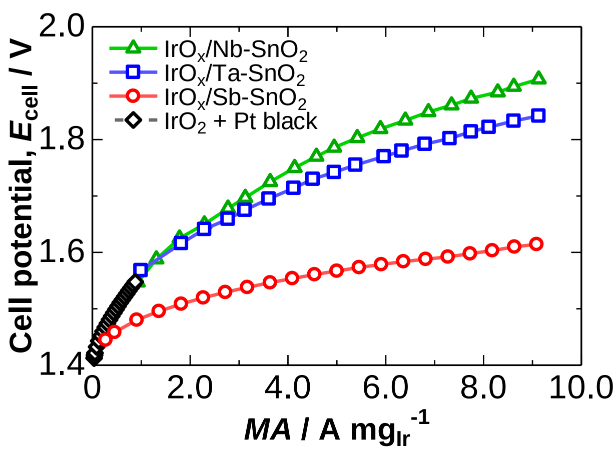

Figure 3-5. Steady-state *I*–*E* curves of single cells with various anodes and Pt/GCB cathode at 80 °C. The current is shown as the apparent mass activity (*MA*) based on the mass of Ir loaded in the anode catalyst layers. Pure water was supplied to the anode with a flow rate of 40 mL min^{-1}. The cathode compartment was purged with H_2.

Next, it is discussed the essential parameters necessary to improve the anode performance. Referring to the properties of IrO_x/M-SnO_2 catalysts in **Table 3-1**, the only marked differences are seen for the values of $\sigma_{app,\ catalyst}$ (or $\sigma_{app,\ support}$). The ohmic resistances of the cells ($R_{ohm,\ cell,\ obs}$) measured at 1 kHz during the operation are shown in **Table 3-3**; the $R_{ohm,\ cell,\ obs}$ values ranged from 75 to 258 mΩ cm^2.

To start, values of $R_{ohm,\ cell,\ calc}$ for comparison with the observed values were calculated. First, it was estimated that $R_{ohm,\ anode}$ of the anode CLs as follows. The thickness of the IrO_x/Sb-SnO_2 CL was ca. 10 μm, observed by SIM as shown in **Figure 3-6**. Since I have prepared all CLs in the same manner, it was assumed the identical thickness for the IrO_x/Ta-SnO_2 and IrO_x/Nb-SnO_2 CLs. Assuming the porosity of the CLs to be 50%, their R_{ohm} values were calculated based on their $\sigma_{app,\ catalyst}$ values. The values of $R_{ohm,\ anode}$ thus calculated for IrO_x/Sb-SnO_2, IrO_x/Ta-SnO_2, and IrO_x/Nb-SnO_2 were 3, 68, and 1333 mΩ cm^2, respectively. Second, for the Nafion® electrolyte membrane with the thickness of 50 μm, it was adopted the $R_{ohm,\ Nafion}$ to be 50 mΩ cm^2. The $R_{ohm,\ cell}$ of the conventional cell in **Table 3-3** was just 75 mΩ cm^2, which is assumed to include $R_{ohm,\ anode}$ (IrO_2 + Pt black) and $R_{ohm,\ cathode}$ (Pt black), together with contact resistances with the GDLs (Pt/Ti mesh and carbon paper). This value of $R_{ohm,\ cell}$ agrees precisely with those of PEFCs with Nafion® membrane of the identical thickness and Pt/C catalysts for the anode and cathode [8–10]. Thus, by adding the $R_{ohm,\ anode}$ of IrO_x/M-SnO_2 to 75 mΩ cm^2 stated above, it was calculated the $R_{ohm,\ cell,\ calc}$ values to be 78, 143, and 1408 mΩ cm^2, for the cells with IrO_x/Sb-SnO_2, IrO_x/Ta-SnO_2, and IrO_x/Nb-SnO_2, respectively. The former two values are relatively consistent with those of $R_{ohm,\ cell,\ obs}$. However, a large discrepancy is seen between $R_{ohm,\ cell,\ obs}$ and $R_{ohm,\ cell,\ calc}$ for IrO_x/Nb-SnO_2. One of the possible reasons is that $\sigma_{app,\ catalyst}$ was measured in ambient air (low humidity) at room temperature, while $R_{ohm,\ cell,\ obs}$ was measured during operation with the anode in pure water at 80 °C. It has been shown that the electronic conductivities of SnO_2-based materials increase with humidity [11,12]. Water molecules adsorbed on the SnO_2 surface can act as electron donors, resulting in an increase in the carrier concentration near the surface. Such a tendency was shown to be more marked for SnO_2 samples with lower electronic conductivity [11,12]. Thus, it can be easily understood that the value of $R_{ohm, cell, obs}$ of IrO_x/Nb-SnO_2 (in pure water at 80 °C) could be much smaller than that of $R_{ohm, cell, calc}$. Taking into account such an effect of water on the electronic conductivity of the M-SnO_2, it is appropriate to employ $R_{ohm, cell, obs}$ as a measure of the apparent resistance of the anode catalyst layer, rather than $R_{ohm, cell, calc}$ based on $\sigma_{app, catalyst}$ (measured in air).

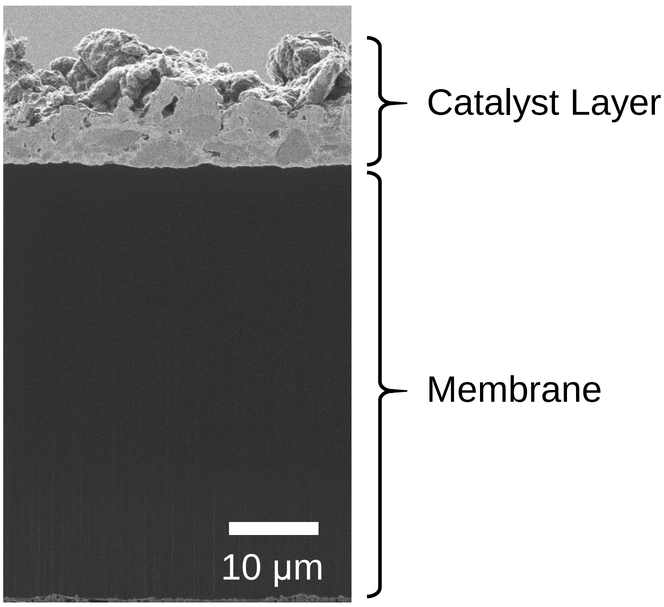

Figure 3-6. Scanning ion microscopic (SIM) image of the cross-section at the anode for the CCM with IrO_x/Sb-SnO_2 catalyst. The average thickness and the standard deviation of the catalyst layer was 9.6 ± 3.1 μm.

It is clearly seen in **Figure 3-4** and **Table 3-3** that E_{cell} decreased with decreasing $R_{ohm, cell, obs}$. However, this is not simply due to the reduction of the ohmic (*iR*) loss. For example, the reduction of the *iR* loss at 1 A cm^{-2} is only ca. 0.08 V by replacing the IrO_x/Ta-SnO_2 anode catalyst with IrO_x/Sb-SnO_2, but the reduction of the E_{cell} in such a case was as large as 0.23 V. On the other hand, the OER activities (*MA* values or Tafel slopes) of the three IrO_x/M-SnO_2 catalysts measured in 0.1 M $HClO_4$ solution in the previous section can be regarded as being at a similar level.

This interesting phenomenon can be reasonably explained as follows. As illustrated in **Figure 3-7**, for the measurement of the OER activities in 0.1 M $HClO_4$ electrolyte solution in the channel flow cell (half cell), IrO_x/M-SnO_2 CLs were dispersed uniformly on the Au substrate with the thickness corresponding to a ca. two-monolayer height of M-SnO_2 support particles (~ 60 nm), intending that all catalyst particles can be in contact with the electrolyte solution. Therefore, it is expected that all of the IrO_x nanocatalyst particles are able to function without any influence of the small electronic (ohmic) resistances of such thin CLs. In contrast, for the measurement of single cell (MEA) performance, the thickness of the anode CL was 10 μm (170 times thicker than that in the half cell). Consequently, electrons generated at the IrO_x nanoparticles in the OER must be transported in the CL to the current collector (Pt/Ti), even though protons can be effectively supplied to the IrO_x surface through the electrolyte binder (ionomer) network. Hence, the higher the $\sigma_{app, catalyst}$ value (lower $R_{ohm, cell, obs}$) is, the lower the OER overvoltage will be in the single cell, due to an effective utilization of the IrO_x nanocatalyst particles on the M-SnO_2 support.

As is clear from **Fig. 3-7** (b), other essential factors are the transport rates of protons and oxygen in the ionomer coated on the catalyst, in addition to the O_2 gas diffusion rate in the CL. Similar to the case of PEFC CLs [13], it is very important to control the microstructure of the CLs, i.e., thickness of the ionomer (related to I/S), primary and secondary pore volumes, etc. While an effect of I/S on the performance of IrO_2/TiO_2 anode has been reported recently [14], more comprehensive research is necessary to optimize the single cell performance toward the near-ideal value evaluated in the half cell, together with high durability.

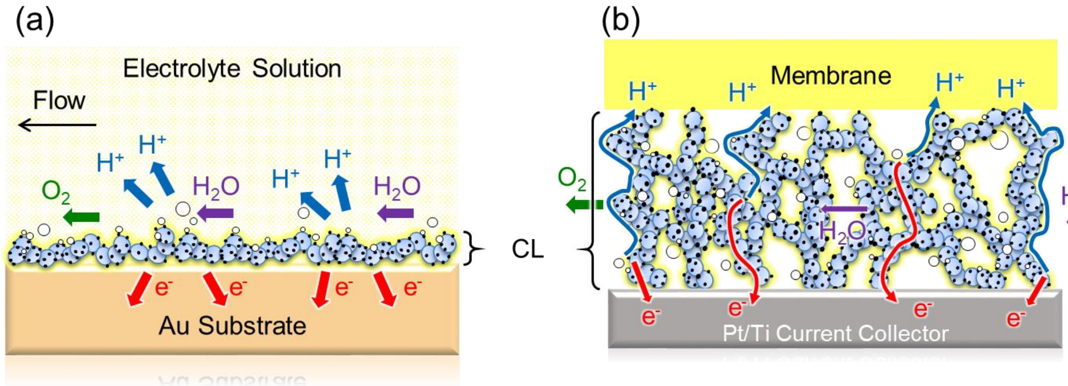

Figure 3-7. Schematic images of the IrO_x/M-SnO_2 anode catalyst layer (CL) during the OER in (a) electrolyte solution (half cell) and (b) a single cell.

3.4 Conclusion

The polarization performances of the $IrO_x/M\text{-}SnO_2$ (M= Nb, Ta, Sb) anode catalysts with fused-aggregate network structures were examined for the OER in both a half cell (0.1 M $HClO_4$) and a single cell with a Nafion® membrane at 80°C. These catalysts exhibited similar high values of *MA* for the OER, regardless of the values of $\sigma_{app, catalyst}$ in the half cell, whereas the E_{cell} decreased with decreasing $R_{ohm, cell, obs, catalyst}$ in the single cell tests. In addition to the reduction of the *iR* loss, the predominant reduction of the anodic overvoltage is ascribed to the increased effective utilization of IrO_x nanocatalyst particles supported on $M\text{-}SnO_2$ with higher $\sigma_{app, catalyst}$. Specifically, a single cell exhibited a promising performance E_{cell} = 1.61 V (ε_V of 92%) at 1 A cm^{-2} and 80°C with the use of an $IrO_x/Sb\text{-}SnO_2$ anode (0.11 mg_{Ir} cm^{-2}) and Pt/GCB cathode (with 0.35 mg_{Pt} cm^{-2}).

References

1. K. Kakinuma, M. Uchida, T. Kamino, H. Uchida, and M. Watanabe, Synthesis and electrochemical characterization of Pt catalyst supported on $Sn_{0.96}Sb_{0.04}O_{2-\delta}$ with a network structure. *Electrochim. Acta* **56**, 2881 (2011), DOI: 10.1016/j.electacta.2010.12.077.
2. Y. Senoo, K. Taniguchi, K. Kakinuma, M. Uchida, H. Uchida, S. Deki, and M. Watanabe, Cathodic performance and high potential durability of Ta-$SnO_{2-\delta}$–supported Pt catalysts for PEFC cathodes. *Electrochem. Commun.* **51**, 37 (2015), DOI: 10.1016/j.elecom.2014.12.005.
3. Y. Senoo, K. Kakinuma, M. Uchida, H. Uchida, S. Deki, and M. Watanabe, Improvements in electrical and electrochemical properties of Nb-doped $SnO_{2-\delta}$ supports for fuel cell cathodes due to aggregation and Pt loading. *RSC Adv.* **4**, 32180 (2014), DOI: 10.1039/c4ra03988b.
4. P. Mazúr, J. Polonský, M. Paidar, and K. Bouzek, Non-conductive TiO_2 as the anode catalyst support for PEM water electrolysis. *Int. J. Hydrogen Energy* **37**, 12081 (2012), DOI: 10.1016/j.ijhydene.2012.05.129.
5. M. Carmo, D.L. Fritz, J. Mergel, and D. Stolten, A comprehensive review on PEM water electrolysis. *Int. J. Hydrogen Energy* **38**, 4901 (2013), DOI: 10.1016/j.ijhydene.2013.01.151.
6. K.A. Lewinski, D.F. Vliet, and S.M. Luopa, NSTF advances for PEM electrolysis—The effect of alloying on activity of NSTF electrolyzer catalysts and performance of NSTF based PEM electrolyzers. *ECS Trans.* **69**, 893 (2015), DOI: 10.1149/06917.0893ecst.
7. S.M. Alia, B. Rasimick, C. Ngo, K.C. Neyerlin, S.S. Kocha, S. Pylypenko, H. Xu, and B.S. Pivovar, Activity and durability of iridium nanoparticles in the oxygen

evolution reaction. *J. Electrochem. Soc.* **163**, F3105 (2016), DOI: 10.1149/2.0151611jes.

8. T. Omata, M. Uchida, H. Uchida, M. Watanabe, and K. Miyatake, Effect of platinum loading on fuel cell cathode performance using hydrocarbon ionomers as binders. *Phys. Chem. Chem. Phys.* **14**, 16713 (2012), DOI: 10.1039/c2cp42997g.
9. Y.-C. Park, K. Kakinuma, M. Uchida, D.A. Tryk, T. Kamino, H. Uchida, and M. Watanabe, Investigation of the corrosion of carbon supports in polymer electrolyte fuel cells using simulated start-up/shutdown cycling. *Electrochim. Acta* **91**, 195 (2013), DOI: 10.1016/j.electacta.2012.12.082.
10. Y. Yamashita, S. Itami, J. Takano, M. Kodama, K. Kakinuma, M. Hara, M. Watanabe, and M. Uchida, Durability of Pt catalysts supported on graphitized carbon-black during gas-exchange start-up operation similar to that used for fuel cell vehicles. *J. Electrochem. Soc.* **163**, F644 (2016), DOI: 10.1149/2.0771607jes.
11. G. Korotchenkov, V. Brynzari, and S. Dmitriev, Electrical behavior of SnO_2 thin films in humid atmosphere. *Sens. Actuators B* **54**, 197 (1999), DOI: 10.1016/S0925-4005(99)00016-7.
12. N. Barsan and U. Weimar, Conduction model of metal oxide gas sensors. *J. Electroceramics* **7**, 143 (2001), DOI: 10.1023/A:1014405811371.
13. M. Lee, M. Uchida, H. Yano, D.A. Tryk, H. Uchida, and M. Watanabe, New evaluation method for the effectiveness of platinum/carbon electrocatalysts under operating conditions. *Electrochim. Acta* **55**, 8504 (2010) DOI: 10.1016/j.electacta.2010.07.071.
14. M. Bernt and H.A. Gasteiger, Influence of ionomer content in IrO_2/TiO_2 electrodes on PEM water electrolyzer performance. *J. Electrochem. Soc.* **163**, F3179 (2016), DOI: 10.1149/2.0231611jes.

Chapter 4: A Challenge toward High Stability for Practical PEMWE Cells with Low Catalyst Loading

4.1 Introduction

A single cell with the use of an IrO_x/Sb-SnO_2 anode (0.11 mg_{Ir} cm^{-2}) and Pt/GCB cathode (with 0.35 mg_{Pt} cm^{-2}) exhibited a promising performance E_{cell} = 1.61 V (ε_V of 92%) at 1 A cm^{-2} and 80 °C in ***Chapter 3***. Thus the durability test for the IrO_x/Sb-SnO_2 cell at a constant current density of 1 A cm^{-2} was carried out, however the degradation rate was high (33 mV h^{-1}, see **Figure 4-1**). To investigate the reason, the catalyst powder was picked from the ink preparation for MEAs by drying. Then I have confirmed that IrO_x nanoparticles were migrated onto and detached partially from the surface of Sb-SnO_2 supports observed by TEM as shown in **Figure 4-2** (c). I have considered this might be ascribed that the interaction between iridium and tin oxide was too weak to support under strong acidic media. To improve the interaction, the condition of pre-treatment under inert gas condition was investigated in ***Chapter 4***.

There are some papers to investigate the effect of heat treatments on OER activities for mixed thin films of iridium oxides with oxides of tin, titanium and/or manganese [1–4]. They concluded that improved OER activities would be affected by their surface interactions due to the formation of the solid solution including IrO_2, while it has been also reported that OER activities were decreased in the case of iridium based nanoparticles supported on Sb-SnO_2 [5,6]. It was considered that declined OER activities were attributed from the change of chemical states on the surfaces and/or the loss of surface areas due to the coarsening of particles annealed at high temperature (> 500°C).

It has been mentioned that IrO_2 will be dissolved into SnO_2 slightly at 320°C under O_2 atmosphere, followed by the formation of (Ir,Sn)O_2 solid solution [7]. However the effect of $(Ir,Sn)O_2$ solid solution on the OER activity, especially for nanoparticles, has not been measured as far. I have found that IrO_x/Sb-SnO_2 catalyst formed the solid solution at the temperature between 300 to 400°C under N_2 atmosphere. Thus I have challenged to investigate the annealing effect on the OER activity, as well as the durability.

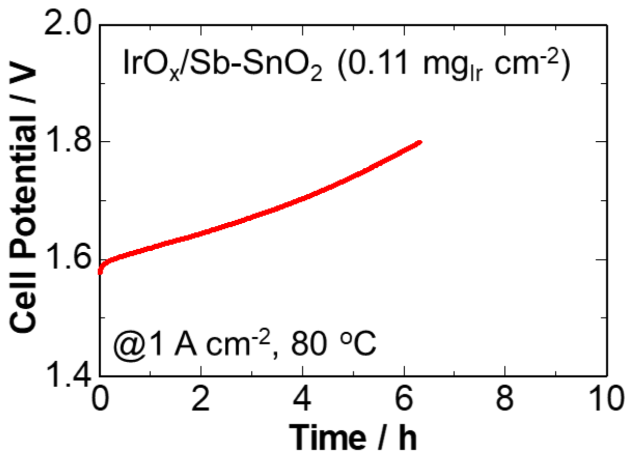

Figure 4-1. Time course of potential applying a constant current of 1 A cm^{-1} for IrO_x/Sb-SnO_2 ($150H_2$) catalyst cell at 80°C. Pure water was supplied to the anode with a flow rate of 40 mL min^{-1}.

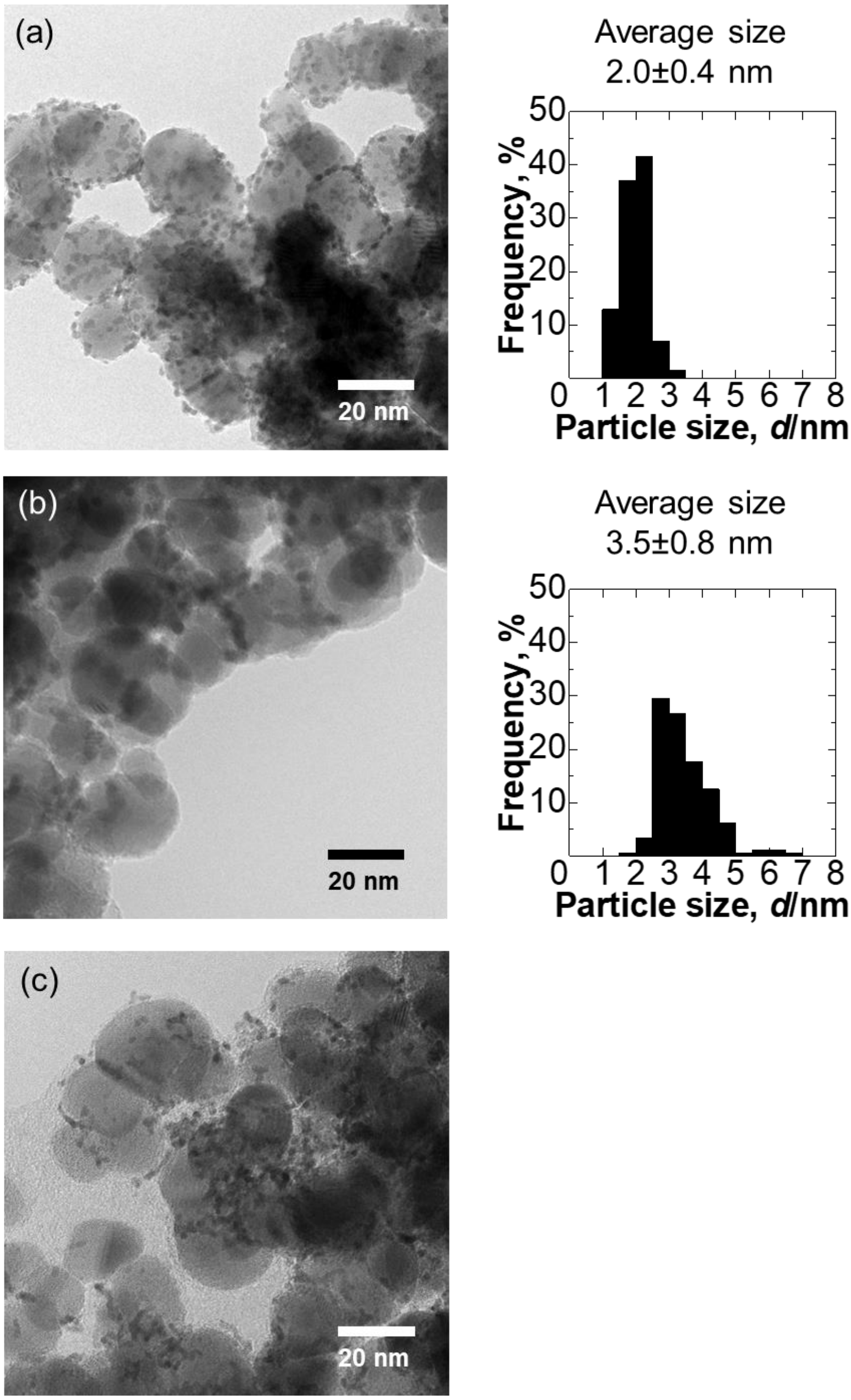

Figure 4-2. TEM images and particle size distribution histograms of IrO_x/Sb-SnO_2 (150H_2) catalyst; (a) as synthesized, (b) after the galvanostatic measurement, (c) after ink preparation (before any tests, see the method in section **3.2.2**).

4.2 Evaluation Techniques of the Formation of Solid Solution

The IrO_x/Sb-SnO_2 (AP) samples were heat-treated at the temperature of *t* (from 250 to 400) °C for 2 h under N_2 atmosphere before H_2 treatment at 150°C. These samples were used as a series of the catalysts in the ink preparation and OER activity tests. The annealed samples were denoted as *t*N150H_2 catalysts hereinafter.

In-situ TEM (H-9500, Hitachi High-Technologies Co., an acceleration voltage of 200 kV and an emission current < 0.2 μA) technique at the temperature from 250 to 400°C with introducing N_2 or H_2 gas under a pressure of 0.1 Pa was applied by the use of a direct-heating holder.

The content of Ir^0, $Ir^{(IV)}$, and $Sn^{(IV)}$ in the IrO_x/Sb-SnO_2 were characterized by XPS equipped with an infrared heating furnace. The samples could be annealed by this furnace at the temperature of *t*°C under N_2 atmosphere (*t*N samples) followed by H_2 treatment (*t*N150H_2 samples), subsequently XPS measurement by the transportation without air exposure. Sn^0 was not detected for all samples.

4.3 Results and Discussion: Annealing Effects on Physical Properties

Figure 4-3 shows ex-situ TEM images and particle size distributions of a series in *t*N150H_2 catalysts (t = 0, 300, 350, and 400°C). IrO_x nanoparticles of 1 to 3 nm in diameter were found to be dispersed uniformly on the oxide supports. The particle size (d_{Ir}) and the standard deviations of the IrO_x nanoparticles were 2.0 ± 0.4, 2.1 ± 0.4, 2.1 ± 0.6, and 1.6 ± 0.4 nm for the 150H_2, 300N150H_2, 350N150H_2, and 400N150H_2 catalysts, respectively. The value of d_{Ir} for 400N150H_2 was somewhat smaller than the others, while a significant increase in d_{Ir} was not observed for each sample.

The chemical states of Ir and Sn as a function of temperature was shown in **Figure 4-4**. For *t*N samples, the increase in $Ir^{(IV)}$ ratio to total amount of Ir (corresponding to Ir^0 + $Ir^{(IV)}$) was observed up to 350N, moreover $Ir^{(IV)}$/Sn ratio was slightly increased. Here, a hypothesis of the formation of $(Ir,Sn)O_2$ solid solution at such temperature via the oxidation from Ir^0 to $Ir^{(IV)}$ is built up. Note that the reduction of $Sn^{(IV)}$ was probably very small because IrO_x/Sb-SnO_2 involved only 11.0 wt% of Ir^0, and the transition amount of Ir^0 to $Ir^{(IV)}$ was only 17% in case of *t*N series. In contrast, the $Ir^{(IV)}$ ratio to total amount of Ir at 400N was declined, which might be affected by the reduction to Ir metals. It has been reported that $(Ir,Sn)O_2$ solid solution would be decomposed at 450°C [7]. The ratio of total amount of Ir to Sn was decreased, which suggests the Ir atoms were diffused into SnO_2 supports beyond the detection limits of XPS, based on the hypothesis. While the values after H_2 treatment in *t*N150H_2 series were decreased compared to those at N_2 heat treatment mainly due to the reduction of IrO_2, tendencies described above were still confirmed; suggesting that the $(Ir,Sn)O_2$ solid solution has been remained in the interface between IrO_x nanoparticles and $Sb\text{-}SnO_2$ support.

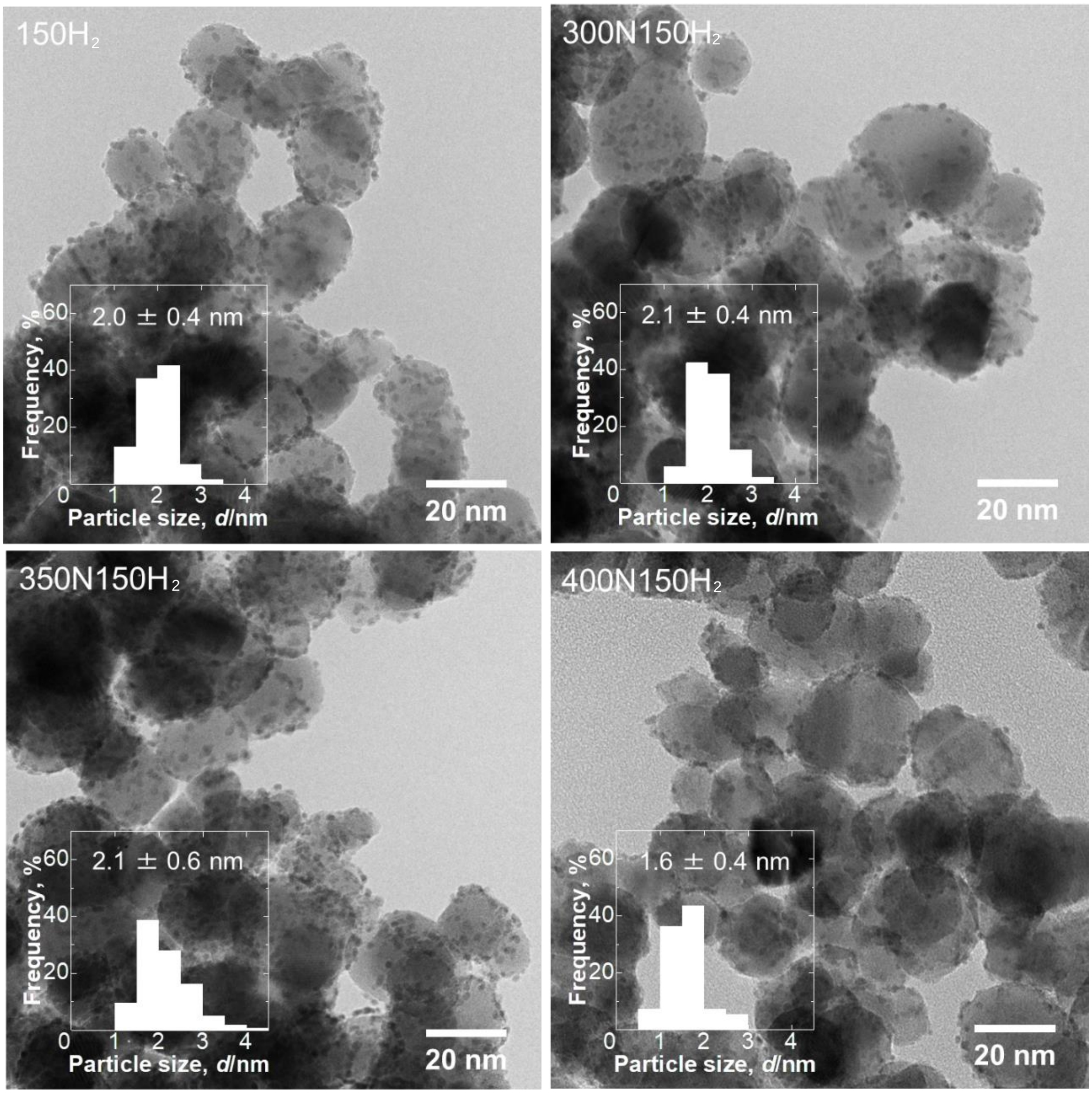

Figure 4-3. TEM images and particle size distribution histograms in a series of *t*$N150H_2$ catalysts with ex-situ heat treatments.

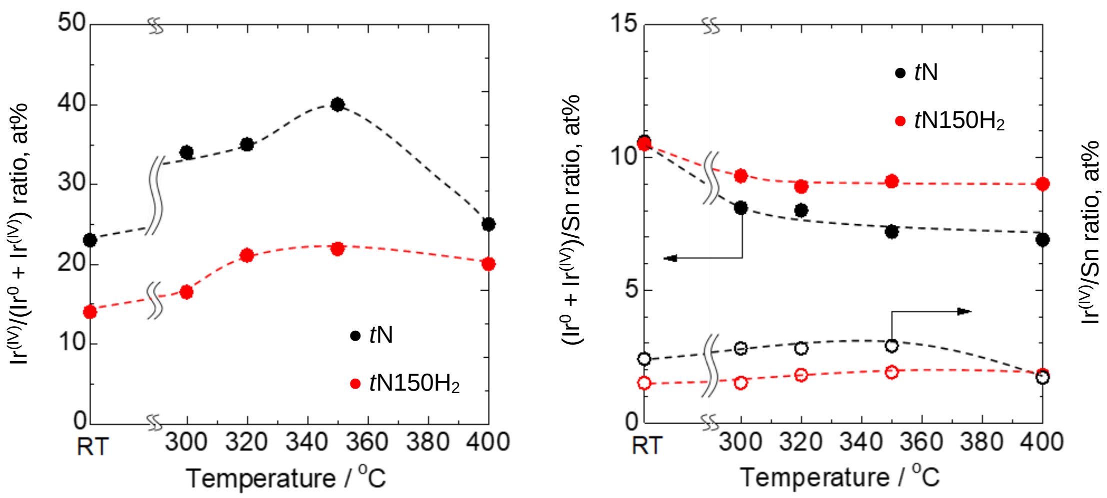

Figure 4-4. The ratio of $Ir^{(IV)}$ to total amount of Ir [$Ir^{(IV)}/(Ir^0 + Ir^{(IV)})$], total amount of Ir to Sn [$(Ir^0 + Ir^{(IV)})/Sn$], and $Ir^{(IV)}$ to Sn ($Ir^{(IV)}/Sn$) in a series of *t*N and *t*N150H$_2$ powders estimated by XPS. All samples were annealed without air exposure.

To verify the hypothesis, a series of in-situ environmental TEM images was carried out at the temperature from 250 to 350°C with N_2 gas introducing, and at the temperature up to 100°C under H_2 atmosphere as shown in **Figure 4-5**. It was observed that the diameter of IrO_x nanoparticles were smaller with increasing temperature, suggesting Ir atoms diffused into Sb-SnO_2 supports partially at the introducing N_2 gas. Therefore, it was clarified that the heat treatment from 300 to 350°C in inert gas leads to the formation of interfacial solid solution partially. In contrast, the nanoparticles appeared on the surface of Sb-SnO_2 supports at the temperature ≥ 80°C under H_2 atmosphere.

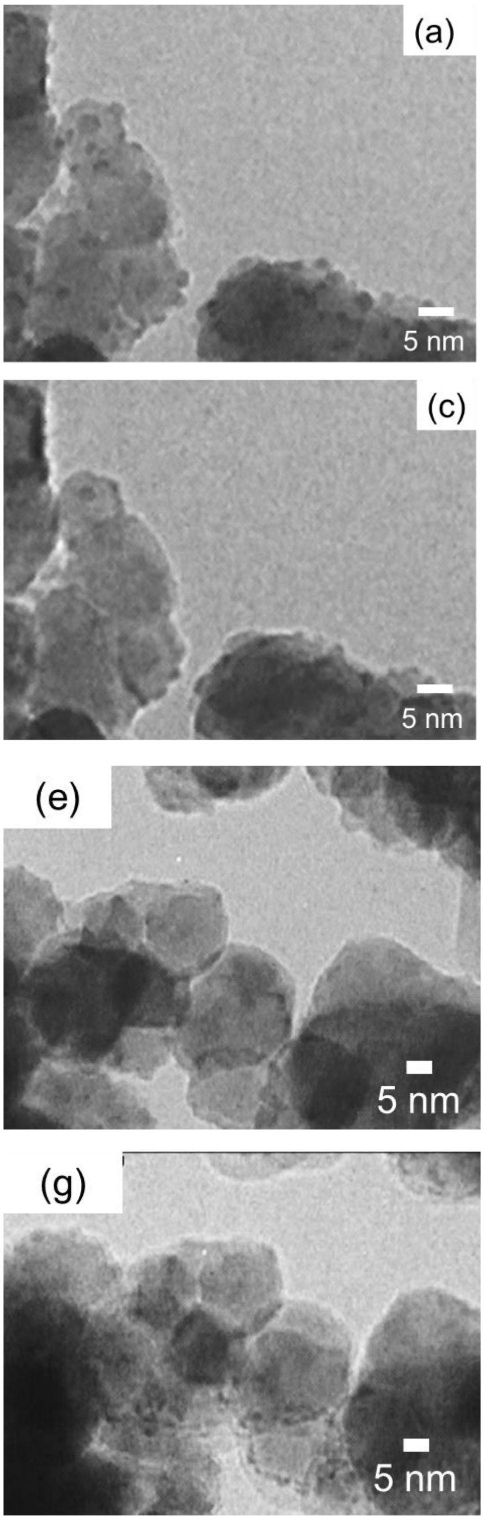

Figure 4-5. In-situ environmental TEM images of IrO_x/Sb-SnO_2; (a) pristine (= AP), (b) 250, (c) 300, and (d) 350°C under N_2 atmosphere. (e) RT (= 350N), (f) 60, (g) 80, and (h) 100°C with introducing H_2 gas.

4.4 Results and Discussion: Effects of the Partially Interfacial Solid Solution on Oxygen Evolution Activities and Fixation of IrO_x Nanoparticles

The relationship between $Ir^{(IV)}$ ratio to the total amount of Ir [$Ir^{(IV)}/(Ir^0 + Ir^{(IV)})$] and OER activities in 0.1 M $HClO_4$ at 80°C (represents the value of $MA_{1.5}$) is shown in **Figure 4-6**. Interestingly, the values of $MA_{1.5}$ were enhanced with increasing in the value of $Ir^{(IV)}/(Ir^0 + Ir^{(IV)})$, mainly due to the interaction between the IrO_x nanoparticles and Sb-SnO_2. Especially 350N150H_2 catalyst exhibited $MA_{1.5}$ of 23 A mg_{Ir}^{-1}, which was twice higher than 150H_2. This indicates the possibility of further reduction of the Ir amount at an anode catalyst to a level as low as 0.05 mg_{Ir} cm^{-2} at 1 A cm^{-2} or the operation at high current density of 2 A cm^{-2} with the same Ir amount as the 150H_2 cell (0.1 mg_{Ir} cm^{-2}). While it is necessary to find the key factor(s) for such an enhancement (e.g., the surface and/or internal Ir states of IrO_x nanoparticles, the interface information between IrO_x and Sb-SnO_2), I have probed that the (Ir,Sn)O_2 solid solution is one of promising approaches to improve OER activities even in the field of nanoparticle catalysts.

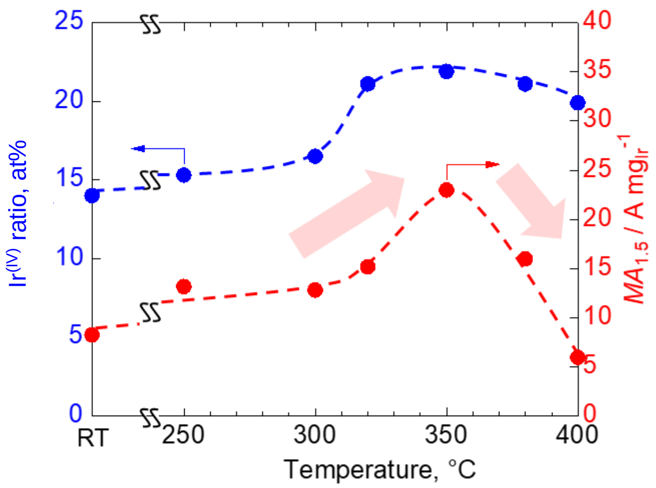

Figure 4-6. The relationship between $Ir^{(IV)}/(Ir^0 + Ir^{(IV)})$ and $MA_{1.5}$ as a function of N_2 annealing temperature for a series of *t*N150H_2 catalysts.

In addition, the $(Ir,Sn)O_2$ solid solution may affect to the fixation of IrO_x nanoparticles onto the supports. **Figure 4-7** shows TEM images after the ink preparation for $150H_2$ and $350N150H_2$. As stated in section **4.1**, many isolated agglomerates of IrO_x nanoparticles on or among Sb-SnO_2 supports were observed for $150H_2$. On the other hand, it was found that IrO_x nanoparticles were maintained to be dispersed on the supports for $350N150H_2$. This fixation effect will lead to improve the durability of IrO_x nanoparticles. Durability testing of a single cell with $350N150H_2$ anode catalyst is going to be carried out in near future.

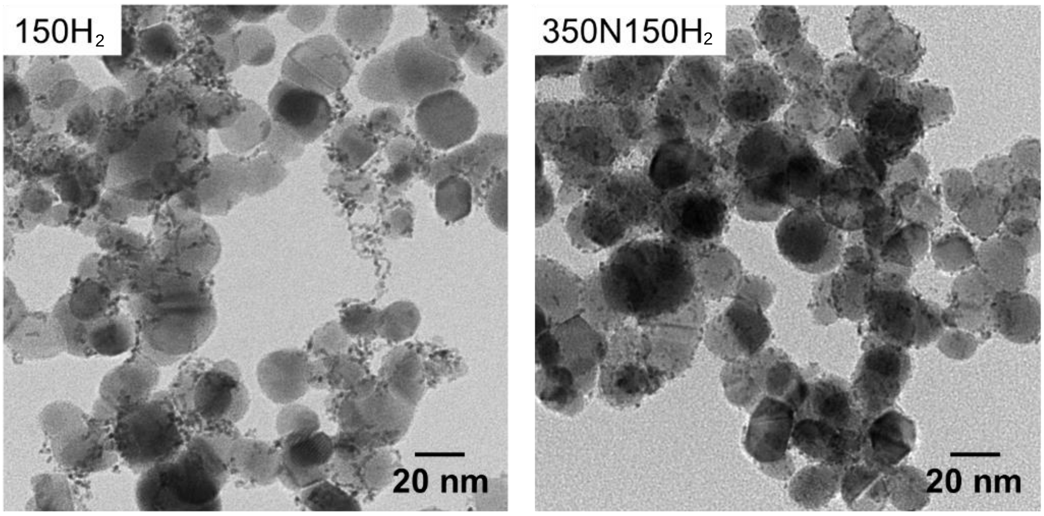

Figure 4-7. TEM images of IrO_x/Sb-SnO_2 ($150H_2$ and $350N150H_2$) catalysts after ink preparation.

4.5 Conclusion

It was clarified that the partially interfacial $(Ir,Sn)O_2$ solid solution could be formed by the anneal of IrO_x/Sb-SnO_2 catalyst under N_2 atmosphere at the temperature from 300 to 350°C before H_2 treatment without coarsening of nanoparticles. This solid solution helps to improve the OER activity and fix the IrO_x nanoparticles possibly due to the strengthened interaction between IrO_x nanoparticles and Sb-SnO_2 supports. According to the results of in-situ environmental TEM observation and XPS without air exposure, it was suggested that the solid solution was ascribed from the diffusion of Ir atoms into the SnO_2 support materials as illustrated in **Figure 4-8**. It is possible that the decline in active surface areas (sites) would be occurred by N_2 annealing, however, the IrO_x nanoparticles were appeared due to the partial reduction of IrO_2 near the surface of particles with moderate H_2 treatments while maintaining the effects from the interfacial solid solution.

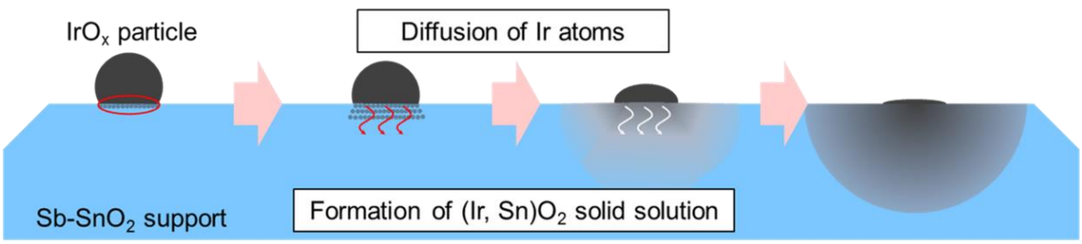

Figure 4-8. The schematic image for the formation of the partially interfacial $(Ir,Sn)O_2$ solid solution.

References

1. X. Chen, G. Chen, and P.L. Yue, Stable Ti/IrO_x-Sb_2O_5-SnO_2 anode for O_2 evolution with low Ir content. *J. Phys. Chem. B* **105**, 4623 (2001), DOI: 10.1021/jp010038d.
2. S.D. Ghadge, P.P. Patel, M.K. Datta, O.I. Velikolhatnyi, R. Kuruba, P.M. Shanthi, and P.N. Kumta, Fluorine substituted (Mn,Ir)O_2:F high performance solid solution oxygen evolution reaction electro-catalysts for PEM water electrolysis. *RSC Adv.* **7**, 17311 (2017), DOI: 10.1039/c6ra27354h.
3. S.D. Ghadge, P.P. Patel, M.K. Datta, O.I. Velikolhatnyi, P.M. Shanthi, and P.N. Kumta, First report of vertically aligned (Sn,Ir)O2:F solid solution nanotubes: Highly efficient and robust oxygen evolution electrocatalysts for proton exchange membrane based water electrolysis. *J. Power Sources* **392**, 139 (2018), DOI: 10.1016/j.jpowsour.2018.04.065.
4. D. Bernsmeier, M. Bernicke, R. Schmack, R. Sachse, B. Paul, A. Bergmann, P. Strasser, E. Ortel, and R. Kraehnert, Oxygen evolution catalysts based on Ir–Ti mixed oxides with templated mesopore structure: Impact of Ir on activity and conductivity. *ChemSusChem* **11**, 2367 (2018), DOI: 10.1002/cssc.201800932.
5. H.N. Nong, H.-S. Oh, T. Reier, E. Willinger, M.-G. Willinger, V. Petkov, D. Teschner, and P. Strasser, Oxide-supported $IrNiO_x$ core–shell particles as efficient, cost-effective, and stable catalysts for electrochemical water splitting. *Angew. Chem.* **127**, 3018 (2015), DOI: 10.1002/ange.201411072.
6. F. Karimi, A. Bazylak, and B.A. Peppley, Effect of calcination temperature on the morphological and electrochemical characteristics of supported iridium hydroxyoxide electrocatalysts for the PEM electrolyzer anode. *J. Electrochem. Soc.* **164**, F464 (2017), DOI: 10.1149/2.0111706jes.
7. X. Wang, Q. Yin, Z. Tang, X. Liu, D. Tang, and W. Lin, The nature of phase

separation in Ir–Sn–O ternary oxide electrocatalyst. *J. Eur. Ceram. Soc.* **33**, 3045 (2013), DOI: 10.1016/j.jeurceramsoc.2013.07.002.

Chapter 5: General Conclusions and Perspectives

5.1 General Conclusions

In this dissertation, it has been taken into account for issues that are the amount used and the costs of noble metal electrocatalysts, especially iridium, in PEMWE. My specific objective have been set to reduce the amount of noble metal to 1/10 compared to conventional cells with maintaining a voltage efficiency (ε_v) of 90% at 1 A cm^{-2}. Iridium based OER catalysts supported on doped tin oxides with a fused-aggregate network structure have been reported consistently in all chapters toward high performances for a practical PEMWE cell.

In ***Chapter 2***, two iridium based catalysts were newly synthesized supported on niobium doped tin oxides. One of them was Ir-Pt binary catalysts prepared by a nanocapsule method in anticipation of alloying effect. Indeed the convex plot of mass activity at 1.5 V ($MA_{1.5}$) as a function of Ir content was obtained at $Ir_{35}Pt_{65}$/Nb-SnO_2 catalyst, whereas Ir/Nb-SnO_2 catalyst with a quite low Ir loading (1.8 wt%, projected value was 20 wt%) exhibited the highest value of $MA_{1.5}$. To improve the loading, a colloidal method in an aqueous phase was used, then finally 2 nm-sized IrO_x nanoparticles highly dispersed on Nb-SnO_2 supports with an Ir loading of 11.3 wt% was succeeded to synthesize.

In ***Chapter 3***, IrO_x/M-SnO_2 (M = Nb, Ta, and Sb) catalysts with similar microstructures but with different values of the apparent conductivity (σ_{app}) were synthesized, taking into account for the investigation in the effect of σ_{app} on the cell performances. In a half-cell (electrolyte solution), similarly enhanced $MA_{1.5}$ values exceeding 10 A mg_{Ir}^{-1} for all IrO_x/M-SnO_2 catalysts were observed, which were > 20 times higher than that of conventional catalyst. This was ascribed not only to the increase in the specific surface areas (S_{IrO2}), but also the structure of an IrO_x shell on an Ir core, as well as the interaction between IrO_x nanoparticles and the doped SnO_2 supports. However the performances of the single cells (MEA) were found to be enhanced in the order: IrO_x/Nb-SnO_2 < IrO_x/Ta-SnO_2 << IrO_x/Sb-SnO_2. The predominant reduction of the cell potential (E_{cell}) is ascribed to the increased effective utilization of IrO_x nanocatalyst particles supported on M-SnO_2 with higher σ_{app}. In particular, a single cell with IrO_x/Sb-SnO_2 anode catalyst exhibited E_{cell} = 1.61 V (ε_V of 92%) at 1 A cm^{-2} with < 1/10 noble metal loading to the conventional cell, which is the highest performance reported so far as shown in **Figure 5-1**.

In ***Chapter 4***, to fix the IrO_x nanoparticles on the Sb-SnO_2 support, the interfacial $(Ir,Sn)O_2$ solid solution was investigated. By annealing at the temperature from 300 to 350°C, it has been confirmed that the partially interfacial $(Ir,Sn)O_2$ solid solution could be formed. This solid solution helped to not only fix the IrO_x nanoparticles, but also improve the OER activity. Such enhancement by the use of IrO_x nanoparticles is the first report in the Ir and Sn system.

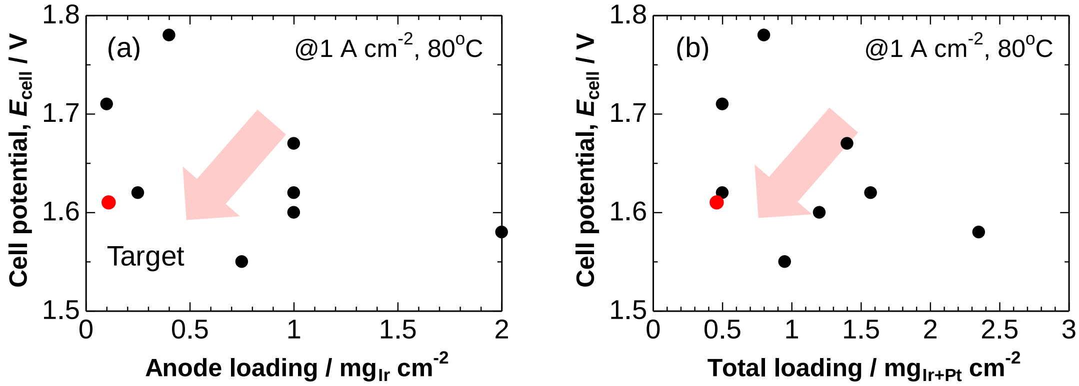

Figure 5-1. The relationships between E_{cell} and noble metal loading; (a) anode Ir loading, (b) total noble metal loading, operated at 1 A cm^{-2}, 80°C.

The symbol of ● corresponds to the present work. The values of the other E_{cell} and noble metal loadings were cited from [1-7].

5.2 Perspectives

On the stage in synthesis of catalysts, one of important results in this work is regards with the effect of σ_{app} on the OER performances. The higher σ_{app}, the higher performance was in the single cell test, which contributes the effective utilization of IrO_x nanocatalyst in OER (electrons). Here, the effectiveness at 1.5 V ($Ef_{Ir,1.5}$) that is a worthy index to evaluate its utilization under actual OER operating conditions, was evaluated as follows [8];

$$Ef_{\mathrm{Ir},1.5}\ (\%) = \frac{MA_{\mathrm{cell},1.5}}{MA_{1.5}} \times 100 \qquad (5.1)$$

where $MA_{cell,1.5}$ could be estimated in MEAs, which was calculated from **Figure 3-5**, while $MA_{1.5}$ was evaluated in electrolyte solution that quotes from **Figure 3-3**. The values of $Ef_{Ir,1.5}$ for IrO_x/Sb-SnO_2 (150H_2) anodes and conventional catalysts were 13 and 57%, respectively. One of the key reasons for this difference is ascribed to the σ_{app} (see **Table 3-1**). Therefore, the further improvement of σ_{app} will lead to the development of practical PEMWE cells.

The improvement of Ir loading will lead to increase the σ_{app}. Unfortunately, the values of Ir loading in IrO_x/M-SnO_2 materials were small (ca. 10 wt%, which is still half of the projected value). Assuming the IrO_x nanoparticles are spherical, the interparticle distances (X) can be calculated from the diameter of nanoparticles (d_{Ir}), the specific surface areas of supports (S_{SnO2}), and Ir loading (y), by the use of following equation [9].

$$X = \sqrt{\pi \rho {d_{\mathrm{Ir}}}^3 \mathrm{S}_{\mathrm{SnO2}} (100 - y)/3\sqrt{3}y} \qquad (5.2)$$

where ρ is the density of iridium. Note that the value of X represents the average distance between the centers of particles. For IrO_x/Sb-SnO_2 (150H_2) as an example, X was estimated to be 5.9 nm when d_{Ir} = 2 nm, S_{SnO2} = 40 m^2 g^{-1}, and y = 11.0 wt%. When y is 20 wt% as a projected value, X is estimated to be only 4.2 nm. This value is too small to disperse 2 nm-sized IrO_x nanoparticles on the support with high Ir loading. To overcome this drawback, one of effective approaches is the enlargement of the diameter in nanoparticles. If the value of X is set to 5.9 nm, the Ir loading will increase up to 30 or 50 wt% when d_{Ir} = 3 or 4 nm, respectively. High Ir loading in the catalyst has an excellent advantage that the thickness of catalyst layer in the practical cell would be smaller in case of the preparation of CCM with same Ir loading on the membranes. This approach also has possibilities for other benefits, to elucidate the structure of IrO_x nanoparticles, as well as to acquire information in the surfaces/interface on IrO_x nanoparticles and M-SnO_2 supports, e.g., to unravel the mechanism in formation of $(Ir,Sn)O_2$ interfacial solid solution.

The other significant finding is that IrO_x/M-SnO_2 catalysts themselves showed the high *MA*. To improve *MA* will give a benefit of the further reduction in Ir amount, and/or possibility of the operation at high current density. For instance, Ir-Ru based binary catalysts with high *MA*s are promising candidates as described in section **1.3**. Moreover, it has been reported that $(Ir,Ru)O_2$ solid solution could form a stable solid solution with a wide composition range and showed higher OER activity than IrO_2 and RuO_2 [10,11].

As one of the clues to develop an anode CL in a MEA, it is necessary to investigate an effect of I/S on the OER performances as stated in section **3.5**. As the other address, additives to an anode CL is also practicable to improve MA_{cell}. It has been reported that the cell performance consisted of IrO_2 and TiO_2 particles with submicrometer order sizes was closed to that of non-supported IrO_2, which exhibited sufficiently high σ_{app} [12]. Unsupported carbon materials (e.g., graphitized carbon black, carbon nanotube), Pt nano- or micro-particles seem to be also candidates for conductive additives, which have a possibility of good O_2 gas diffusion or transportation of electrons in anode CL without OER inhibition on IrO_x nanoparticles.

The results of Ir and IrO_x nanoparticles dispersed on M-SnO_2 supports in the present work are useful for future researches to develop the anodes of PEMWE from fundamental to practical studies, where the number of papers published has been increasing and increasing [13]. They will open up a means to solve the problem in costs and amount used for precious metal electrocatalysts, especially iridium based nanocatalysts. I believe that this dissertation provides new guideposts and special insights playing a role for drastic evolution of PEMWE.

References

1. J. Xu, G. Liu, J. Li, and X. Wang, The electrocatalytic properties of an IrO_2/SnO_2 catalyst using SnO_2 as a support and an assisting reagent for the oxygen evolution reaction. *Electrochim. Acta* **59**, 105 (2012), DOI: 10.1016/j.electacta.2011.10.044.
2. G. Li, H. Yu, X. Wang, S. Sun, Y. Li, Z. Shao, and B. Yi, Highly effective $Ir_xSn_{1-x}O_2$ electrocatalysts for oxygen evolution reaction in the solid polymer electrolyte water electrolyser. *Phys. Chem. Chem. Phys.* **15**, 2858 (2013), DOI: 10.1039/c2cp44496h.
3. H.S. Oh, H.N. Nong, T. Reier, M. Gliech, and P. Strasser, Oxide-supported Ir nanodendrites with high activity and durability for the oxygen evolution reaction in acid PEM water electrolyzers. *Chem. Sci.* **6**, 3321 (2015), DOI: 10.1039/c5sc00518c.
4. G. Liu, J. Xu, Y. Wang, and W. Wang, An oxygen evolution catalyst on an antimony doped tin oxide nanowire structured support for proton exchange membrane liquid water electrolysis. *J. Mater. Chem. A* **3**, 20791 (2015), DOI: 10.1039/C5TA02942B.
5. K.A. Lewinski, D.F. Vliet, and S.M. Luopa, NSTF advances for PEM electrolysis—The effect of alloying on activity of NSTF electrolyzer catalysts and performance of NSTF based PEM electrolyzers. *ECS Trans.* **69**, 893 (2015), DOI: 10.1149/06917.0893ecst.
6. S.M. Alia, B. Rasimick, C. Ngo, K.C. Neyerlin, S.S. Kocha, S. Pylypenko, H. Xu, and B.S. Pivovar, Activity and durability of iridium nanoparticles in the oxygen evolution reaction. *J. Electrochem. Soc.* **163**, F3105 (2016), DOI: 10.1149/2.0151611jes.
7. M. Bernt and H.A. Gasteiger, Influence of ionomer content in IrO_2/TiO_2 electrodes on PEM water electrolyzer performance. *J. Electrochem. Soc.* **163**, F3179 (2016), DOI: 10.1149/2.0231611jes.
8. M. Lee, M. Uchida, H. Yano, D.A. Tryk, H. Uchida, and M. Watanabe, New

evaluation method for the effectiveness of platinum/carbon electrocatalysts under operating conditions. *Electrochim. Acta* **55**, 8504 (2010), DOI: 10.1016/j.electacta.2010.07.071.

9. M. Watanabe, H. Sei, and P. Stonehart, The influence of platinum crystallite size on the electroreduction of oxygen. *J. Electrochem. Soc.* **261**, 375 (1989), DOI: 10.1016/0022-0728(89)85006-5.
10. S. Song, H. Zhang, X. Ma, Z. Shao, R.T. Baker, and B. Yi, Electrochemical investigation of electrocatalysts for the oxygen evolution reaction in PEM water electrolyzers. *Int. J. Hydrogen Energy* **33**, 4955 (2008), DOI: 10.1016/j.ijhydene.2008.06.039.
11. T. Audichon, T.W. Napporn, C. Canaff, C. Morais, C. Comminges, and K.B. Kokoh, IrO_2 coated on RuO_2 as efficient and stable electroactive nanocatalysts for electrochemical water splitting. *J. Phys. Chem. C* **120**, 2562 (2016), DOI: 10.1021/acs.jpcc.5b11868.
12. P. Mazúr, J. Polonský, M. Paidar, and K. Bouzek, Non-conductive TiO_2 as the anode catalyst support for PEM water electrolysis. *Int. J. Hydrogen Energy* **37**, 12081 (2012), DOI: 10.1016/j.ijhydene.2012.05.129.
13. T. Ogawa, M. Takeuchi, and Y Kajikawa, Analysis of trends and emerging technologies in water electrolysis research based on a computational method: A comparison with fuel cell research. *Sustainability* **10**, 478 (2018), DOI: 10.3390/su10020478.

List of Publications

Papers

1. H. Ohno, S. Nohara, K. Kakinuma, M. Uchida, A. Miyake, S. Deki, and H. Uchida, Remarkable mass activities for the oxygen evolution reaction at iridium oxide nanocatalysts dispersed on tin oxides for polymer electrolyte membrane water electrolysis. *J. Electrochem. Soc.* **164**, F944 (2017), DOI: 10.1149/2.1101709jes.
2. H. Ohno, S. Nohara, K. Kakinuma, M. Uchida, and H. Uchida, Effect of electronic conductivities of iridium oxide/doped SnO_2 oxygen-evolving catalysts on the polarization properties in proton exchange membrane water electrolysis. *Catalysts* **9**, 74 (2019), DOI: 10.3390/catal9010074.

Meeting abstracts

Prize

1. First prize for Special Program for Clean Energy Science and Technology in Univ. of Yamanashi (2013).

International Conferences

1. H. Ohno, S. Nohara, A. Miyake, S. Deki, M. Watanabe, and H. Uchida, *3rd International Workshop on Green Energy Conversion*, P32, Yamanashi, Japan, August 25-27 (2014).
2. H. Ohno, S. Nohara, K. Kakinuma, A. Miyake, S. Deki, M. Watanabe, and H. Uchida, *International Fuel Cell Workshop 2015*, Yamanashi, Japan, August 27-28 (2015).
3. H. Ohno, S. Nohara, K. Kakinuma, A. Miyake, S. Deki, M. Watanabe, and H. Uchida, *The 229th Meeting of The Electrochemical Society,* San Diego, CA, May 29-June 2 (2016).
4. H. Ohno, S. Nohara, K. Kakinuma, A. Miyake, S. Deki, and H. Uchida, *PRiME 2016*, Honolulu, Hawaii, Abstract 2737, October 2-7 (2016).
5. H. Ohno, S. Nohara, K. Kakinuma, A. Miyake, S. Deki, and H. Uchida, 5th *International Seminar on Green Energy Conversion*, P12, Koumi, Nagano, August 31-September 2 (2016).
6. H. Ohno, S. Nohara, K. Kakinuma, M. Uchida, and H. Uchida, *6th International Seminar on Green Energy Conversion*, P13, Koumi, Nagano, September 13-15 (2017).
7. H. Ohno, S. Nohara, K. Kakinuma, M. Uchida, and H. Uchida, *International Fuel Cell Workshop 2018*, Yamanashi, Japan, August 23-24 (2018).

Domestic Conferences

1. H. Ohno, S. Nohara, H. Matsunaga, A. Miyake, S. Deki, M. Watanabe, and H. Uchida, The *81st Meeting in The Electrochemical Society of Japan*, 3P07, Ohsaka, March (2014).
2. H. Ohno, S. Nohara, K. Kakinuma, A. Miyake, S. Deki, M. Watanabe, and H. Uchida, *The 55th Battery Symposium in Japan*, 1C30, Kyoto, November (2014).
3. H. Ohno, S. Nohara, K. Kakinuma, A. Miyake, S. Deki, M. Watanabe, and H. Uchida, *The 56th Battery Symposium in Japan*, 1B29, Nagoya, November (2015).

Acknowledgments

This work was supported by the New Energy and Industrial Technology Development Organization (NEDO) of Japan (FY2013-2014), and "Fundamental Research on Highly Efficient Polymer Electrolyte Water Electrolyzers with Low Noble Metal Electrocatalysts" from Grant-in-Aid No. 17H01229 for Scientific Research (A) from Japan Society for the Promotion of Science (JSPS). All experiments in this work have been carried out at Clean Energy Research Center, Fuel Cell Nanomaterials Center, and Integrated Graduate School of Medicine, Engineering and Agricultural Science in University of Yamanashi.

At first and foremost, I would like to express my greatest gratitude to **Professor Hiroyuki Uchida** and **Associate Professor Shinji Nohara**, as my academic supervisors, for their continuous guidance, inestimable ideas, and warm encouragements throughout this work as if they are my fathers.

I would like to express my sincere thanks to **Professors Makoto Uchida** and **Katsuyoshi Kakinuma** for their invaluable suggestions and excellently academic advices in our immense discussions throughout this work, as well as my lab life.

I would like to express great acknowledgments to **Professors Masahiro Watanabe**, **Shigehito Deki**, and **Akihiro Iiyama** for their advices to support my experiments and belief in my life.

I would like to also thank to **Professors Kim Hasuck**, **Nobuhiro Kumada**, and **Masatoshi Yanagida** for their beneficial advices in my defense to create my dissertation.

For my study and manners in University of Yamanashi that is the basis of my knowledge, techniques, as well as styles, I am also grateful to **Professors Kenji Miyatake**, **Junji Inukai**, **Kazutoshi Higashiyama**, **Toshihiro Miyao**, **Donald A. Tryk**, **Manuel E. Brito**, **Takeo Kamino**, **Hiroshi Yano**, **Hanako Nishino**, **Junpei Miyake**, and

Kohei Suda.

For my gold experience through kind help and discussions in precious internships, I am grateful to **Professor Peter Strasser**, **Drs. Hong N. Nong**, **Hoang P. Tran**, **Camillo Spöri**, and **all members in Strasser's lab** of Technische Universität Berlin, as well as **Dr. Akiko Miyake** in Kobelco Eco-Solutions.

I appreciate the members of the catalyst team in our lab, **Drs. Guoyu Shi** and **Morio Chiwata**, as well as **Mr. Masahiro Haraguchi**, **Mr. Daiya Miyaji**, **Mr. Ikkei Arima**, **Mr. Hiromi Suzuki**, **Mr. Satoshi Ogawa**, **Mr. Yuma Shimizu**, **Mr. Honami Nishikawa**, **Mr. Shinya Hanyu**, **Mr. Daiki Yokomori**, **Mr. Yuta Ooishi**, **Mr. Keisuke Shiino**, **Mr. Shohei Asanuma**, **Mr. Kodai Kitagawa**, **Mr. Shuji Nakamura**, **Mr. Yuki Miyamoto**, and **Mr. Kazuaki Nakamura** for their strong assistances to my knowledge, techniques, as well as styles in my life.

I also appreciate the members in our lab, especially **Drs. Ryo Akiyama**, **Jun Omura**, **Masaru Sakamoto**, **Yuichi Senoo**, **Yuji Chino**, **Hideaki Ono**, **Yoshiyuki Ogihara**, **Kazuki Shimura**, **Kazuhiro Takanohashi**, **Yuya Yamashita**, **Ryosuke Nishikawa**, **Ryo Shimizu**, **Ahn Jinju**, **Chikara Takei**, as well as **Yutaka Ishibashi**, **Hisaki Itoga**, **Takahiro Inoue**, **Anna Oonishi**, **Hiromichi Nishiyama**, **Chisato Arata**, **Takumi Kuroda**, **Shigefumi Shimada**, **Ryunosuke Taki**, **Jun Fukasawa**, **Takashi Masuda**, **Shota Miyashita**, **Taro Kimura**, **Seiya Kosaka**, **Shun Kobayashi**, **Ibuki Hosaka**, **Koki Ueno**, **Kohei Uyama**, **Mizuki Ozawa**, **Yu Kakizawa**, **Ryo Shirasaka**, **Mizuki Hayashi**, **Kanji Otsuji**, **Ryo Kobayashi**, **Toshiki Tanaka**, **Takahiro Matsumoto**, **Shinnichiro Tsutsui**, and **Takayuki Watanabe** for their kind help, advices, and warm encouragements.

I would like to thank deeply all officers and staffs in **Clean Energy Research Center**, **Fuel Cell Nanomaterials Center**, and **Special Doctoral Program for Green**

Energy Conversion Science and Technology for their kind helps and supports.

Finally, I would like to dedicate my gratitude and this dissertation to **my family**.

Hideaki Ohno

March 2019